# Subwavelength silicon photonic nanostructures for applications in the near-IR and mid-IR

Thi Thuy Duong Dinh

université PARIS-SACLAY

# Subwavelength silicon photonic nanostructures for applications in the near-IR and mid-IR

*Nanostructures photoniques en silicium sub-longueur d'onde pour des applications dans l'infrarouge proche et moyen*

**Thèse de doctorat de l'université Paris-Saclay**

École doctorale n°575 : electrical, optical, bio-physics and engineering (EOBE)
Spécialité de doctorat : Electronique et Optoélectronique, Nano- et Microtechnologies
Graduate School : Sciences de l'ingénierie et des systèmes. Référent : Faculté des sciences d'Orsay

Thèse préparée dans l'unité de recherche **Centre de Nanosciences et de Nanotechnologies** (Université Paris-Saclay, CNRS), sous la direction de **Carlos ALONSO-RAMOS**, Chargé de recherche

**Thèse soutenue à Paris-Saclay, le 21 juillet 2022, par**

**Thi Thuy Duong DINH**

## Composition du Jury

| | |
|---|---|
| **Philippe DELAYE**<br>Directeur de recherche, Institut d'Optique (Université Paris-Saclay) | Président |
| **Gonzalo WANGÜEMERT PÉREZ**<br>Professeur des universités, Université de Málaga | Rapporteur & Examinateur |
| **Emilien PEYTAVIT**<br>Chargé de recherche (HDR), Laboratoire IEMN | Rapporteur & Examinateur |
| **Carlos ALONSO-RAMOS**<br>Chargé de recherche, C2N-Université Paris-Saclay | Directeur de thèse |

THESE DE DOCTORAT

NNT : 2020UPAST107

université PARIS-SACLAY

DOCTORAL SCHOOL
Electrical, Optical, Bio: Physics and Engineering (EOBE)

**Titre :** Nanostructures photoniques en silicium sub-longueur d'onde pour des applications dans l'infrarouge proche et moyen

**Mots clés :** Infrarouge moyen, Photonique au silicium, Sublongueur d'onde, Infrarouge proche, Nanostructures

**Résumé :** La photonique au silicium est prometteuse pour la production à grande échelle et à faible coût de circuits optoélectroniques de haute performance. Grâce à l'impressionnant développement technologique de ces dernières années, la photonique au silicium élargit ses frontières vers de nouvelles applications au-delà des communications de données, y compris, entre autres, la détection, la radio sur fibre et la quantique. Afin de répondre aux exigences de ces nouvelles applications, la communauté de la photonique au silicium explore de nouvelles gammes de longueurs d'onde et de nouveaux phénomènes physiques, avec un intérêt particulier pour l'infrarouge moyen (longueur d'onde de 2 à 20 µm) et les non-linéarités Kerr.

La photonique au silicium est prometteuse pour la production à grande échelle et à faible coût de circuits optoélectroniques de haute performance. Grâce à l'impressionnant développement technologique de ces dernières années, la photonique au silicium élargit ses frontières vers de nouvelles applications au-delà des communications de données, y compris, entre autres, la détection, la radio sur fibre et la quantique. Afin de répondre aux exigences de ces nouvelles applications, la communauté de la photonique au silicium explore de nouvelles gammes de longueurs d'onde et de nouveaux phénomènes physiques, avec un intérêt particulier pour l'infrarouge moyen (longueur d'onde de 2 à 20 µm) et les non-linéarités Kerr.

**Title :** Subwavelength silicon photonic nanostructures for applications in the near-IR and mid-IR

**Keywords :** Mid-Infrared, Silicon Photonics, Subwavelength, Near-Infrared, Nanostructures

**Abstract :** Silicon photonics holds the promise for large-scale and low-cost production of high-performance optoelectronic circuits. Driven by the impressive technology development in the recent years, silicon photonics is expanding its frontiers towards new applications beyond datacom, including among others, sensing, radio-over-fiber and quantum. Aiming to meet the requirements of these new applications, the Si photonics community is exploring alternative wavelength ranges and physical phenomena, with a particular interest in the mid-infrared (2-20 µm wavelength), and Kerr nonlinearities.

Silicon photonics holds the promise for large-scale and low-cost production of high-performance optoelectronic circuits. Driven by the impressive technology development in the recent years, silicon photonics is expanding its frontiers towards new applications beyond datacom, including among others, sensing, radio-over-fiber and quantum. Aiming to meet the requirements of these new applications, the Si photonics community is exploring alternative wavelength ranges and physical phenomena, with a particular interest in the mid-infrared (2-20 µm wavelength), and Kerr nonlinearities.

# Subwavelength silicon photonic nanostructures for applications in the near-IR and mid-IR

Thèse préparée dans l'unité de recherche **Centre de Nanosciences et de Nanotechnologies** (Université Paris-Saclay, CNRS), sous la direction de **Carlos ALONSO-RAMOS**, Chargé de recherche

**Thèse soutenue à Paris-Saclay, le 21 juillet 2022, par**


## Thi Thuy Duong DINH


## Composition du Jury

| | |
|---|---|
| **Philippe DELAYE**<br>Directeur de recherche, Institut d'Optique (Université Paris-Saclay) | Président |
| **Wangüemert-Pérez GONZALO**<br>Professeur des universités, Université Málaga | Rapporteur & Examinateur |
| **Emilien PEYTAVIT**<br>Chargé de recherche, Laboratoire IEMN | Rapporteur & Examinateur |
| **Loïc BODIOU**<br>Maître de conférences, Université de Rennes 1 | Invité |
| **Joan RAMIREZ**<br>Cadre scientifique, Nokia Bell Labs/ III-V lab | Invité |
| **Carlos-Alonso RAMOS**<br>Chargé de recherche, C2N-Université Paris-Saclay | Directeur de thèse |

# Acknowledgments

This doctoral thesis was accomplished with substantial contributions and great support from many motivated and wonderful people.

First and foremost, I am extremely grateful to my supervisor, Dr. Carlos Alonso Ramos, for his invaluable advice, continuous support, and patience during my Ph.D study. No words can fully express my deep gratitude to him. I also feel very lucky and honored to be his first student. Besides the dedicated guidance and support, he always brings positive energy, humor, and optimism in any situation. More than just a supervisor, he becomes a true friend. We can share everything about academic research, daily life, hobbies, music, food, travel, and even the silliest things. You won't be bored when you're around him. Gracias por todo lo que has hecho por mí, siempre eres el mejor supervisor.

I would also like to thank Dr. Laurent Vivien, Prof. Delphine Marris-Morini, and Dr. Eric Cassan for supporting my Ph.D. study. Thank Xavier Le Roux for his significant contributions, thoroughness, and kind helps in the sample fabrication. Thank everyone for their kindness and genuine concern for each student in the group. They always maintain the bond between every member and keep the spirit, positive energy of MINAPHOT group. Their kind helps and supports that have made my study and life in the C2N a wonderful time.

In addition, I would like to thank to Dr. Philippe Delaye, Prof. J. Gonzalo Wangüemert Pérez, Dr. Emilien Peytavit, Dr. Loïc Bodiou, Dr. Joan Manel Ramírez for reviewing my thesis and being members of my thesis committee. I enjoyed and appreciated helpful discussions, their knowledge, and suggestions.

I want to express my gratitude to all Ph.D. students and Postdoctoral in MINAPHOT group. Thank David Gonzalez and Paula for sharing the office with me, Alicia Ruiz Caridad (mi querida y siempre eres bienvenida a VietNam de nuevo), Daniel Benedikovic (always cheers me up), Christian Lafforgue (thanks for your patience, enthusiasm and dedicated instruction about Femto laser experimental setup), Miguel Montesinos Ballesteros, Jianhao Zhang, Thi Phuong Do, Lucas Deniel, Zhengrui Tu, Dorian Oser, Skylar Deckoff-Jones, Vincent Pelgrin, Jonathan Peltier, Misha Dyatlov, Thi Hao Nhi Nguyen, Natnicha Koompai, Qiankun Liu, Daniele Melati, Jerôme Michon, Victor Turpaud, Elena Durán-Valdeiglesias, Mikhaïl Dyatlov, Yijun Yang, Joan Manel Ramírez, David Medina, etc. We learn, play, have fun, and share great moments together. With those enthusiastic and humorous people, I have very much enjoyed my time at C2N over the years. I feel fortunate to be a member of MINIAPHOT group.

I also want to thank all my Vietnamese friends who have made my daily life enjoyable in France. Finally, I would like to express my gratitude to my parents, and my family, and my husband (Cảm ơn Linh Trần, nhờ anh truyền động lực đã giúp em đi xa tới tận đây). Without their tremendous support and encouragement over the past few years, it would be impossible for me to complete my study.

Palaiseau, France

July 2022

**Đinh Thị Thùy Dương**

# Synthèse en français

## Introduction

La région des longueurs d'onde de l'infrarouge moyen, qui s'étend de 2 à 20 µm, est reconnue comme une plage spectrale importante pour les applications de communication de données en espace libre, les capteurs chimiques et biologiques [1] et l'imagerie thermique [2], [3]. Une attention particulière a été accordée au développement de capteurs IR moyen sur puce basés sur la spectroscopie d'absorption. Chaque type de molécule absorbe la lumière à des longueurs d'onde infrarouges spécifiques, générant une empreinte d'absorption unique. Par conséquent, la présence et la concentration de molécules cibles dans un échantillon peuvent être examinées avec précision en mesurant le spectre de la lumière après interaction avec l'analyte.

La photonique au silicium présente un grand potentiel pour relever les défis de l'intégration de capteurs d'absorption compacts et à faible coût dans l'infrarouge moyen, en raison de sa capacité unique à produire des circuits photoniques ultra-compacts en grande quantité et à faible coût.

Ce PhD vise à développer une technologie photonique en silicium pour l'IR moyen, basée sur des guides d'ondes Si suspendus avec un revêtement SWG (voir figure 1). La motivation principale est de profiter de la large fenêtre de transparence du Si (longueur d'onde de 1,1 µm- 8 µm) tout en bénéficiant du contraste d'indice élevé, du matériau mature, du faible coût et de la fabrication en grand volume de la photonique au silicium. Le métamatériau à réseau sub-longueur d'onde (SWG) fournit une approche directe pour l'ingénierie de l'indice effectif, du profil de mode et de la dispersion, améliorant ainsi les performances des dispositifs photoniques. Au cours de mon doctorat, j'ai effectué des simulations de modélisation, des conceptions et des caractérisations expérimentales.

## Guides d'ondes suspendus dans l'infrarouge moyen en silicium avec une gaine métamatériale

Le silicium sur isolant (SOI) est la plateforme la plus courante pour les télécommunications optiques. La plateforme SOI classique comprend une couche de silicium cristallin (indice de réfraction de 3,44 près de la longueur d'onde de 1550 nm) au-dessus d'une sous-gaine d'oxyde enterrée (BOX), constituée de dioxyde de silicium (indice de réfraction de 1,44 près de la longueur d'onde de 1550 nm). Le contraste d'indice élevé entre le Si et le $SiO_2$ permet un fort confinement de la lumière, ce qui permet une intégration dense de guides d'ondes de rayon de courbure micrométrique. La plateforme SOI présente des avantages clés en termes de technologie de fabrication mature, de production de masse et de circuits photoniques compacts. Le silicium possède une grande transparence, atteignant une longueur d'onde de 8 µm. Cependant, l'utilisation du SOI dans l'infrarouge moyen est entravée par l'absorption de la silice au-dessus de la longueur d'onde de 3,6 µm [5].

Une alternative prometteuse pour exploiter toute la gamme de transparence du silicium (longueur d'onde de 1,1-8 µm) consiste à mettre en œuvre des guides d'ondes en silicium suspendus (voir figure 1a). De telles structures de membrane en silicium peuvent être fabriquées, par exemple en utilisant de l'acide fluorhydrique (HF) pour éliminer le sous-garnissage en $SiO_2$ [32], [37]. Pour le guide d'ondes suspendu à revêtement SWG (voir la figure 1), des trous périodiques avec une période inférieure à la longueur d'onde sont mis en œuvre sur les deux côtés du cœur du guide d'ondes. Ce revêtement de trous périodiques sub-longueur d'onde assure trois fonctions : i) un indice métamatériel effectif plus faible permettant le confinement de la lumière dans le cœur du guide d'ondes, ii) permettant la pénétration HF pour éliminer la silice, iii) la stabilité mécanique du guide d'ondes après l'élimination de la silice sous le revêtement.

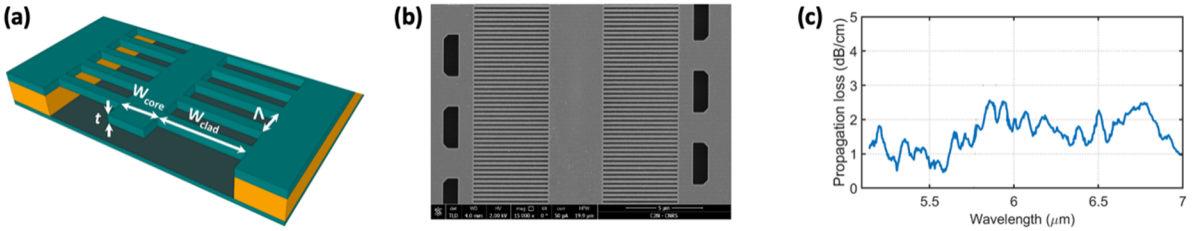


**Figure 1.** (a) Vue schématique d'un guide d'ondes en silicium suspendu avec une gaine sub-longueur d'onde. (b) Image au microscope électronique à balayage du guide d'ondes fabriqué. (c) Perte de propagation mesurée.

J'ai développé des guides d'ondes suspendus en silicium avec une gaine sub-longueur d'onde pour l'infrarouge moyen, fabriqués dans la salle blanche du C2N (Fig. 1b). J'ai démontré expérimentalement des pertes de propagation de 1-2.5 dB/cm dans la gamme de longueurs d'onde entre 5 µm et 7 µm (Fig. 1c). Ces faibles pertes de propagation constituent une avancée importante dans le domaine des guides d'ondes photoniques suspendus en silicium pour l'infrarouge moyen, et sont une caractéristique clé qui a permis la démonstration de la génération de supercontinuum par spectromètre à transformée de Fourier (voir chapitre 4) et de supercontinuum (voir chapitre 5). Ces guides d'ondes photoniques suspendus en silicium offrent un large éventail de possibilités pour développer des dispositifs photoniques innovants dans la gamme MIR, particulièrement intéressants pour les applications de détection de substances, d'imagerie et de communications optiques.

## Guides d'ondes en silicium à double métamatériau pour les applications de détection

Les guides d'ondes photoniques intégrés en silicium offrent de grandes possibilités d'exploitation des interactions lumière-matière à l'échelle nanométrique, avec des applications directes dans la détection biochimique pour la médecine, la détection des dangers et la surveillance de l'environnement [4], [51], [52]. J'ai développé des guides d'ondes en silicium à double métamatériau afin de maximiser les interactions lumière-matière pour des applications de détection [14].

J'ai validé expérimentalement un nouveau type de guide d'ondes nanophotonique qui permet un contrôle réglable du confinement du champ modal en incorporant deux métamatériaux différents dans le cœur et la gaine [14]. La conception à double métamatériau offre de nouveaux degrés de liberté pour façonner séparément le contraste d'indice vertical et horizontal, ainsi que pour l'ingénierie de la condition monomode. Le contraste d'indice vertical est déterminé par l'indice du métamatériau dans le cœur, tandis que le contraste d'indice horizontal et les conditions monomodes sont régis par la différence entre les métamatériaux du cœur et de la gaine.

J'ai développé des résonateurs annulaires à double métamatériau fonctionnant avec une polarisation TM dans des plaquettes SOI avec une couche de silicium de guidage de 220 nm d'épaisseur, un BOX de 3 µm d'épaisseur et de l'air comme revêtement pour démontrer le potentiel de ce concept (Fig 2). Selon mes simulations 3D-FDTD, le mode TM de notre guide d'ondes à double métamatériau fournit un facteur de confinement externe plus élevé dans l'air (0,35) que les guides d'ondes à bande avec polarisation TM (0,3). Mes expériences ont confirmé que les résonateurs en anneau à bande et à double métamatériau présentent des facteurs de qualité similaires d'environ 30 000. Les résonateurs annulaires métamatériaux doubles proposés constituent une alternative prometteuse aux guides d'ondes à bandes conventionnels, car ils présentent des facteurs de qualité similaires et une plus grande sensibilité de masse.

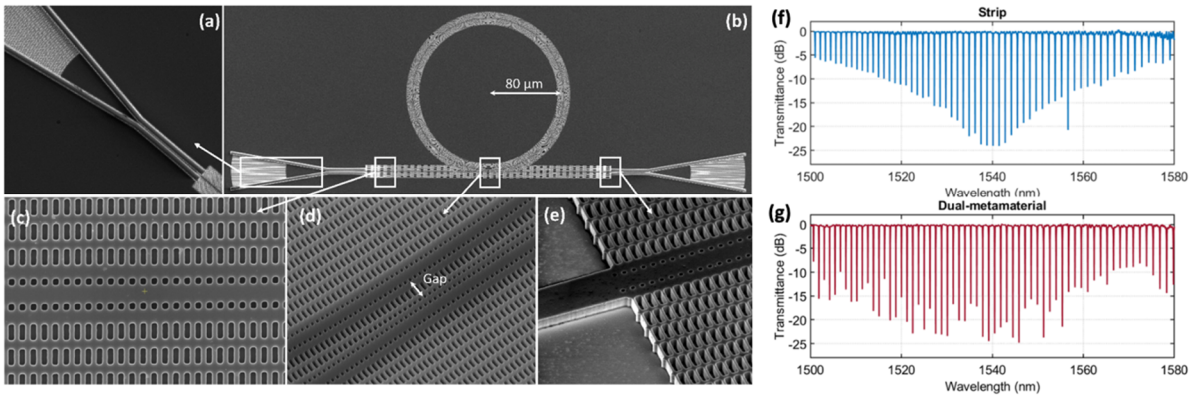


**Figure 2.** Images MEB du résonateur annulaire complet (a) coupleur à réseau de fibres-puces (b) micro-résonateur annulaire complet à double métamatériau ; (c) guide d'ondes à double métamatériau, (d) région de couplage entre le guide d'ondes bus et le résonateur annulaire ; (e) transition entre le coupleur à réseau et le guide d'ondes métamatériau. Comparaison de la réponse spectrale de (f) guide d'ondes à double métamatériau et (g) guide d'ondes à bande (W = 450 nm), tous deux au couplage critique avec un espace entre le guide d'ondes à bus et le résonateur de 600 nm, et un rayon de 80 µm.

## Spectromètre à transformée de Fourier

Les spectromètres photoniques miniaturisés en silicium ont un grand potentiel pour des applications grand public, allant de la médecine, des sciences biologiques et environnementales à l'astrophysique et aux télécommunications [156]. J'ai développé des

spectromètres hétérodynes spatiaux à transformée de Fourier (SHFTS) implémentés dans le silicium pour les longueurs d'onde du proche IR (section 4.2) et du moyen IR (section 4.3).

## SHFTS en silicium exploitant l'avantage du Jacquinot

Je démontre expérimentalement un SHFTS fabriqué par lithographie optique dans l'UV profond à 193 nm au CEA Leti, comprenant une large ouverture de collecte de lumière de 90 µm × 60 µm et un réseau de photodétecteurs Ge intégré. Le dispositif repose sur une nouvelle géométrie de réseau à alimentation bidirectionnelle, combinant deux coupleurs de réseau avec un angle de rayonnement opposé pour alimenter simultanément 16 interféromètres Mach-Zehnder (Fig. 2). Nous montrons expérimentalement une augmentation de l'étendue de ~13 dB, par rapport à une ouverture de coupleur de réseau d'entrée conventionnelle, en utilisant un faisceau d'illumination large de 0,5 mm FWHM. Nous avons comparé différentes configurations de dispositifs (Fig. 2), en illuminant tous les MZI simultanément avec une entrée de collecte à grande surface ou un par un avec des coupleurs à fibre optique conventionnels, et en enregistrant les sorties des MZI avec des photodétecteurs Ge intégrés et des photodétecteurs externes. La grande étendue de la configuration proposée et les puissantes corrections de phase et d'amplitude fournies par la technique pseudo-inverse ont permis de démontrer une résolution de 85 pm en utilisant une ouverture d'entrée de grande surface et des photodétecteurs intégrés, sans dégradation significative des performances par rapport à l'illumination individuelle de chaque MZI et à la lecture avec des photodétecteurs externes. Ces résultats ouvrent une nouvelle voie vers la production en grand volume de spectromètres miniaturisés sur puce en silicium photonique exploitant l'avantage de Jaquinot, ce qui peut être particulièrement intéressant pour les applications de détection dans les systèmes embarqués où le poids, la robustesse et l'étendue sont des paramètres clés [21].

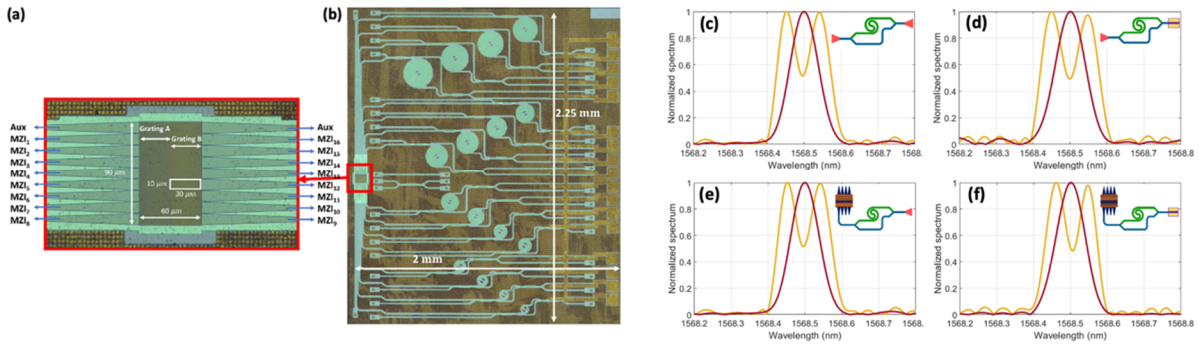


**Figure 3.** Images optiques de (a) coupleurs de réseau à alimentation bidirectionnelle et (b) SHFTS complets fabriqués, comprenant un coupleur de réseau de grande surface, un réseau de MIZ et des photodétecteurs Ge intégrés. Spectres récupérés d'une gouttelette monochromatique et d'une gouttelette avec une séparation crête à crête de 85 nm dans quatre configurations différentes : (i) illumination avec un réseau de fibres classiques, sortie collectée par un photodétecteur externe ou un photodétecteur intégré, (ii) illumination avec un coupleur à réseau large proposé et sortie lue par le coupleur à réseau classique.

## SHFTS dans l'infrarouge moyen mis en œuvre à l'aide de guides d'ondes suspendus en Si avec un revêtement sub-longueur d'onde

J'ai fait la démonstration d'un spectromètre SHFT intégré dans l'IR moyen, réalisé à l'aide de guides d'ondes en silicium suspendus avec un gainage à réseau métamatériel (figure 4). Cette stratégie permet de contourner la contrainte d'absorption de la gaine en silice pour les longueurs d'onde supérieures à 4 µm, ce qui permet de surmonter la principale limitation de la technologie SOI dans l'infrarouge moyen.

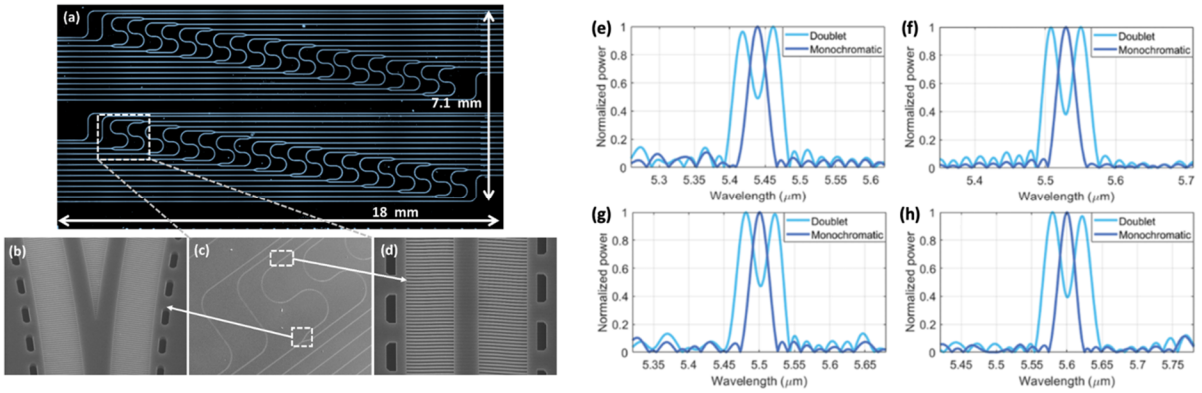


**Figure 4.** a) Image optique d'un SHFTS fabriqué, fonctionnant à une longueur d'onde dans l'infrarouge moyen et comprenant 20 MZI. Images MEB de (b) séparateur à jonction Y, (c) interféromètre Mach-Zehnder, et (d) guide d'ondes à réseau de sous-longueurs d'onde suspendu. Spectre récupéré d'un guide d'ondes suspendu à base de SHFTS fonctionnant en polarisation TE à différentes longueurs d'onde : (a) 5440 nm, (b) 5520 nm, (c) 5500 nm et (d) 5600 nm.

Le spectromètre SHFT comprend un réseau de 19 MZI avec une longueur de déséquilibre maximale de 200 µm, atteignant une résolution mesurée de 13 $cm^{-1}$ et une largeur de bande de 100 $cm^{-1}$, à proximité de la longueur d'onde de 5,5 µm. Il s'agit à notre connaissance de la plus grande longueur d'onde rapportée pour un spectromètre SHFT intégré en silicium. Ces résultats ouvrent une voie prometteuse pour la mise en œuvre de spectromètres intégrés exploitant le grand débit et la robustesse contre les imperfections de fabrication de l'architecture SHFT, exploitant la gamme complète de transparence du silicium (longueur d'onde de 1,1-8 µm) tout en profitant de la technologie SOI mature.

## Génération de supercontinuum dans le proche infrarouge et l'infrarouge moyen à l'aide de guides d'ondes en silicium suspendus avec une gaine sub-longueur d'onde

J'ai démontré une nouvelle approche pour contrôler l'excitation des ondes dispersives sur puce en exploitant les guides d'ondes métamatériaux en silicium. L'optimisation de la géométrie des guides d'ondes métamatériaux peut permettre un contrôle efficace et indépendant de la position des ondes dispersives de courte et de longue longueur d'onde [13].

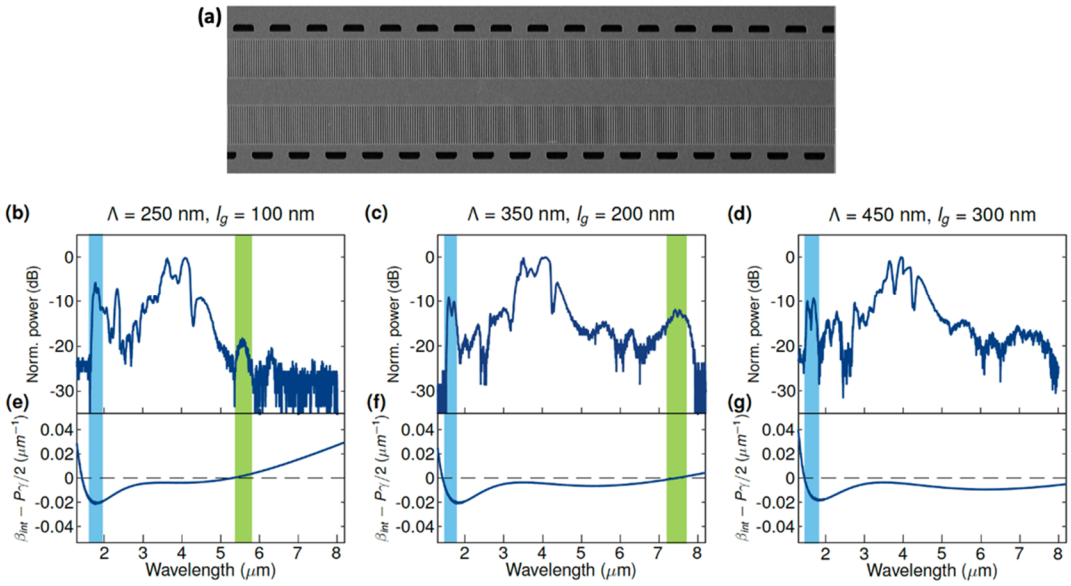


**Figure 5.** Images SEM du guide d'onde SWG suspendu fabriqué. Dispersion intégrée calculée et caractérisation expérimentale du supercontinuum des guides d'ondes à réseau métamatériel avec différentes longueurs d'espace (a) Lg = 100 nm, (b) lg = 200 nm, (c) lg = 300 nm, pour une longueur d'onde injectée de 3,5 µm et une puissance de pointe de 1 kW. La région grise correspond aux positions des ondes dispersives à grande longueur d'onde.

Je démontre expérimentalement l'accord de l'onde dispersive de grande longueur d'onde entre 5,5 µm et 7,5 µm de longueur d'onde, avec une variation négligeable de l'onde dispersive de courte longueur d'onde. J'utilise cette flexibilité d'ingénierie de la dispersion pour démontrer un supercontinuum s'étendant sur 2,35 octaves, entre deux ondes dispersives proches de 1,55 µm et 7,5 µm de longueur d'onde. Il s'agit, à notre connaissance, de la plus large génération de supercontinuum dans le silicium et de l'une des plus larges démonstrations utilisant des guides d'ondes intégrés. Ces résultats ouvrent une voie prometteuse pour la mise en œuvre d'un élargissement non linéaire de la lumière et d'une génération de fréquence polyvalente, couvrant les longueurs d'onde des télécommunications et de l'infrarouge moyen, grâce à la photonique du silicium. Nous prévoyons que l'approche des guides d'ondes métamatériaux favorisera le développement d'une nouvelle génération de circuits photoniques en silicium non linéaires de haute performance exploitant un contrôle flexible de l'excitation des ondes dispersives pour des applications émergentes en détection, métrologie et communications.

## Conclusions

Ce travail de thèse s'inscrit dans le cadre d'une activité de recherche à long terme axée sur le développement de dispositifs spectroscopiques intégrés pour des applications de détection dans l'infrarouge moyen, basés sur des guides d'ondes en silicium à réseau métamatériel. À cette fin, j'ai développé des blocs de construction fondamentaux pour les applications de détection comprenant trois composants principaux : une source supercontinuum dans

l'infrarouge moyen à bande ultra large, un composant d'interaction lumière-matière utilisant un résonateur microring métamatériau, et des spectromètres SHFT pour l'analyse du spectre. Tout au long de cette thèse, le SWG est l'outil clé et indispensable pour améliorer les dispositifs fonctionnels. La plateforme SWG en Si suspendue est la solution pratique pour résoudre les problèmes d'absorption de la silice dans l'infrarouge moyen, en élargissant la largeur de bande de fonctionnement de la plateforme SOI pour couvrir toute la fenêtre de transparence du silicium, de 1,1 μm à 8 μm de longueur d'onde. En outre, ce travail de thèse étudie la polyvalence et la faisabilité des microstructures SWG pour contrôler le confinement du champ, l'indice effectif, l'adaptation de phase et la dispersion.

# Table of Contents

# Chapter 1: Introduction

There is a growing interest in the mid-infrared (mid-IR) spectral range (2-20 μm wavelength) mainly driven by its immense potential for sensing in applications related to food safety, medical diagnosis, indoor air quality monitoring, defense, astrophysics science and resource exploration. In the first section of this chapter, I briefly introduce the mid-infrared spectral range and its interest for applications in molecular and biological sensing. The second section provides an overview of the objectives of the PhD work, while the third section describes the outline of this manuscript. The fourth section comprises a summary of the recent state-of-the-art of mid-IR photonic technologies.

## 1.1 Motivation of integrated photonics for sensing in the mid-infrared

The mid-IR wavelength region spanning from 2 to 20 μm is known as an important spectral range for applications in free-space data communications, chemical and biological sensors [1], and thermal imaging [2], [3]. Particular attention has been paid to develop the on-chip mid-IR sensors based on absorption spectroscopy. Each kind of molecule absorbs light at specific infrared wavelengths, generating a unique absorption fingerprint. Hence, the presence and concentration of target molecules in a sample can be examined precisely by measuring the spectrum of light after interacting with the analyte.

In the near-IR spectral range, several integrated nanophotonic biochemical sensors have been demonstrated achieving great performance, mainly based on specific chip surface functionalization and specific chemical reactions [4]. However, the implementation of optical absorption sensors in the near-IR is hampered by the limited strength of the absorption features of most of the molecules in this wavelength range, orders of magnitude weaker than in the mid-IR. Indeed, the mid-IR spectral range contains very strong absorption features of several important molecules [5] (see Figure 1.1), for example, carbon dioxide $CO_2$ (2.65 μm, 4.2-4.3 μm), carbon monoxide CO (4.5 μm), methane $CH_4$ (3.2-3.45 μm), nitric oxide NO (5.2 μm), some hazardous substances HF (2.33-2.78 μm), $H_2S$ (2.5-2.75 μm). These absorption features serve to identify trace gases, enabling real-time monitoring of multiple target molecules.

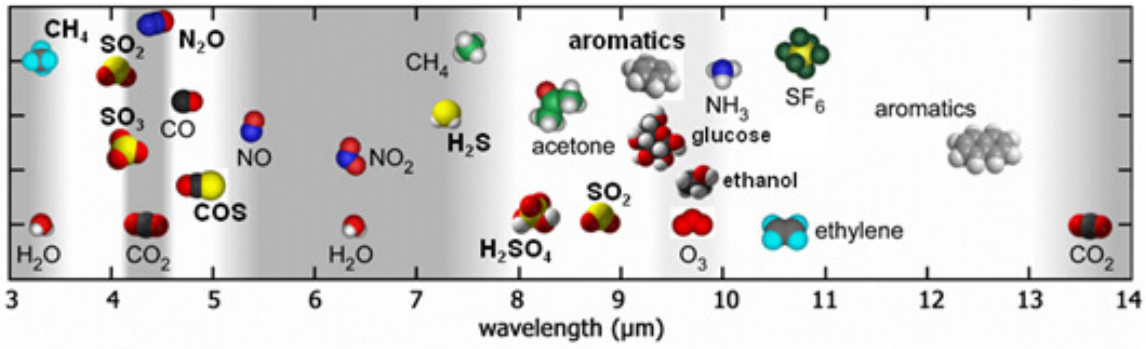


**Figure 1.1:** Graphical representation of the location of strong absorptions of several molecules of interest for applications in air pollution monitoring and industrial process control.

Optical absorption sensors in the mid-IR hold an immense potential for application in medical field [6]–[8], food safety [9], environment monitoring [10], [11], astronomy [12], and indoor air quality (IAQ) for controlling air condition. Silicon photonics has a great potential for addressing the integration challenges of compact and low cost integrated mid-IR absorption sensors due to its unique capability for the large volume and low-cost production of ultra-compact photonic circuits. In this regard, during the last two decades, there has been a surge of activities in the integrated mid-IR sensors, which has resulted in remarkable technological advances. However, while the integrated photonics technologies in near-IR, mainly telecom (near 1.55 μm wavelength) and datacom (near 1.3 μm wavelength) bands, are mature and well developed, the use of silicon photonics for the mid-IR remains an open challenge.

## 1.2 Overview of the PhD work

This PhD aims at developing a silicon photonics technology for the mid-IR, based on suspended Si waveguides with SWG cladding. The main motivation is taking advantage of the wide Si transparency window (1.1 μm- 8 μm wavelength) while benefiting from the high index contrast, mature material, low-cost and large volume fabrication of silicon photonics. The subwavelength grating (SWG) metamaterial provides a straightforward approach to engineer the effective index, mode profile, and dispersion, boosting the performances of the photonic devices.

Figure 1.2 illustrates one possible application of this envisioned technology for the development of optical absorption sensors. This complex circuit comprises 5 primary components: (i) narrowband mid-IR laser, (ii) broadband nonlinear mid-IR light source, (iii) light-matter interaction, (iv) optical spectrometer and (v) mid-IR photodetectors. The broadband mid-IR spectrum generated by the nonlinear effect, e.g. supercontinuum generation, propagates along the waveguide interacting with the target molecules. The resulting spectrum, marked with the absorption fingerprints of the analyte, is retrieved by

the spectrometer. The goal of this PhD is developing key passive and nonlinear devices that can be used for the implementation of complex mid-IR circuits as the described sensor. The integration of mid-IR laser and photodetector are out of the scope of this PhD work.

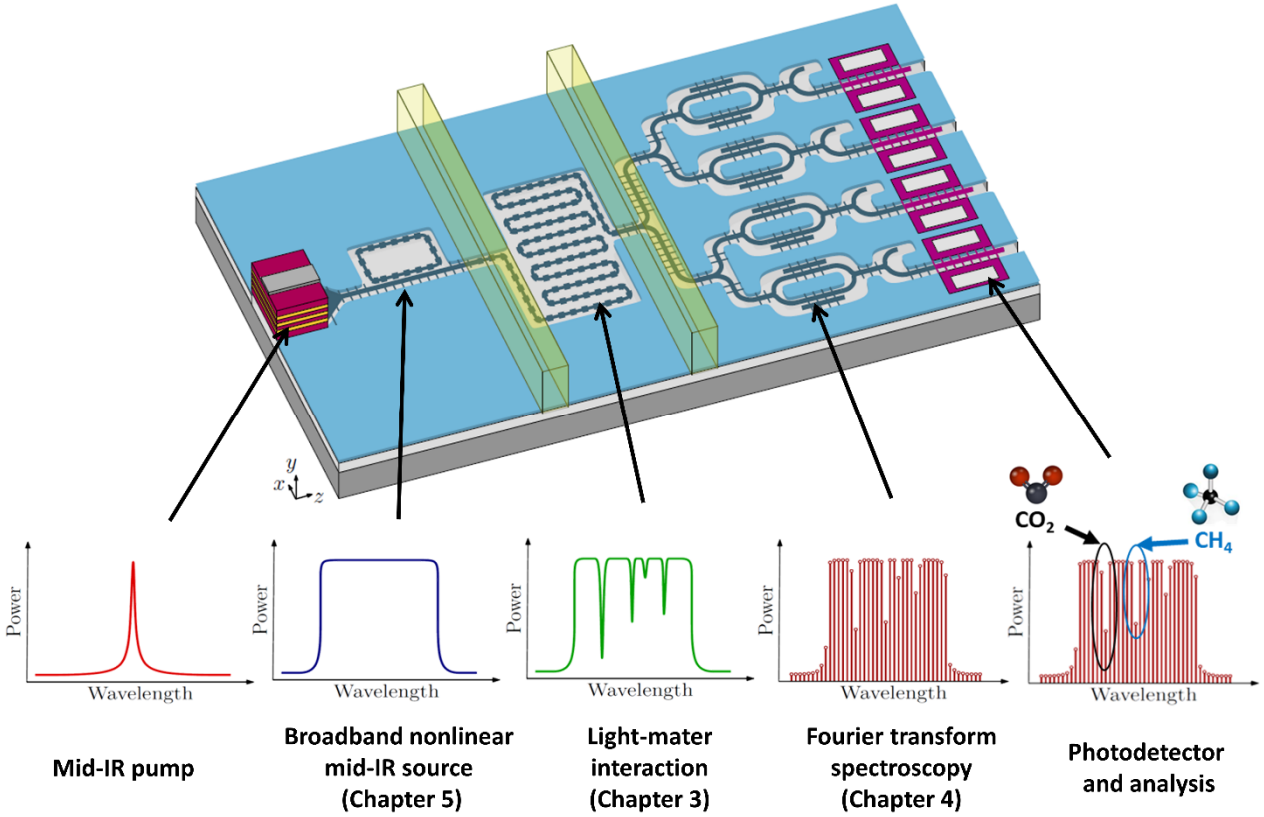


**Figure 1.2**: Schematic of the on-chip mid-IR sensor using metamaterial waveguides. This mid-IR sensor contains three main components: mid-IR light source, light-mater interaction, and Fourier transform spectrometer.

**The main results of this thesis are**:

- Development of the suspended silicon SWG-cladding platform with low-loss waveguides in mid-IR wavelength range (Chapter 2).
- Development of nonlinear supercontinuum generation in the mid-IR, exploiting metamaterial engineering to tune phase matching conditions [13], thereby controlling the supercontinuum generation process (Chapter 5)
- Exploit the degrees of freedom released by metamaterial engineering to shape the optical confinement [14], improving light-matter interactions (Chapter 3).
- Development of integrated Fourier-Transform spectrometers in the near-IR [15] and mid-IR [16] (Chapter 4).

## 1.3 Outline of the thesis manuscript

The manuscript is organized as follows:

**Chapter 1:** Motivation, objectives of the PhD work, state-of-the-art of integrated photonic technologies for mid-IR.

**Chapter 2**: Brief introduction to subwavelength metamaterial engineering, including main concepts and stage-of-the-art. Numerical study of the subwavelength metamaterial waveguide. Description of the fabrication processes and experimental results.

**Chapter 3**: Brief discussion of waveguide optimization for sensing applications, with basic concepts and state-of-the-art. Description of the proposed strategy to use metamaterial engineering to control optical confinement and improve the light-matter interaction strength, including numerical analysis and experimental results of metamaterial ring resonator in near-IR wavelengths.

**Chapter 4**: General introduction to Fourier transform spectroscopy and recent state-of-the-art. Presentation of proposed architectures and results on integrated spatial heterodyne Fourier transform spectrometers working in the near-IR and mid-IR wavelengths.

**Chapter 5**: Basic concepts of supercontinuum generation on silicon photonics. Discussion of dispersion control based on metamaterial engineering and results on supercontinuum generation.

**Chapter 6**: Conclusions of the PhD work and perspectives.

## 1.4 State-of-the-art mid-infrared photonics

### 1.4.1 Mid-IR platforms

Figure 2 shows the transparency window of several materials in the mid-IR. The use of conventional silicon-on-insulator (SOI) platform in the mid-IR range is hampered by the absorption of silica cladding for wavelengths above 3.6 μm [5], [17]. Several alternative materials with the wider transparency windows in the mid-IR have been proposed to overcome such problem. These include germanium on silicon (GeSi) [18], [19], silicon on silicon nitride (SOSN) [20], chalcogenides [21], [22], silicon on sapphire (SOS) [23], [24], and suspended silicon [25]. In this section, we briefly review some common platforms which have been exploited for use in mid-IR wavelengths. A summary of the reported platforms is given in table1.1 including the information of waveguide geometry, wavelength, and propagation loss.

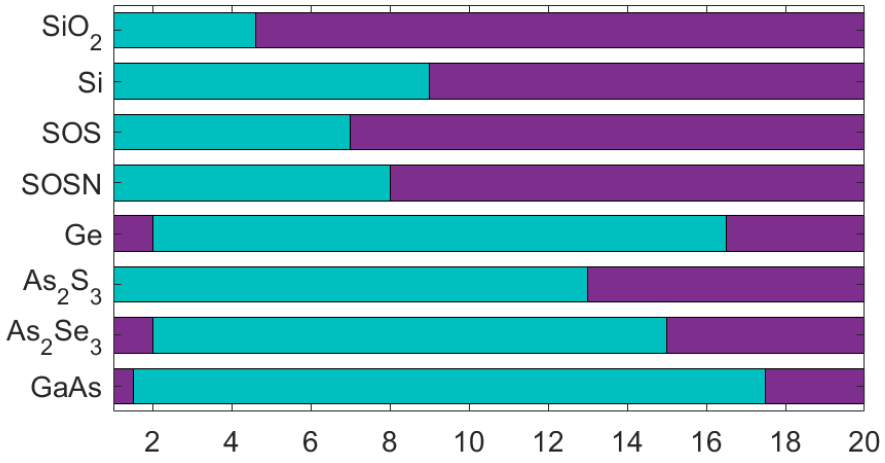


**Figure 1.3**: Transparency windows of several materials in mid-IR wavelength range. The violet area represents high loss, and the turquoise area indicates the transparency.

**Table 1.1**: Photonic platforms for the mid-IR

| No. | Platform | Type of waveguide | Wavelength | Propagation loss | Polarization | Ref. |
|---|---|---|---|---|---|---|
| 1 | SOI | Rib | 3.8 µm | 1.8 ± 0.2 dB/cm | TE | [26] |
| 2 | SOI | Slot | 3.8 µm | 1.4 ± 0.2 dB/cm | Slot mode | [27] |
| 3 | SOI | Strip | 3 - 6 µm | - | multimode | [28] |
| 4 | SOS | Strip | 4.5 µm | 4.3 ± 0.6 dB/cm | TE | [24] |
| 5 | SOS | Strip | 5.18 µm | 1.92 dB/cm | TE/TM | |
| 6 | SOSN | Rib | 3.39 µm | 5 ± 0.6 dB/cm | TE/TM | [20] |
| 7 | GOS | strip | 5.8 µm | 2.5 dB/cm | TM | [29] |
| 8 | GOS | Rib | 3.8 µm | 0.6 dB/cm | TE | [30] |
| 9 | GOSN | strip | 3.8 µm | 3.35 dB/cm | TE | [31] |
| 10 | Suspended Ge | SWG-cladding | 7.7 µm | 5.3 dB/cm | TE | [32] |
| 11 | Suspended Ge | Rib | 7.67 µm | 2.6±0.3 dB/cm | TE | [33] |
| 12 | graded GeSi | rib | 4.6 µm | 1.5 ± 0.5 dB/cm<br>2 ± 0.5 dB/cm | TE<br>TM | [18] |

| | | | | | | |
|---|---|---|---|---|---|---|
| 13 | graded GeSi | rib | 5.5-8.5 µm | 2-3 dB/cm | TE/TM | |
| 14 | Suspended Si | rib | 2.75 µm | 3 dB/cm | TE | [25] |
| 15 | Suspended Si | SWG-cladding | 3.8 µm | 0.82 dB/cm | TE | [34] |
| 16 | Chalcogenide | planar | 8.4 µm | 0.5 dB/cm<br>1.1 dB/cm | TE<br>TM | [21] |
| 17 | Chalcogenide | Rib | 5 µm | 0.3 dB/cm | TE | [22] |
| 18 | Suspended Si | SWG-cladding | 6.6 µm | 4.3 dB/cm | TE | [35] |
| 19 | Suspended Si | SWG-cladding | 7.6 µm | 3.1 dB/cm | TE | [36] |
| 20 | Suspended Si | SWG-cladding | 5-7 µm | <2 dB/cm | TE | This PhD |

***Silicon on insulator***

Silicon on insulator (SOI) is the most common platform for optical telecommunications. The conventional SOI platform comprises a crystalline silicon layer (refractive index of 3.44 near 1550 nm wavelength) on top of a buried oxide (BOX) under-cladding, made of silicon dioxide (refractive index of 1.44 near 1550 nm wavelength). The high index contrast between Si and $SiO_2$ allows a strong light confinement, providing dense integration of waveguides with micrometers bending radius. SOI platform has key advantages in terms of mature fabrication technology, mass production, and compact photonic circuits. Silicon has a wide transparency, reaching up to 8 µm wavelength (see Figure 1.3). However, the use of SOI in the mid-IR is hampered by silica absorption above 3.6 µm wavelength [5]. To reduce the light absorption in silica layer, S. A. Miller et al. proposed the use of large multi-mode waveguides, with cross-section of 2300 nm × 4000 nm. The large core yields strong light confinement in the Si core, decreasing the interaction with the silica cladding, achieving low loss below 1 dB/cm for wavelengths up to 6 µm [28]. The authors also demonstrated the SOI ring resonators using this design having the high intrinsic Q factor of $10^6$ at wavelengths from 3.5 to 3.8 µm. However, this strategy is not compatible with the implementation of optical absorption sensors, as most of the light is confined within the silicon core, with very little interaction with the waveguide surroundings where it can sense the analyte.

***Silicon on sapphire***

A common strategy for expanding the working wavelength of SOI is to replace the silicon oxide under cladding with alternative materials. The silicon on sapphire (SOS) platform consists of a thin silicon layer on a sapphire substrate (refractive index of 1.71 near 1550 nm wavelength). This platform has advantage in widening the transparency window in mid-IR up to 5 μm wavelength. However, sapphire has the limitations of being costly and more difficult to manipulate. SOS waveguides in the mid-IR were experimentally demonstrated for the first time in 2010, having a propagation loss of 4.3 ± 0.6 dB/cm at 4.5 μm wavelength [23]. Later in 2013, SOS waveguides have been reported showing low propagation loss about 0.7 dB/cm near wavelength 4.5 μm [24]. In addition, the SOS ring resonator has been realized having high Q factors of 151 000 operating wavelength of 4.5 μm [24]. SOS platform has been employed in several optical devices showing good performances, including high quality factor ring resonators [24], [37], grating couplers [38], absorption sensors, and nonlinear frequency generation in mid-IR wavelengths [39].

***Silicon on silicon nitride***

Silicon nitride ($Si_3N_4$) having refractive index of ~2 has been employed as an under-cladding to extend the working wavelength up to 6.7 μm [20]. Khan et al. have demonstrated silicon on silicon nitride platform at the mid-IR wavelength near 3.39 μm [20]. In this work, the SON thin films were fabricated by bonding a silicon die to a SOI coated with a silicon nitride layer. The waveguides achieved a propagation loss of 5.2 ± 0.6 dB/cm for transverse-electric (TE) polarization and 5.1 ± 0.6 dB/cm for transverse-magnetic (TM) mode. SON has been investigated for $CO_2$ sensing based on infrared evanescent field absorption [40]. In this work, the $Si_3N_4$ layer was deposited using low pressure chemical vapor deposition (LPCVD). This platform enables detecting $CO_2$ concentration down to 5000 ppm at working wavelength of 4.23 μm.

***Suspended silicon***

Another alternative to exploit the full silicon transparency range (1.1-8 μm wavelength) is to implement suspended silicon waveguides (see Fig. 1.4). Such silicon membrane structures can be fabricated, for example using hydrofluoric (HF) acid to remove $SiO_2$ under-cladding [34], [41]. Other methods were developed to implement suspended structures such as fusion-bonded suspended silicon membrane [42], and air-gap rib [43]. However, these methods require far more sophisticated fabrication procedures than prior method, resulting in increasing production costs.

The suspended platform stands out as a promising candidate for the mid-IR platform since it possesses several advantages:

- Exploit the wide Si transparency window up to 8 μm, strong Kerr effect and negligible two-photon absorption beyond 2.2 μm wavelength.
- Leverage the mature fabrication technologies of SOI, compatible with low-cost mass production.
- High index contrast between silicon ($n \approx 3.44$) and air cladding ($n \sim 1$), enabling compact devices.

Two main approaches have been proposed for the realization of suspended Si waveguides in the mid-IR: rib waveguide (see Figure 1.4(a)), and subwavelength grating (SWG) cladded waveguide (see Figure 1.4(b)).

The suspended rib waveguides (Figure 1.4(a)) were studied theoretically and experimentally by Cheng et al., showing propagation loss of $3 \pm 0.7$ dB/cm at wavelength near 2.75 μm [25]. A series of periodical holes are etched on both sides of the waveguide core, which allow HF penetration for the selective silica removal without affecting the propagation of the fundamental mode in the silicon core. The suspended rib waveguide requires two dry-etching steps (a full-etch step for periodical holes and a shallow-etch step for rib waveguide) and one wet-etching step.

For suspended SWG-cladded waveguide (see Figure 1.4(b)), periodic holes with subwavelength period are implemented at the two sides of the waveguide core. This subwavelength periodic hole cladding provides three functions: i) lower effective metamaterial index allowing light confinement in the waveguide core, ii) allowing HF penetration to remove silica, iii) mechanical stability of the waveguide after silica under-cladding removal.

The suspended silicon SWG-cladded waveguide has been demonstrated by J. Soler Penades et al. achieving the propagation loss of 0.82 dB/cm at wavelength of 3.8 μm [34]. At longer mid-IR wavelength near 7.67 μm, they reported the propagation loss of 3.1 dB/cm for transverse-electric (TE) polarized mode[36]. Zhou W. et al. demonstrated a fully suspended slot waveguide platform (see Figure 1.4(e)), which achieved the low propagation loss of 2.8 dB/cm, and high intrinsic Q factor of 12 600 at the wavelength near 2.2 μm [44]. Recently, a suspended silicon SWG waveguide platform with SWG grating metamaterial cladding was proposed for chemical sensing application in long-wave infrared wavelength range (see Figure 1.4(f))[35]. This suspended SWG waveguide platform has a flat propagation loss of 4.3 dB/cm in a broad wavelength range of 6.4–6.8 μm. Different passive devices, including grating couplers, Y-junctions, and directional couplers implementing on such platform have been exhibited with high performance. In addition, a limit of detection (LoD) is experimentally carried out for toluene vapor sensing achieving 75 ppm.

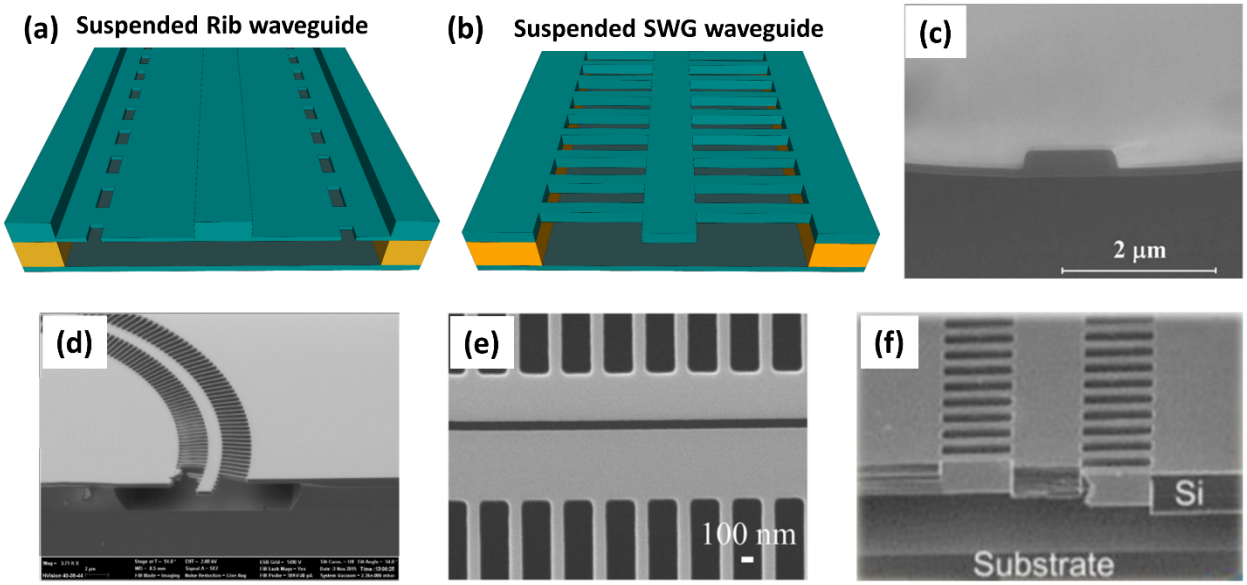


**Figure 1.4**: Schematic view of: (a) suspended rib waveguide, (b) suspended SWG waveguide. Scanning electron microscope images of: (c) suspended rib waveguide [25], (d) suspended SWG waveguide [34], (e) suspended slot waveguide [44], (f) suspended SWG waveguide long-wave infrared wavelength [35].

***Germanium***

Germanium (Ge) is a group-IV semiconductor material having a refractive index of n ~ 4. Ge-based platform is recognized as an excellent candidate for extending the operating wavelengths, especially for long mid-IR wavelengths above 8 µm (transparency limit of silicon). Several Ge-based mid-IR platforms have been studied for applications in the mid-IR, including germanium on silicon (GOS) [45], germanium on silicon nitride (GOSN) [31], germanium on insulator (GOI) [46], germanium-rich (graded) SiGe (GSOS) [18], [19].

In the GOS platform, the light is confined in the Ge core and Si serves as cladding material. The Ge strip waveguide on a Si substrate have been experimentally demonstrated with propagation losses of 2.5 dB/cm at a wavelength of 5.8 µm for transverse-magnetic (TM) polarization mode [29]. Low-loss GOS rib waveguides have been realized by M. Nedeljkovic et. al in 2015, achieving the propagation loss of 0.6 dB/cm at wavelength of 3.8 µm [30]. In longer mid-IR wavelength, K. Gallacher et al. reported the propagation losses below 5 dB/cm for wavelength from 7.5 to 11 µm in both TE and TM polarizations [45].

Ge on SOI (GOSOI) [46] and Ge on silicon nitride (GOSN) [31] have also been studied as potential platforms for mid-IR applications. GOSOI and GOSN platform provide high index contrast, enabling strong light confinement in the core. However, these platforms are limited

in the operating wavelengths due to the absorption of the SOI and silicon nitride in longer wavelengths.

For GeSi graded platform, the concentration of Ge is increased gradually along the thickness of the layer. By controlling the concentration of the Ge material during epitaxy growth, Ge graded Si platform allows tailoring the refractive index and mode confinement. Low-loss Ge-rich $Si_{0.2}Ge_{0.8}$ rib waveguides were demonstrated having propagation loss as low as 1.5 ± 0.5 dB⁄cm and 2 ± 0.5 dB⁄cm at 4.6 μm wavelength for the TE and TM polarizations, respectively [18]. Several optical devices-based Ge graded Si have been reported with high performances including MMIs [19], resonators [47], Fourier transform spectrometers [48].

In addition to the platforms mentioned above, suspended Ge platforms have also been considered for applications in long mid-IR wavelengths. The suspended Ge platforms can be fabricated by removing the silicon dioxide under the guiding-layer to produce the membranes. As a result, the achievable transparency window of these platforms can exceed 15 μm. In addition, the suspended platform has high index contrast which is advantageous for strong light confinement and efficient nonlinearity. The suspended rib Ge waveguides have been developed for the long infrared wavelength of 7.67 μm, achieving the propagation loss of 2.6 ± 0.3 dB/cm[33]. Later in 2021, A. Sanchez-Postigo et al. have first demonstrated the suspended Ge waveguide with subwavelength-grating metamaterial lateral cladding having propagation losses of 5.3 ± 1.0 dB/cm at a wavelength of 7.7 μm [32].

***Chalcogenide***

Chalcogenide glasses (ChGs) are amorphous compounds which have one or more chalcogen elements, such as sulfur, selenium, and/or tellurium [49]. Chalcogenide glasses are an interesting candidate for mid-IR integrated photonics due to their wide optical transparency window [50]. Sulfur chalcogenide glasses, for example, have a transparency window of up to 12 μm, whereas selenium glasses have a transparency window of up to 15 μm and tellurium glasses have a transparency window of up to 20 μm. Another benefit of ChGs is the amorphous structure, which allows monolithic integration on a wide range of mid-IR transparent substrates, such as $CaF_2$, $MgF_2$, and sapphire. In addition, composition engineering allows them to adjust their refractive indices in a wide range, enabling using of chalcogenide glasses for both waveguide core and cladding [22]. However, the main problems of the chacogenide glasses are chemical instability, and photosensitivity issues [51], [52]. Low-loss planar waveguides were fabricated from multilayer thin films of chacogenide glasses [21]. In this work, $As_2Se_3$ was used as core waveguide and $As_2S_3$ having lower refractive index served as cladding material. This planar waveguide structure presents propagation loss of 0.5 dB/cm and 1.1 dB/cm for TE and TM polarization at 8.4 μm wavelength [21]. In 2013, a rib

chacogenide glass waveguide was reported achieving the propagation loss as low as 0.3 dB/cm at 5 μm wavelength [22].

### 1.4.2 Mid-IR building blocks

In parallel with the progress of different materials used for mid-IR wavelengths, the development of functional devices is also attracted great interest and attention. In recent review publications, many noteworthy efforts on innovative MIR silicon photonics passive and active devices have been presented and summarized [53], [54]. In this section, we will discuss briefly about some basic building blocks for mid-IR: light sources, nonlinear wideband sources, photodetectors, and passive devices.

***Light sources***

Integrated light source is a key component of the Mid-IR sensor devices. However, the group IV materials (silicon and germanium) are not suitable for active devices due to their indirect bandgap properties. There are few alternative approaches including the heterogeneous integration of quantum cascade lasers (QCLs) [55], [56], intraband cascade lasers (ICLs) [57], nonlinear frequency conversion [58], and rare-earth doped material [59].

The quantum cascade lasers (QCLs) have developed extensively since their first demonstration by J. Faist and colleagues at Bell lab in the 1994 [56]. The working principle of QCL is based on intersubband transitions in semiconductor heterostructures. QCLs can cover a large portion of the electromagnetic wave spectrum from mid-IR to THz by engineering quantum well thicknesses and compositions of semiconductor alloy. In mid-infrared range, QCLs is considered one of the most widely used light sources.

More importantly, the QCLs have been successfully integrated on different platforms such as SOI, silicon on silicon nitride. In 2016, A. Spott et al. have proved the first heterogeneous integration of QCLs on silicon platforms [55]. The devices were integrated with the silicon-on-nitride-on-insulator (SONOI) platforms, emitting the light at 4.8 μm and operating in pulsed mode at room temperature.

***Nonlinear mid-IR sources***

In parallel with the development of heterogeneously integrated QCLs, an extensive number of works has been devoted mid-IR light source based on nonlinear effects. In this case, nonlinear effects (e.g. Kerr) are used to spectrally broaden a narrowband optical pump. Several materials, such as SOI [60], [61], GeSi [62], $SiN_x$ [63], Chacogenide [64], SOS [39], and suspended Si [65] have been used for nonlinear frequency generation in the mid-IR. Numerous nonlinear interactions have been exploited for mid-IR light sources such as different frequency conversions, four wave mixing [60], [66], stimulated Raman scattering

(SRS) [67], frequency comb [68], [69], and supercontinuum generation [39], [70]. Among of these nonlinear sources, supercontinuum generation source has been growing significantly for applications requiring a broad-spectrum coverage, such as spectrometers. Supercontinuum generation source is accomplished by launching a sufficient intense pulse through a nonlinear medium, achieving broadband spectrum. The basic mechanism of the SC generation involves both linear effect (dispersion) and nonlinear effects such as higher order soliton fission and self-phase modulation. Broadband supercontinuum generation in mid-IR wavelengths have been demonstrated in different materials including silicon on sapphire [39], SOI, chacogenide glass [64], suspended Si rib waveguide [71], GeSi graded [72]. More detailed state-of-the-art is provided in chapter 5.

***Photodetectors***

A photodetector is an essential component of an integrated photonic circuit, that converts optical signals to electrical ones. In terms of waveguide-integrated mid-IR photodetectors, there are four main approaches that have been implemented: (1) heterogeneous integration of narrow-gap semiconductors [73], (2) monolithic integration or growth of narrow-gap semiconductors [74], (3) narrow-gap Van der Waals semiconductor such as graphene [75], (4) ion-implantation of Si with dopants to introduce gap states [76].

Among the four approaches, heterogeneous integration of III-V detectors shows the best performance (responsivity, and signal-to-noise ratio - SNR) due to their high material quality. The monolithic integrated detectors (e.g., polycrystalline lead salts) exhibit highly competitive performance, while allowing thermal evaporation or solution processing. The emerging 2D Van der Waals-based detectors provide broadband detection in the mid-IR but have high dark current due to the nature of narrow or zero-bandgap. Lastly, Si implanted waveguide detectors are the simplest ones and are fully compatible with CMOS technology. However, this approach shows comparatively low responsivity.

***Passive devices***

A thorough state-of-the-art of integrated passive devices for mid-IR can be found in previous reviews [5], [53], [54]. Some relevant examples attaining excellent performances, include fiber-chip grating couplers [38], [77], [78], high quality-factor ring resonators [28], [79], Mach-Zehnder interferometers (MZI), multimode interference splitters/combiners [30], [34], polarization rotators/splitters [80]. Table 1.2 summarizes the current developments for various passive integrated components in mid-IR wavelengths including the information of structure, material platform, operating wavelength.

**Table 1.2**: Some passive mid-IR devices and their performances

| Structure | Material platform | Wavelength | Performances | Ref. |
|---|---|---|---|---|
| Grating coupler | SOS | 2.75 µm | Coupling efficiency = -4 dB (32.6%) | [81] |
| Grating coupler with inverse taper | GOS | 3.8 µm | Coupling efficiency = -11 dB (7.9%) | [77] |
| Grating coupler | GOS<br>GOSOI | 5.2 µm | Coupling efficiency = -5 dB (32%)<br>Coupling efficiency = -4 dB (40%) | [78] |
| Multi-mode interferometer | SOI | 3.7 µm | IL = 3.6 dB | [26] |
| Multimode interferometer | GOS | 3.8 µm | IL = 0.21 dB | [30] |
| Multimode interferometer | Suspended Si | 3.7 µm | IL < 0.7 dB | [34] |
| Microring resonator | SOS | 4.3 - 4.6 µm | Q = 151 000 | [24] |
| Microdisk resonator | Chacogenide glass | 5.2 µm | $Q = 2 \times 10^5$ | [79] |
| Microring resonator | SOI | 3.5-3.8 µm | $Q = 10^6$ | [28] |
| Photonic crystal cavity | Suspended Si | 4.4 µm | Q = 13 600 | [82] |

# Chapter 2: Mid-IR suspended silicon waveguides with metamaterial cladding

Since their first demonstration in silicon photonics [83], [84], subwavelength-grating metamaterials waveguides have been used as a powerful tool for overcoming performance limitations of conventional silicon photonic devices [85], [86]. Throughout this PhD, the subwavelength grating (SWG) metamaterials are employed to construct the basic building blocks for enhancing the performance of optical devices, with special interest in the mid-IR. This chapter is organized as follows. First, we provide a brief overview of the field of silicon subwavelength metamaterial engineering. Then, we present our results on mid-IR suspended silicon waveguides for the mid-IR.

## 2.1 Introduction

Periodic structuration with the subwavelength segments has been widely used in several photonic devices, playing a significant role in the development of integrated optics. The relative length of the grating period and the wavelength determines whether a periodic structure diffracts light or acts like an equivalent homogeneous medium. Nanostructuration releases multiple degrees of freedom to tailor optical properties of materials by engineering geometrical parameters like the period, or the duty cycle. The combination of metamaterial design and advanced lithography fabrication has enabled the demonstration of several optical devices exploiting subwavelength metamaterial engineering to achieve unprecedented performance [85], [87], [88]. In this section, we introduce the basic working principle of the SWG metamaterials and highlight their important role in developing the next generation of on-chip optical devices with applications in optical communications and sensing. Next, we briefly review the recent state-of-the-art and arising challenges of basic components for integrated optical spectrometer and discuss how SWG are exploited to improve the performance of advanced photonic devices.

### 2.1.1 Working principle of subwavelength grating metamaterials

Here, we consider the waveguide geometry depicted in Figure 2.1a, comprising a periodic array of alternating sections of different dielectric materials. This waveguide geometry is determined by the refractive indices $n_1$ and $n_2$ of dielectric materials, the period $\Lambda$ and the duty cycle, defined as $a/\Lambda$. Depending on the length of the periodicity of the dielectric grating,

compared to the optical wavelength, this structure can reflect, diffract, or transmit the light, acting as a homogeneous anisotropic medium [87].

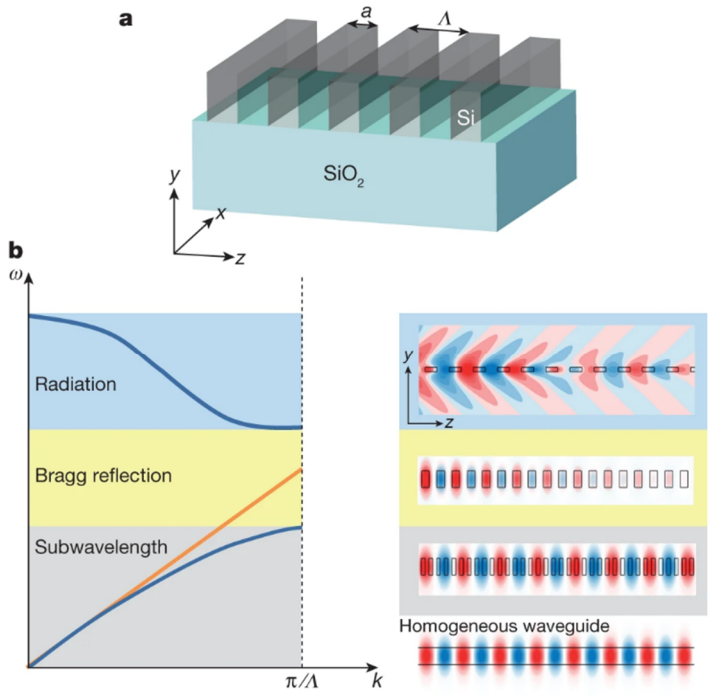


**Figure 2.1**: a) Schematic of the periodic waveguide. We consider light propagation along the z direction or the x direction. b) Schematic dispersion (left) and electric field profiles along the waveguide (right) of three different regimes: radiation, Bragg reflection, and subwavelength metamaterial *[85]*.

Depending on the length of the periodicity of the dielectric grating, compared to the optical wavelength $\lambda$, this structure can: (i) radiate the light, (ii) reflect the light, or (iii) transmit the light, acting as a homogeneous anisotropic medium [85], [87].

(i) In the radiation regime, the grating period is longer than haft of wavelength $\Lambda \geq \lambda/2$. The grating partially scatters guided light out of the propagation direction (Figure 2.1b). This radiation regime is widely used in integrated optics to implement surface grating couplers that interface integrated waveguides and optical fibers [89]. Other important applications of the radiation regime are the implementation of polarization beam splitter [90] and wavelength duplexers [91].

(ii) In the Bragg reflection regime, the period of the grating is equal to haft of the wavelength $\Lambda_{Bragg} = \lambda/(2.n_{eff})$. In this case, the light is back-reflected in the counterpropagating direction (Figure 2.1b). This Bragg reflection regime has been widely used in integrated optics to implement a myriad of devices, including among

others, wavelength filters [92], refractive index sensors [93] and mirrors for lasers [94], [95].

(iii) In the subwavelength regime, the period is shorter than haft wavelength $\Lambda \leq \lambda/2$. This short period precludes the radiation and reflection of light. Hence, the grating behaves as equivalent homogeneous medium, allowing loss-less propagation of light.

In the deep-subwavelength regime, the equivalent refractive index can be modelled following analytical expressions, the so-called Rytov equations [96]. For light propagation direction perpendicular ($z$ axis in Figure 2.1a) or parallel ($x$ axis in Figure 2.1a) to the grating periodicity, the equivalent metamaterial effective index can be calculated as:

$$n_{\parallel}^2 = \frac{a}{\Lambda} n_1^2 + \left(1 - \frac{a}{\Lambda}\right) n_2^2 \tag{2.1}$$

$$\frac{1}{n_{\perp}^2} = \frac{a}{\Lambda}\frac{1}{n_1^2} + \left(1 - \frac{a}{\Lambda}\right)\frac{1}{n_2^2} \tag{2.2}$$

For a given grating geometry, the effective index of the parallel polarization is higher than the one of perpendicular polarization $n_{\parallel} > n_{\perp}$. The Rytov equation provides fairly good initial approximation to study subwavelength structures.

Bloch-Floquet formalism can be used to accurately describe the behavior of SWG structures [97]. When the light propagates in $z$ direction, the Bloch mode is described as:

$$E(x, z + \Lambda) = E_B(x, z) \exp(-\gamma_B \Lambda), \tag{2.3}$$

where $\gamma_B = \alpha_B + jk_B = a_B + j(2\Pi / \lambda)n_B$ is the complex propagation constant, $\alpha_B$ is the attenuation constant, $k_B$ is the propagation constant, and $n_B$ is the effective index of the Bloch mode. The effective index of the Bloch- Floquet mode can be extracted from electromagnetic simulations based, e.g. on finite-difference time domain method [98] or definite-frequency eigenstate method [99]. As an example, figure 2.1b shows the dispersion diagram of a periodic waveguide. The blue line corresponds to the Bloch-Floquet modal calculations, while the orange line represents the dispersion considering a homogeneous structure with equivalent core effective index, calculated using Rytov's approximations. In the deep SWG regime ($\Lambda \ll \frac{\lambda}{2}$, i.e. small values of $k$ in Figure 2.1b), Bloch-Floquet and effective index methods yield similar results, suggesting that the SWG acts like the standard waveguide. However, near the Bragg condition, ($\Lambda \sim \frac{\lambda}{2}$ and k ~ 0.5) both methods deviate substantially.

In addition to these two methods above, the anisotropic model can be used to study subwavelength structure. This model provides a good compromise between isotropic model, which considers the medium to be homogeneous, and the Bloch-Floquet model, which

generally requires significant computational time and memory. The anisotropic approach provides better accuracy compared to isotropic model without increasing simulation time. This anisotropic model is particularly beneficial in determining the leakage losses and it has been used to study period structure in several previous works [32], [88].

### 2.1.2 State-of-the-art of subwavelength grating metamaterials

This section briefly summarizes the state-of-the-art of SWG metamaterials in silicon, describing some illustrative examples of how SWG metamaterials are exploited to improve the performance of advanced photonic devices. More details can be found in dedicated reviews [85], [87], [88].

Figure 2.2a shows a scanning electron (SEM) microscope image of the first reported silicon SWG waveguide [100]. The period is 300 nm, the width is 300 nm, and the duty cycle of 33%. These waveguides were experimentally demonstrated in 2010, showing propagation loss of 3 dB at 1.5 μm wavelength, which is comparable with the loss of standard Si waveguides at the time. One of the first applications of such SWG waveguides was the implementation of waveguide crossing with reduced loss and crosstalk for the propagating mode [101]. Figure 2.2b shows the SEM image of SWG waveguide crossing implemented on SOI platform. When light travelling in one waveguide crosses another waveguide, the overlap region between two waveguides causes the loss and crosstalk (light couples to the intersecting waveguide). SWG minimizes this overlap by delocalization of the Bloch-Floquet mode in the crossing region. The SWG-based crossing exhibited measured loss as low as -0.0023 dB/crossing, and crosstalk < -40 dB [101]. SWG waveguides have also been used to implement 5 μm radius ring resonators with high Q-factor of 11500 [102].

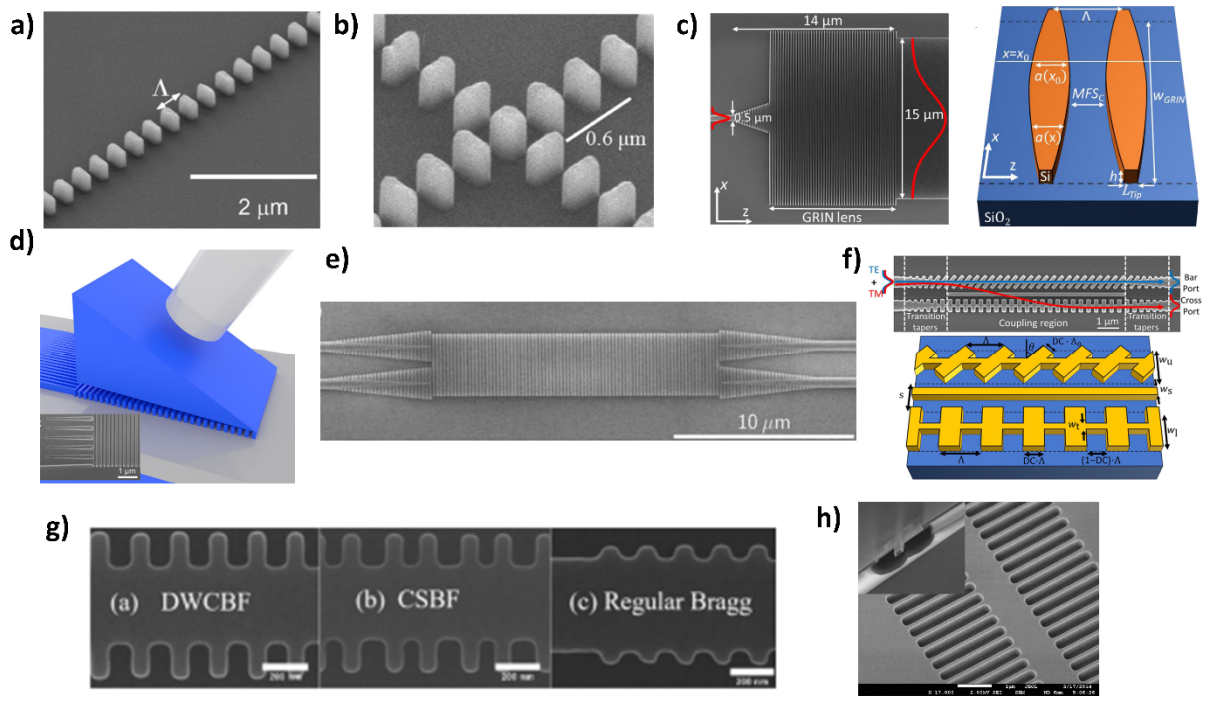


**Figure 2.2**: Selected examples of state-of-the-art SWG-based demonstrations: a) SEM image of the SWG waveguide on SOI platform with a width of 300 nm [100]; b) SEM image of the SWG waveguide crossing having a width of 300 nm, the period of 300 nm [101]; c) SEM image of the GRIN-lens-based spot size converter (left) and schematic of the SWG structure with the shape of the silicon blocks (right) [103]; d) Schematic representation and SEM image (inset) of the zero-order grating coupler [104]; e) SEM image of the SWG multimode interference coupler [105]; f) SEM image (top) and schematic (bottom) of the tilted SWG segments based polarization beam splitter [106]; g) SEM images of double-width corrugation Bragg filter (DWCBF), corrugation-shifted Bragg filter (CSBF), and conventional Bragg filter [92]; h) SEM image of the first SWG-based suspended silicon waveguide [41].

SWG waveguides have been used for developing several novel photonic devices, including integrated narrow band spectral filters [107], [108], broadband beam splitters [109], phase shifters [110], polarization controllers [111], fiber-chip grating couplers [89], [112]. Below, some examples are briefly described, illustrating the benefits of flexible SWG metamaterial engineering:

***On-chip beam formers***

One of the first demonstrations of SWG metamaterial engineering with SOI was the implementation of metamaterial graded-index (GRIN) lenses [113]. This concept has been recently extended to implement on-chip beam expander based on anisotropic GRIN metamaterial-based lens. In this case, the duty cycle is varied along the transversal

dimension to implement a parabolic index profile, as shown in figure 2.2c), yielding a 30-fold spot size expansion over a distance of 14 μm, with measured insertion loss below 1 dB and bandwidth exceeding 130 nm [103].

***Fiber-chip couplers***

The conventional optical fiber (SMF-28) has the mode field diameter much larger than the silicon waveguides with the submicron area. This large mode-size mismatch leads to a poor coupling efficiency. The ability to flexibly control mode confinement in SWG grating waveguides has been exploited to implement high-efficiency fiber-chip couplers. SWG-engineered facet couplers have been developed experimentally achieving coupling efficiency of 92% [114]. On the other hand, SWG engineering has been used to optimize the performance of fiber-chip grating couplers achieving coupling efficiency of 85% [112]. The combination of SWG and interleaved full and shallow etching steps allowed coupling efficiency of -1.3 dB [115]. A novel type of a grating coupler has been recently proposed combining a metamaterial waveguide and a silicon prism, see Figure 2.2d, to overcome the efficiency-bandwidth trade-off in conventional grating coupler [104]. The proposed device used of zero-order radiation, yielding a coupling efficiency above 80% with the insertion loss below 1 dB, covering bandwidth of 94 nm.

***Beam splitters***

SWG metamaterial engineering has been utilized to improve the performance of beam splitters, mainly in terms of bandwidth. SWG-based multimode interference (MMI) couplers (see Figure 2.2e) have been experimentally demonstrated that exploit anisotropy and dispersion engineering to achieve record 500 nm bandwidth [105].

***Polarization controllers***

SWG waveguides made of tilted silicon segments have been developed for application in on-chip polarization splitters [106]. Based on this concept, polarization splitters (see Fig. 2.2f) were demonstrated achieved a 72 nm bandwidth with insertion losses below 1 dB and an extinction ratio of 15 dB. Anisotropy engineered SWG polarization splitters have been recently reported achieving insertion losses below 1 dB and high polarization extinction ratio PER excess 20 dB cover a bandwidth of 200 nm [111].

***Wavelength filters***

The high index contrast of SOI waveguides hinders the implementation of narrowband Bragg grating filters, which are key for applications in quantum photonics [116]. Flexible index engineering in SWG waveguides has been utilized to overcome this limitation, achieving bandwidths below 1 nm. As an example, Figure 2.2g shows SEM images of SWG-engineered

filters based on differential SWG-based corrugation, achieving bandwidths of 0.8 nm with high rejection ratio exceeding 40 dB [92].

***Refractive index sensors***

The performance of photonic sensors is strongly related to the overlap of the optical mode with the target molecules. SWG metamaterial engineering has been proposed to deconfine the optical mode and maximize light matter interaction [117]–[119]. Bulk sensitivity of up to 579 nm/RIU has been demonstrated using multi-box SWG waveguides [117]. More detailed discussion on the use of SWG for enhancing the light-matter interaction is provided in Chapter 3.

***Mid-IR waveguides***

SWG engineering has also been exploited to implement suspended silicon waveguides that circumvent the absorption of the silica cladding for wavelengths above 4 μm. Figure 2.2h shows a SEM of the first SWG-based suspended silicon waveguide for the mid-IR range [41]. More details on the working principle of such waveguides are provided in the following sections.

## 2.2 Design

In this section, we discuss some strategic decisions regarding the design of the suspended waveguides and present the simulation strategy used to design the suspended silicon waveguides with subwavelength metamaterial cladding.

### 2.2.1 Geometry definition

Two main strategies have been reported for the implementation of suspended Si waveguides for applications in the mid-IR: a) rib waveguides (Figure 2.3a) [71], [120], and b) subwavelength-cladded waveguides (Figure 2.3b) [34], [35]. SWG-cladded waveguides allow fabrication with a single-etch step but require the definition of small-sized holes over comparatively thick Si layers. Our main motivation to implement SWG-cladded waveguides is the flexibility in controlling the properties of the cladding. For example, just by changing the duty cycle (defined as $a/\Lambda$) we can change the lateral confinement yet using only one etch step. This is key to implement complex circuits requiring sometimes highly-confined optical modes, e.g. to implement tight bending, and sometimes highly-deconfined optical modes, e.g. to maximize light-matter interaction. Another key advantage of the SWG-cladded approach is the flexibility in engineering the waveguide dispersion, which we exploit for supercontinuum generation (see Chapter 5).

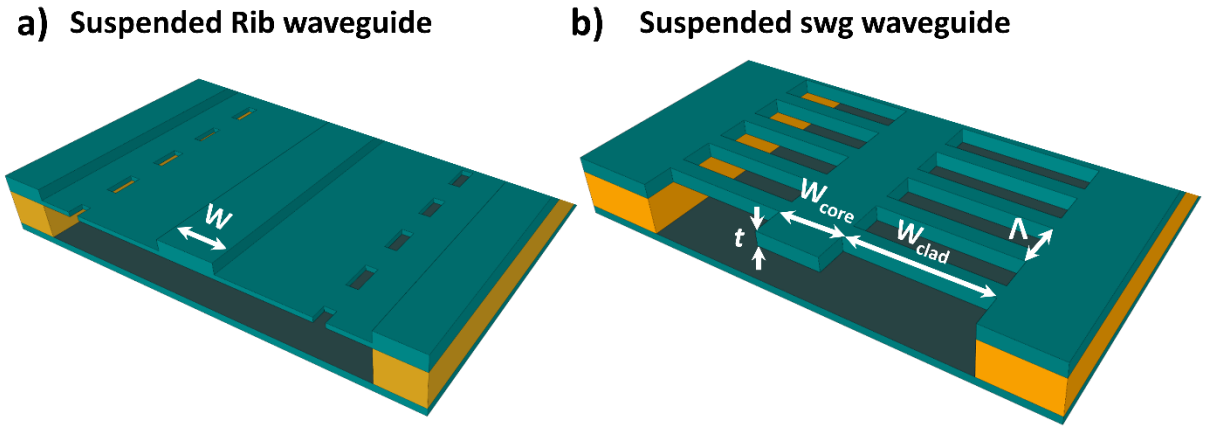


**Figure 2.3**: Schematic of a) a suspended Rib waveguide, and b) a suspended subwavelength-cladded waveguide.

The geometrical parameters defining the SWG-cladded waveguide, defined in Figure 2.4a, are the widths of the core ($W_{core}$) and cladding ($W_{clad}$), the silicon thickness (t), the buried oxide layer thickness ($t_{BOX}$), the grating period (Λ) and the length of the grating teeth (a).

In our cleanroom, we have access to SOI wafers with different Si thickness (220 nm, 300 nm, 500 nm, 700 nm and 1500 nm). On the one hand, the larger the Si thickness, the better the confinement of long wavelengths. On the other hand, the thicker the Si layer, the more difficult it is to etch subwavelength-size holes. Thus, we chose 700 nm thickness as a compromise solution. The SOI wafers with 700-nm-thick to silicon layer have a buried oxide layer thickness of $t_{BOX} = 3$ µm.

### 2.2.2 Simulation of optical modes

To study these SWG-based waveguides, we have employed two different simulation strategies: i) simplified model based on equivalent refractive index method, and ii) full vectorial three-dimensional simulations using finite difference time domain (FDTD) technique. The effective index method provides fast insight of how the optical mode is affected by geometrical parameters like waveguide width, SWG period, etc. Accurate analysis with 3D-FDTD requires a considerable computational effort. Hence, geometrical dimensions are first roughly designed with the effective index method and then fine-tuned.

We have modelled the chromatic dispersion of silicon by Sellmeire equation [121]:

$$n_{Si}^2(\lambda) = 11.6858 + \frac{0.939816}{\lambda^2} + \frac{0.00810461 \times 1.1071^2}{\lambda^2 - 1.1071^2} \qquad (2.4)$$

**Effective index method and 2D modal analysis**

The periodic waveguide is modeled by a non-periodic waveguide where the periodic cladding is substituted by a homogeneous medium with an effective metamaterial medium (see Figure 2.4).

The equivalent refractive index of cladding ($n_{clad}$) is calculated using Rytov's equation as [96]:

$$n_{clad}^2 \approx \frac{a}{\Lambda} n_{Si}^2 + \left(1 - \frac{a}{\Lambda}\right) n_{air}^2 \tag{2.5}$$

where $n_{Si}$ and $n_{air}$, are the refractive indices of silicon and air. Λ is the period and $a$ is the length of the grating teeth.

The optical modes of this effective waveguide are simulated with a commercial mode solver based on finite difference method (FDM) tool from Lumerical [122]. This simplified structure allows us to run several simulations in a short time. Note that this method has widely been used to study several SWG-based structures such as directional couplers [123], mode converters, and ring resonators [124].

As an example, Figure 2.4e shows the effective indices for the transverse-electric (TE) and transverse-magnetic (TM) polarized modes calculated with FDM. In this case, the widths of the waveguide core and cladding are $W_{core}$ = 2.5 µm and $W_{clad}$ = 5 µm, respectively. The waveguide thickness is t = 700 nm. The periodic structure considered for the calculation of the homogeneous effective index has a period of Λ = 350 nm, and duty cycle of a/Λ = 0.5. Figure 2.5 shows the calculated effective index of fundamental $TE_0$, $TM_0$ modes, and higher order $TE_1$, $TM_1$ modes as a function of wavelength, comparing them with slab mode. As can be seen, a width of 1500 nm yields single TE mode operation for wavelengths above 5 µm (Figure 2.5a), and single $TM_0$ mode for wavelengths above 4.5 µm (Figure 2.5.d). For comparison, the waveguide having core width of 2500 nm supports single TE mode for wavelengths above 7 µm, while a waveguide with width of 3500 nm has multimode behavior in the 3-8 µm range. For TM mode, the maximum wavelength for single mode operation is near 5 µm for both waveguides widths of 3500 nm and 2500 nm (Figure 2.5e, f).

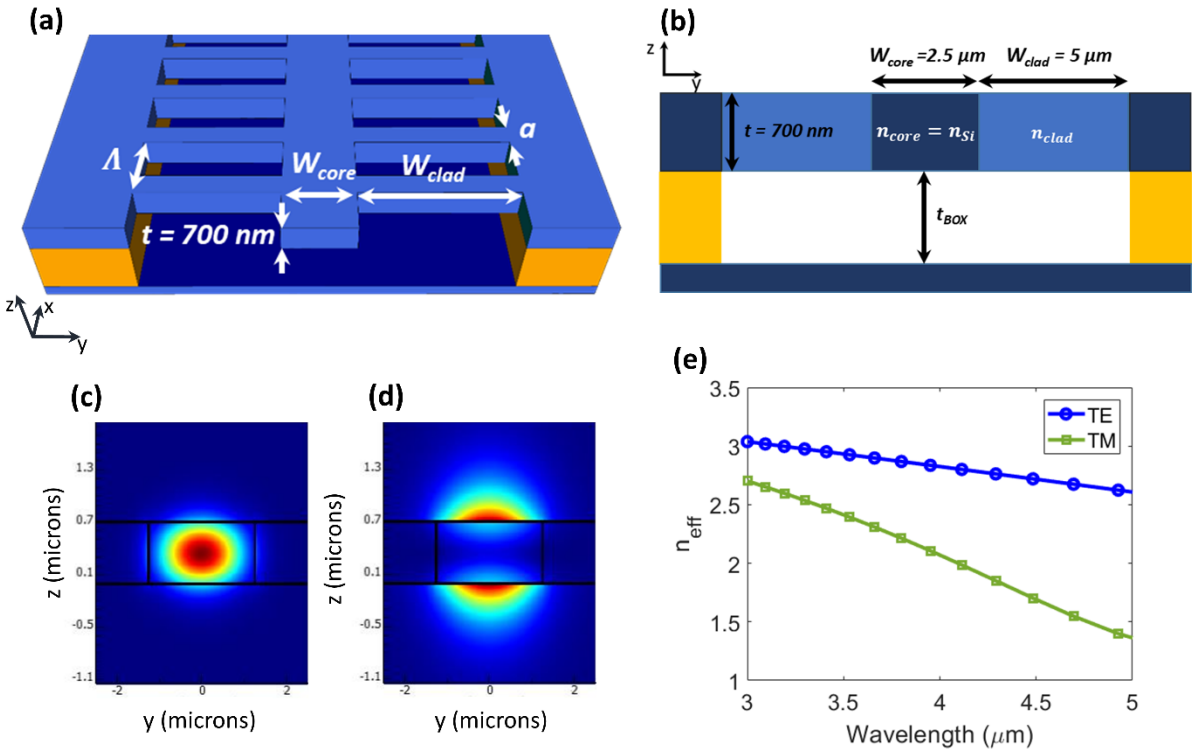


**Figure 2.4**: (a) Schematic illustration and (b) cross-section of subwavelength waveguide; (c) field profile of $TE_0$ mode and (d) $TM_0$ at 5 μm for the waveguide width $W_{core}$ = 2.5 μm, $W_{clad}$ = 5 μm, thickness t = 700 nm, pitch of Λ = 350 nm, and duty cycle a/Λ of 0.5, and (e) effective index of TE and TM mode as a function of wavelength.

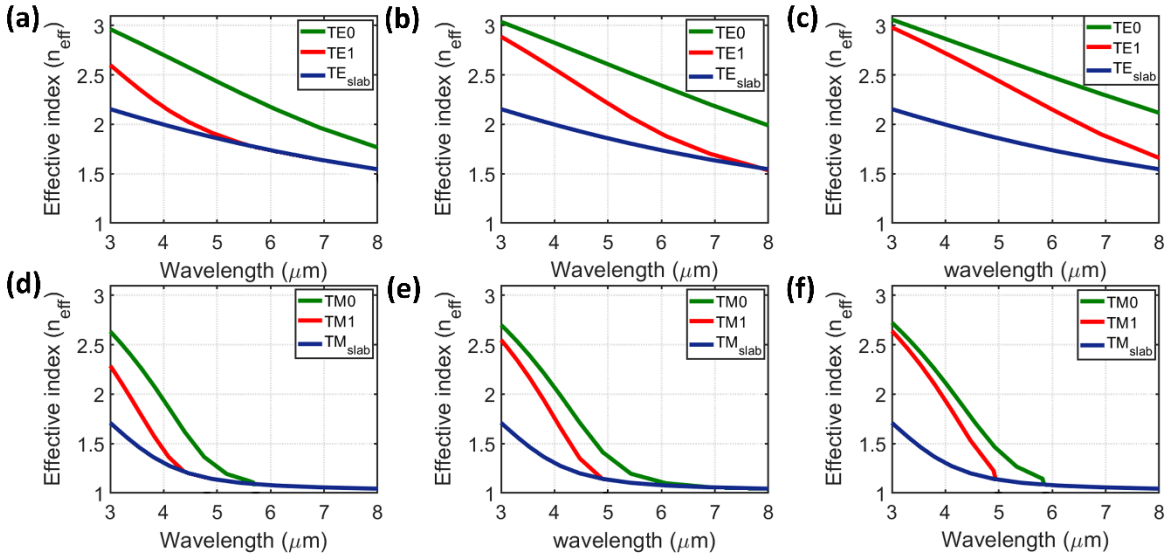


**Figure 2.5**: Effective index of the fundamental and first order TE and TM modes compared to the effective index of the slab mode of different width of (a), (d) 1500 nm, (b), (e) 2500 nm, and (c), (f) 3500 nm in mid-IR range from 3 to 8 μm wavelength.

**Full vectorial simulations with 3D FDTD**

To implement accurate simulations, we use full 3D vectorial FDTD method [98]. This method is derived from photonic crystal band structure computations since the SWG waveguide can be considered as 1D photonic crystal. This model enables studying the properties of an infinitely long waveguide by studying only one period (one-unit cell) of the structure and applying periodic Bloch boundary condition. According to the Bloch-Floquet theorem, the modes of the periodic structure can be described as $E = E_k(x,y,z)e^{-ikz}$, with $E_k(x,y,z) = E_k(x,y,z+\Lambda)$. Here, $k$ is the Bloch wavenumber, $\Lambda$ is the grating period.

Since we want to study modes with TE and TM polarizations we use dipole cloud, with randomly distributed orientations, to excite all possible modes. Note that specific optical mode can be selected by choosing the orientation of the dipoles and selecting the appropriate symmetry conditions [98]. We use a mesh resolution of $\Delta x \times \Delta y \times \Delta z = 10 \times 10 \times 10$ nm$^3$, as a compromise between accuracy and computational effort. We apply periodic Bloch boundary conditions in the propagation direction and perfectly matched layer (PML) boundary conditions in the other directions. The effective index of the Bloch modes is calculated using the relation $n_{eff} = \frac{c}{\omega}k(\omega)$. Figure 2.6a shows schematically the suspended SWG waveguide geometry. We selected the following geometrical parameters: the longitudinal period $\Lambda$ = 300 nm, core width $W_{core}$ = 2.5 µm, $W_{clad}$ = 5 µm, Si thickness t = 700 nm, the duty cycle of 0.5. Figure 2.6b showed the field profile of the fundamental TE mode calculated at 7.8 µm wavelength at the slide cut A and B. The calculated band structure and effective index of the fundamental TE mode using 3D FDTD are shown in figure 2.6c and 2.6d.

This model allows us studying the subwavelength structure precisely and extracts the modal properties using band structure analysis. However, the analysis of the band structure based on FDTD is time consuming and memory intensive, this model is not suitable for large parameters sweep.

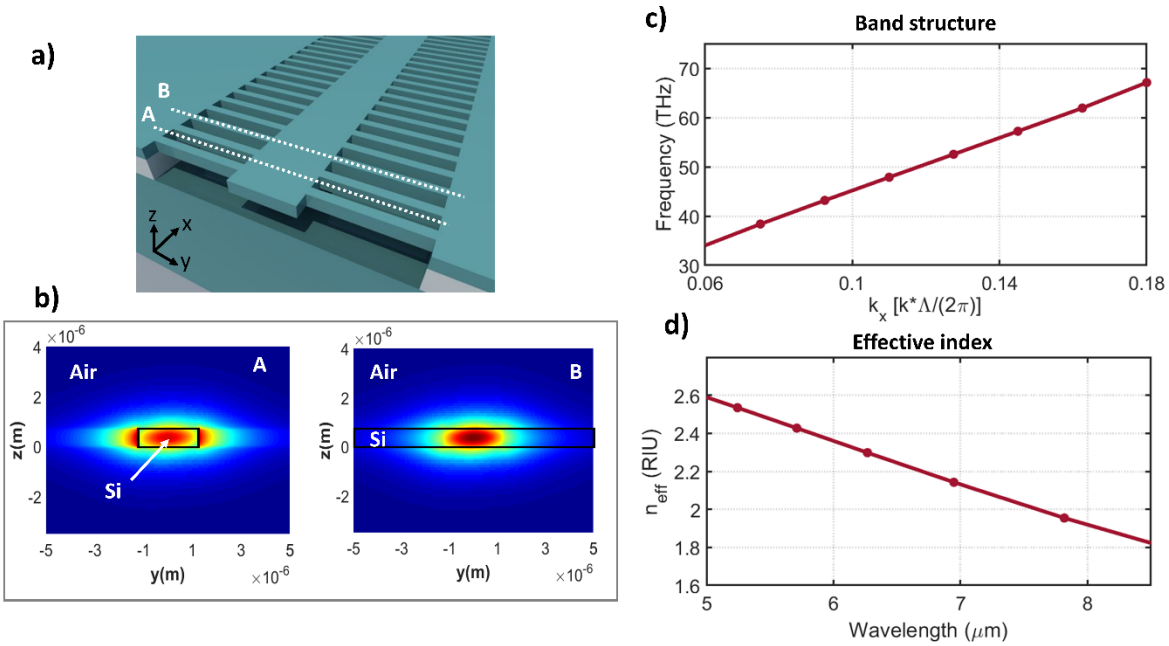


**Figure 2.6**: a) Schematic view of suspended subwavelength waveguide with the defined geometries $\Lambda$ = 300 nm, $W_{core}$ = 2.5 µm, $W_{clad}$ =5 µm, thickness t = 700 nm, the duty cycle of 0.5; b) the field profile of the fundamental TE mode at section A, B (illustrate) at central wavelength of 7.6 µm; c) Calculated band structure of suspended SWG using 3D FDTD model working in $TE_0$ polarized mode; d) Calculated effective index as a function of the wavelength in range of 5-8 µm.

Figure 2.7 compares the effective indices of the fundamental TE mode with different waveguide widths in mid-IR wavelength range calculated using 2D modal solver and 3D-FDTD simulation. In this figure, we used the following waveguide geometries: $\Lambda$ = 300 nm, $W_{clad}$ = 5 µm, thickness t = 700 nm, and the duty cycle of 0.5. As can be observed, the results calculated by 2D modal solver are in good agreement with the full 3D-FDTD solution.

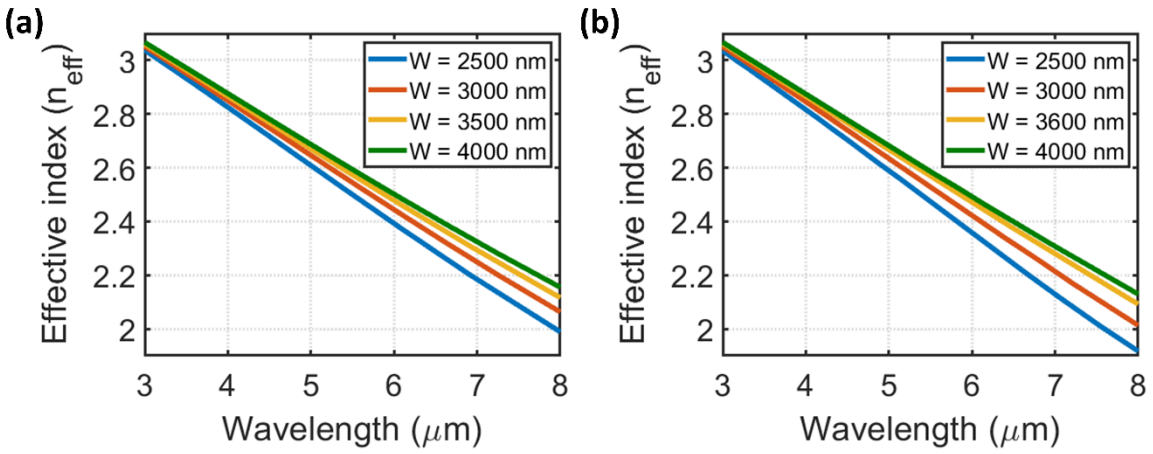


**Figure 2.7**: Comparison between (a) 2D-FDM and (b) 3D-FDTD simulation of effective index of the fundamental TE mode different widths ($\Lambda$ = 300 nm, $W_{clad}$ = 5 µm, thickness t = 700 nm, the duty cycle of 0.5).

## 2.3 Fabrication

The suspended subwavelength silicon waveguides have been fabricated in the C2N cleanroom. I have been in charge of the generation of the layouts, using in-house python tools. The lithography, etching and liberation have been performed by Xavier Le Roux and Carlos Alonso-Ramos.

The suspended silicon subwavelength waveguides were fabricated using SOI wafers with silicon guiding layer with thickness of 700 nm and buried oxide layer with thickness of 3 µm. The fabrication process, illustrated in Fig. 2.8, comprises 4 main steps: 1) electron-beam lithography resist (ZEP-520-A) is deposited on top of the SOI wafer by a spin coating; 2) the subwavelength structures are defined by electron-beam lithography; 3) the patterns are etched by inductive coupled plasma (ICP) reactive ion etching; 4) The buried oxide layer underneath was removed by hydrofluoric (HF) acid vapor.

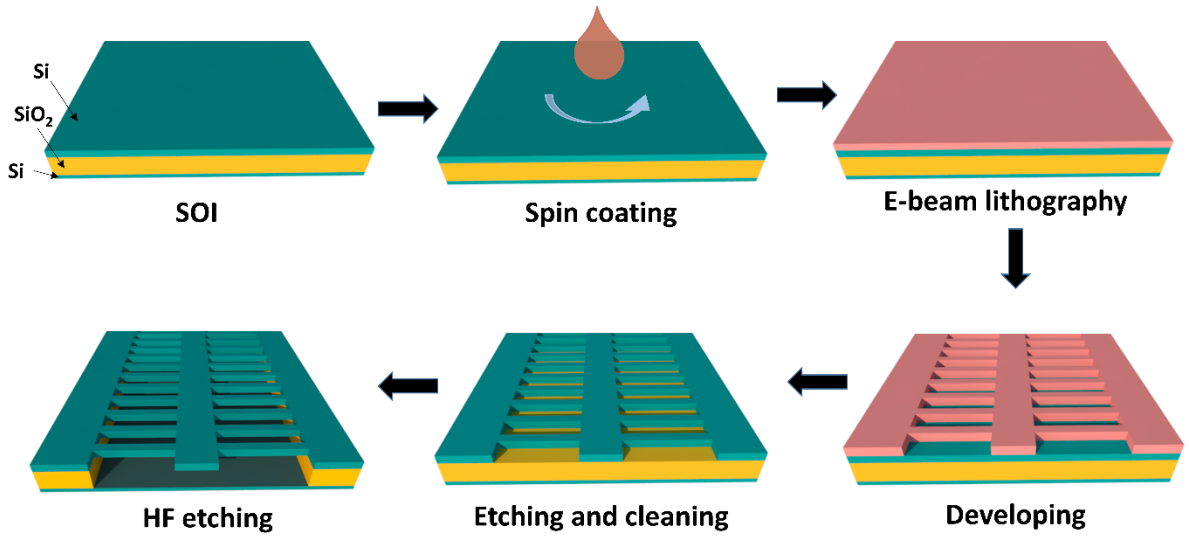


**Figure 2.8**: Schematic illustrates the fabrication processes of suspended subwavelength-grating waveguide on silicon platform implemented at C2N cleanroom comprising of main processes.

Figure 2.9 shows scanning electron microscopy (SEM) images of fabricated suspended subwavelength structures, including of a) top view SWG waveguide, b) enlarged view of SWG served as cladding; c) edge coupling of the SWG; c) waveguide bending; d) Y-branch splitter, f) fiber-chip grating coupler (for near-IR wavelength). The suspended SWG waveguide dimensions are $\Lambda$ = 300 nm, $W_{core}$ = 3.6 µm, $W_{clad}$ = 5 µm, Si thickness t = 700 nm. Regarding mechanical stability, we have fabricated several suspended SWG-waveguides with a few centimeters-length without observing any broken or collapsed structure. The HF evaporation etching process is reduces the surface tension, thereby allowing the improvement of the mechanical stability. In addition, we noticed no over-etching or reduction in thickness of the silicon guiding layer.

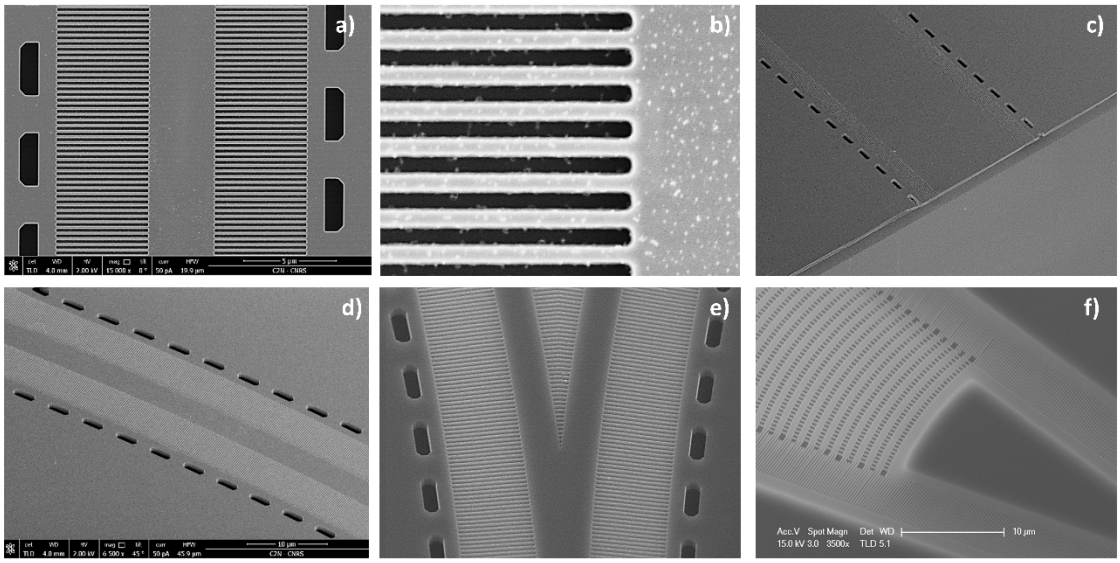


**Figure 2.9**: SEM images of suspended subwavelength waveguides on silicon platform fabricated at C2N cleanroom a), top-view SWG waveguide b) zoom in SWG serves as cladding, c) edge coupling of the SWG waveguide, d) S-bend subwavelength waveguide, e) Y-branch suspended subwavelength, f) fiber-chip grating coupler.

## 2.4 Experimental characterization

We have characterized the linear response of the fabricated suspended subwavelength waveguides using mid-IR experimental setup in C2N, depicted in Figure 2.10. As a mid-IR source, we use a tunable mid-IR laser (Mircat, daylight solution), comprising four different tunable QCL modules. The first QCL ranges from 5.01 µm to 6.1 µm wavelength, the second QCL from 5.8 µm to 7.06 µm, and the third QCL from 7 µm to 8.5 µm. The polarization of the collimated QCL output is controlled by polarization rotator. Then, the light is coupled into the chip by using aspherical lens made of ZnSe. The light propagates through the suspended subwavelength waveguides, and the output is collected by an aspherical lens and directed towards an external MCT (Mercury Cadmium Telluride) photodetector (DSS-MCT(14)020, Horiba). The MCT is cooled with nitrogen to minimize the thermal noise. A chopper, placed before the sample, and a lock-in amplifier are used to perform synchronous detection to improve the signal to noise ratio. Before employing the photodetector.

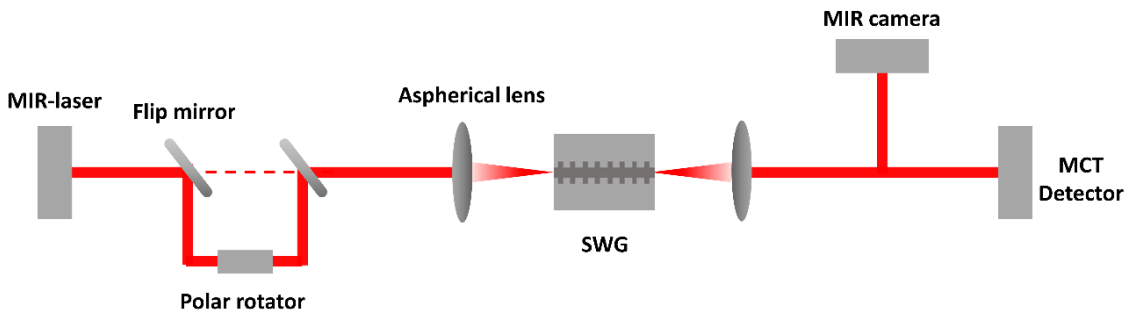


**Figure 2.10**: The experimental setup of the propagation loss measurement in mid-IR wavelength.

To characterize the propagation losses in mid-IR, we fabricated 4 suspended subwavelength waveguides with lengths ranging from 1.4 cm to 2.58 cm. The main geometrical parameters of the waveguide are: 700 nm thickness of silicon, core width of $W_c$ = 3.6 µm, cladding width of $W_{clad}$ = 5 µm, the period of 350 nm, the duty cycle of 0.4. These parameters have been chosen for dispersion optimization for supercontinuum generation (see Chapter 5). We experimentally characterize the transmission spectra of the fabricated waveguides in a range of 5 µm to 7 µm wavelength with the a sampling step of 2 nm. The propagation loss (in dB/cm) is calculated using the cut-back method by linearly fitting the measured insertion loss as a function of the wavelength for different waveguide lengths. The optical propagation losses are obtained from the slope of the linear regression. As an example, Figure 2.11 shows the measured optical transmission of SWG waveguide for TE polarization in the wavelength range of 5-6 µm (Figure 2.11a), and 6-7 µm (Figure 2.11b). The experimental setup comprises nearly 1 m of free-space propagation. Thus, the measured spectra are marked by the absorption fingerprints of the air (mainly water absorption peaks). To minimize the noise of the transmission spectrum, we smooth the measured curve with 50 sampling points. At each wavelength sample point, a linear regression fit of the optical transmission as a function of the normalized waveguide length is performed. As an example, Figure 2.11c depicts the linear fit for two different wavelengths of 5.5 µm and 6.4 µm. Figure 2.11d shows the measured propagation loss as a function of wavelength. At wavelengths between 5.2 µm and 5.7 µm, our waveguides yield propagation losses of 1–2.5 dB/cm. This result is a significant improvement compared to current metamaterial-clad Si membrane waveguides.

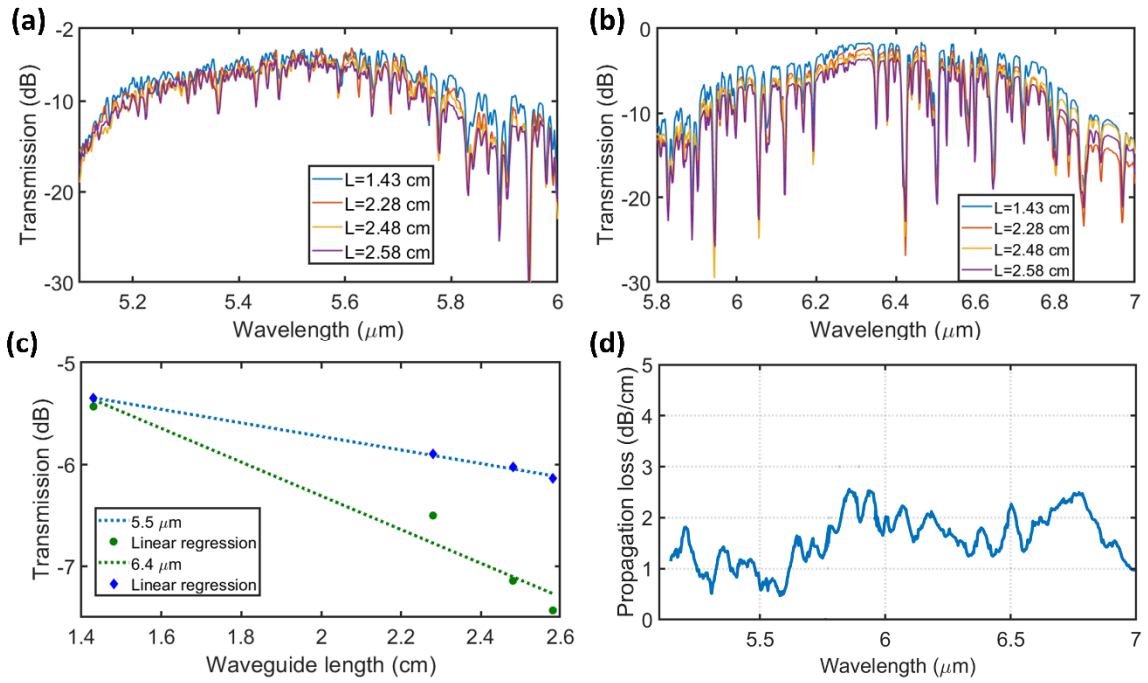


**Figure 2.11**: Experimental transmission spectra (a) from 5 to 6 µm wavelengths and (b) from 5.8 to 7 µm wavelengths of SWG waveguides with increasing lengths. (c) linear regression fit of the optical transmission as a function of the waveguide length at 5.5 µm and 6.4 µm; (d) propagation losses as a function of wavelength of fabricated suspended SWG with the waveguide core width of 3.5 µm, SWG grating width of 5 µm, the period of 350 nm.

The propagation loss improvement can be mainly attributed to optimized lithography and etching process. For comparison, previous demonstrations of metamaterial-cladded Si suspended waveguides in the mid-IR are summarized in table 2.1. These findings show that the subwavelength grating designed devices have great fabrication quality, possibly expanding the working wavelengths to the whole transparency window of silicon.

**Table 2.1**: Summary of previous demonstrations of metamaterial-cladded Si suspended waveguides in the mid-IR.

| Wavelength | Silicon thickness | Propagation loss | Ref. |
|---|---|---|---|
| 3.8 µm | 500 nm | 0.8 dB/cm | [34] |
| 6.6 µm | 1500 nm | 4.3 dB/cm | [35] |
| 7.6 µm | 1400 nm | 3.1 dB/cm | [36] |
| 5.1-7 µm | 700 nm | < 2 dB/cm | This PhD [16] |

## 2.5 Conclusion

In this chapter, we have presented the brief overview of the working principle and state-of-the art SWG-based devices in silicon photonics. We have also presented our results on the development of suspended SWG. We reported the numerical simulation techniques we used to study these free-standing SWG waveguide, and the fabrication processes in C2N cleanroom facilities. We experimentally characterized demonstrated propagation losses of 1–2.5 dB/cm in the wavelength range between 5 μm and 7 μm. Such low propagation loss stands as an important advancement in suspended silicon photonic waveguides for the mid-IR, and are a key feature that allowed the demonstration of Fourier-transform spectrometer (see Chapter 4) supercontinuum generation (see Chapter 5). These suspended silicon SWG offer a wide range of opportunities to develop innovative photonic devices in the MIR range, particularly interesting for application in substance sensing, imaging, and optical communications.

# Chapter 3: Dual-metamaterial silicon waveguides for sensing applications

Integrated silicon photonic waveguides provide great opportunities to exploit light-matter interactions at the nanoscale, with direct applications in biochemical sensing for medicine, hazard detection and environmental monitoring [4], [53], [54]. This chapter is devoted to the development of dual-metamaterial silicon waveguides to maximize light-matter interactions for applications in sensing. We begin this chapter by presenting the general working principles of photonic sensors based on absorption and refractive index monitoring. We briefly overview the main approaches proposed to maximize the interaction of the optical mode with the waveguide surroundings, targeting to optimize the detection sensitivity. In the second section, we introduce our novel approach based on a dual-metamaterial structure to improve the sensitivity of optical biochemical sensors. We describe how to use metamaterial strategies to engineer the optical confinement and then maximize the light-mater interaction. To demonstrate the operational feasibility of the proposed structure, we have fabricated the dual-metamaterial ring resonator and examined its optical properties. The numerical calculations and experimental analyses of SWG-based micro-ring resonators are also presented, along with a comparison to conventional waveguides. In the last section, we further extend the dual-metamaterial concept to implement suspended dual-metamaterial waveguides and ring resonators.

## 3.1 Introduction

### 3.1.1 Principle of operation of photonic sensors.

Optical waveguide modes generally expand outside of the waveguide core, with an exponentially decaying profile. The part of the mode profile expanding outside the waveguide core is commonly referred as evanescent field. The evanescent field can be used to interact with the waveguide surroundings for sensing applications. On-chip waveguide sensors typically exploit one of these two physical phenomena to detect the presence of the target molecules: i) variation of the real part of the effective index of the optical mode, ii) variation of the imaginary part of the effective index of the mode, or equivalently, the waveguide propagation loss. Note that both effects, effective index and absorption variation, are related through the Kramers-Kronig relations [125]. Refractive index sensors mostly exploit the variation of the effective index, while absorption-based sensors mostly utilize the variation of

the propagation loss. The operation principle of these two kinds of sensors is depicted in Figure 3.1 [126].

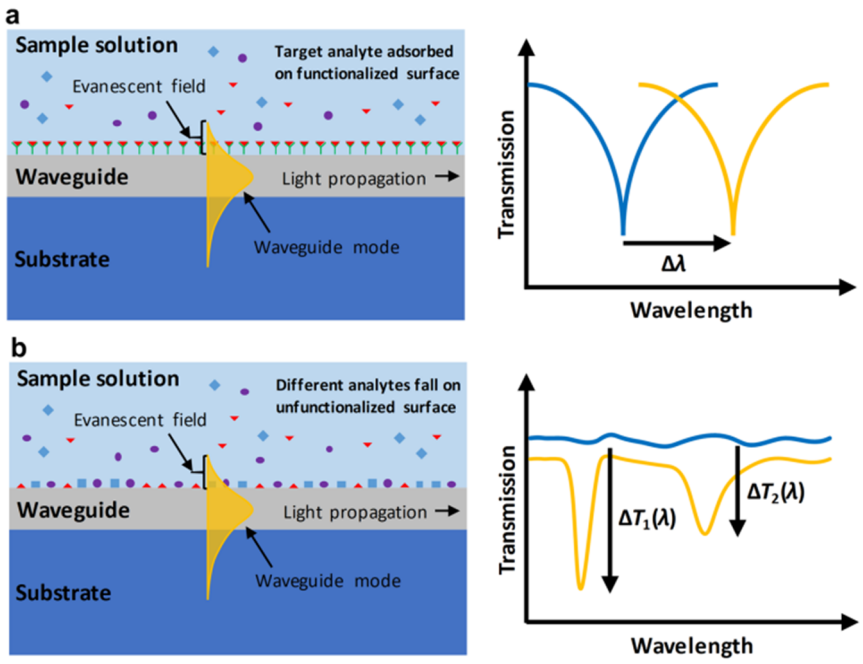


**Figure 3.1**: Schematic of the two types of the biochemical sensors: (a) RI-based sensor and (b) absorption-based sensor [126].

### Refractive-index sensors

When the guided light propagates through the waveguide, one part of the evanescent field overlaps with the surrounding media. Consequently, the interaction between the evanescent field and target molecules leads to the change of effective index of the optical mode. Two different scenarios (see Figure 3.2) are typically considered for refractive index sensors [127]: i) surface sensing, where the waveguide is surface functionalized to attach target molecules within a few-nanometer thickness, and ii) bulk sensing, where the analyte is modeled as a semi-infinite medium covering the waveguide.

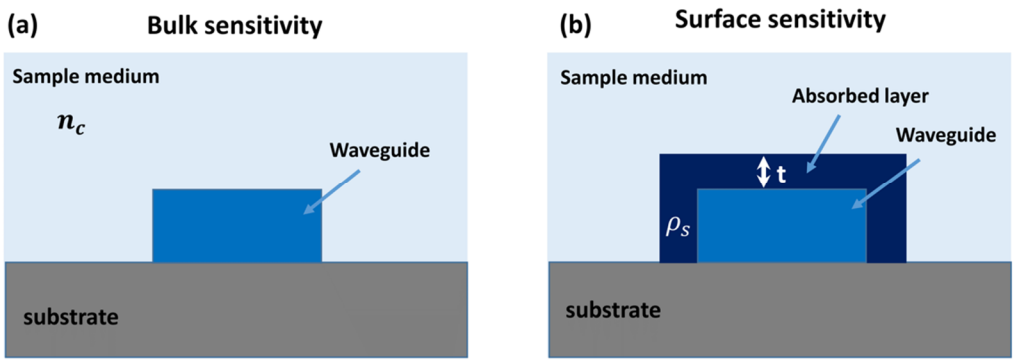


**Figure 3.2**: Schematic illustration of the (a) bulk sensitivity, and (b) surface sensitivity.

The sensitivity is one figure of merit typically used to benchmark these devices, indicating how much the effective index of the waveguide mode changes due to variations in the waveguide cladding. For bulk sensors, the sensitivity ($S_{bulk}$) is defined as [127]:

$$S_{bulk} = \frac{\partial n_{eff}}{\partial n_c} \qquad (RIU/RIU) \tag{3.1}$$

where $n_{eff}$ is the effective index and $n_c$ is the index of surrounding environment. From the equation, the meaning of bulk sensitivity can be understood as the ratio of the change in the effective index of the guided mode to the change in the external environment [1].

For surface sensors, the sensitivity ($S_{surf}$) is defined as [127]:

$$S_{surf} = \frac{\partial n_{eff}}{\partial t} \ (RIU/nm) \tag{3.2}$$

where $t$ is the thickness of the absorbed layer. This sensitivity determines the ratio of the change in mode effective index to the change in thickness of the functionalized molecular layer. Ideally, the functionalized layer changes thickness only when the target molecules are attached to it.

Bulk and surface sensitivities are both proportional to the overlap of the optical mode with the analyte [126]. So, as discussed in section 3.1.3, there has been a considerable research activity focused on the development of integrated waveguide geometries maximizing the strength of the evanescent field and its overlap with the analyte.

Typically, three types of sensitivities are used: waveguide sensitivity ($S_w$), architectural sensitivity ($S_a$), and device sensitivity ($S_d$) [127]. The waveguide sensitivity converts physical changes caused by molecule binding into effective index variations, whereas the architecture sensitivity converts changes in the effective index into the phase shift (interferometric architecture), or wavelength shift (resonant architecture). The device sensitivity (total sensitivity) is described as the product of waveguide and architecture sensitivities $S_d = S_w S_a$.

These bulk sensitivity ($S_{bulk}$ in equation 3.1) and surface sensitivity ($S_{surf}$in equation 3.2) are the waveguide sensitivities.

**Absorption sensors**

The Beer–Lambert law defines the intensity of the light transmitted through a homogeneous medium, exhibiting a wavelength dependent absorption coefficient $\sigma(\lambda)$ as [128]:

$$I(\lambda) = I_0(\lambda)e^{-\sigma(\lambda)cL} \tag{3.3}$$

where as $I(\lambda)$ is the transmitted light intensity, $\lambda$ is the wavelength, $c$ is the concentration of the absorbing material and $L$ is the interaction path length. As each molecule has a unique wavelength dependent absorption coefficient, typically referred as absorption fingerprint, analysis of the spectrum of the transmitted light allows precise detection of the composition of the medium, i.e. type of molecules and their relative concentration [128].

For light propagating along a waveguide, the Beer-Lamber law can be adapted as:

$$I(\lambda) = I_0(\lambda)e^{-\sigma(\lambda)\Gamma cL}e^{-\alpha(\lambda)L} \tag{3.4}$$

Here, $\alpha(\lambda)$ is the wavelength dependent waveguide propagation loss, in most cases governed by light scattering by waveguide roughness. Γ is the ratio of the optical mode field that overlaps with the analyte, calculated as:

$$\Gamma = \frac{\int_{cladd} |E|^2 \mathrm{d}x\mathrm{d}y}{\int \quad |E|^2 \mathrm{d}x\mathrm{d}y} \tag{3.5}$$

According to the equation 3.4, the strength of the absorption is strongly affected by the interaction path length, and absorption coefficient. Thus, one simple approach to enhance the light-matter interaction is increasing the waveguide length (folded beam path and micro ring resonators).

For the absorption-based sensor, when the guided light propagating in the waveguide is exposed to the media, a part of evanescent field is absorbed selectively by the functional group of analytes. The vibration frequencies of such functional groups of biochemical molecules generate the distinctive absorption wavelengths. Besides, the optical path length, concentration, and temperature affect the absorption intensity.

### 3.1.2 Sensor architectures

The architectures can be generally categorized in two different types: interferometric and resonant-based sensors. Figure 3.3 shows the schematic illustrations of these two architectures.

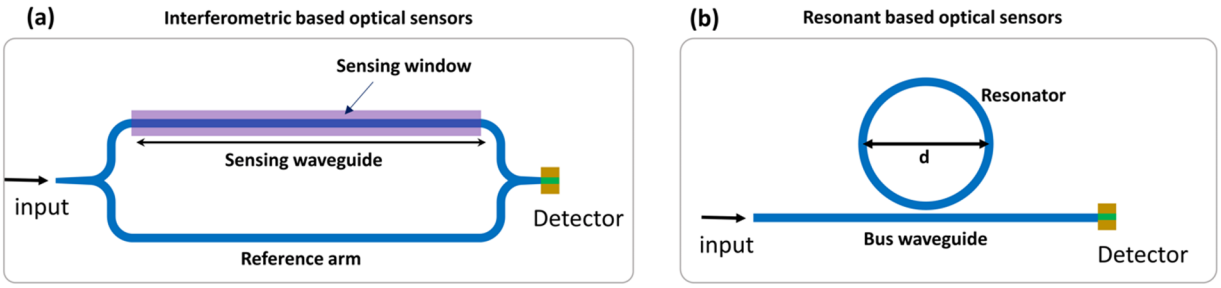


**Figure 3.3**: Schematic of (a) interferometric based optical sensors and (b) resonant based optical sensors.

### *Interferometric based Optical biosensors*

Interferometric sensors have been extensively studied using different interferometric architectures such as Mach-Zehnder [129], Young [129], [130], Biomodal [131], Hatman [132], and directional couplers [133]. Among them, the Mach-Zehnder interferometer is one of the most widely used for interferometric sensors. The schematic of the Mach-Zehnder interferometer (MZI) is illustrated in Fig. 3.3a. In principle, when the light travels in the waveguide, it is divided 50:50 into two separate paths using. One arm serves as the reference arm, and the other one serves as the sensing arm passing through the medium in which the evanescent field interacts with analysts. The light is then recombined at the output and generates the interferogram, which contains the phase difference. The phase difference $\Delta\varphi$ is determined by the interaction length $L$ of the arm and the effective index difference between the two arms [127]:

$$\Delta\varphi = \frac{2\pi L}{\lambda_0}\Delta n_{eff} \tag{3.6}$$

The architecture sensitivity is determined by:

$$Sa = \frac{\partial\varphi}{\partial n_{eff}} = \frac{2\pi}{\lambda_0}L \tag{3.7}$$

Where $\lambda_0$ is the central wavelength, $\Delta n_{eff}$ is effective index difference. Since the sensitivity depends on the interaction length, one direct strategy to improve the sensitivity is to increase the length of the arm which can be achieved using the spiral waveguides. In 1990s, Heideman et al. first introduced the biosensing application employing integrated MZIs. Till now, the development of MZI sensors has made significant progress. Various types of materials, such as $Si_3N_4$, $SiO_2$, Si, and polymers were employed successfully.

### *Resonant based Optical biosensors*

Besides the interferometer configuration, the resonant is also widely used for sensing applications. Several resonant-based structures have been developed, such as rings, Bragg

gratings [134], disks [135], and microspheres [136]. In principle, light is introduced into the optical cavity through the coupled evanescent field of the optical bus waveguide. The light in the optical cavity is transmitted multiple round trips before escaping the cavity. Such approach is beneficial in enhancing the interaction path length while maintaining compact size. It should be noted that the optical path length is determined by the Q-factor of the ring resonator, which is defined as the stored energy inside the resonator. Instead of increasing the physical length $L$ of the waveguide, we want to improve the number of round trips inside the ring, aiming to maximize the light-mater interaction. Q factor is considered as an important factor in resonant-based sensors which is defined as:

$$Q = \frac{\lambda_0}{\Delta\lambda_{FWHM}} \tag{3.8}$$

The effective length of the ring is determined by the Q factor, which is shown as:

$$L_{eff} = Q\frac{\lambda_0}{2\pi n_g} \tag{3.9}$$

Where $n_g$ is the group index, $\lambda_0$ is the resonant wavelength, $\Delta\lambda_{FWHM}$ is the FWHM bandwidth of the resonance peak. The intrinsic limit of detection (iLoD) is directly related to the Q factor and the device sensitivity S:

$$iLoD = \frac{\lambda_0}{Q \times S} \tag{3.10}$$

Several research studies have been working on resonant based sensors such as microspheres [136], microtoroids, microdisks [135], and ring resonators. Microspheres are generally made from silica or polymer to confine the light. The advantage of the microspheres is their very high Q factor, proving the great performance in sensing. However, this structure encounters limitations in mass manufacture and integration, making it not suitable for commercial fabrication because it has no standard in fabrication and it is difficult for repetition, and less compact for miniaturization. Meanwhile, the microdisk and microring resonators are recognized as suitable approaches for photonic biochemical sensors because of their design simplicity, compactness, and ease of manufacture.

### 3.1.2 Silicon waveguide geometries for sensing applications

Different strategies have been proposed aiming to enhance the light-matter interaction in the bio-chemical sensors, including varying waveguide geometries, different operating polarizations, and varying the operating wavelengths. In this section, we will present some general strategies. Table 3.1 summarizes the performance of different sensing configurations.

**Table 3.1**: Performance of different sensing configurations.

| Sensor configuration | Material platform | Strategy | Bulk sensitivity | Surface sensitivity | Limit of detection (LoD) | Ref. |
|---|---|---|---|---|---|---|
| MRR | SNOI | Slot | 212 nm/RIU | - | 2.3 $\times 10^{-4}$ RIU | [137] |
| MZI | SiN | Slot | - | 7.16 nm/(ng/mm$^2$) | 1.3 (pg/mm$^2$) | [138] |
| MRR | SOI | TM mode | 135 nm/RIU | - | $7\times10^{-7}$ RIU | [139] |
| Microdisk resonator | SOI | TM mode | 142 nm/RIU | - | $6.8\times10^{-4}$ RIU | [140] |
| MZI | SOI | TM mode | 460× $2\pi$ rad | - | 6 (pg/mm2) | [141] |
| MRR | SOI | Suspended | 310 nm/RIU | - | - | [142] |
| MRR | SOI | TM mode Suspended | 130 nm/RIU | - | $8\times10^{-4}$ RIU | |
| MRR | SOI | SWG | 400-500 nm/RIU | 800 pm/nm | $2\times10^{-6}$ RIU | [118] |
| MRR | SOI | Multibox SWG | 579.5 nm/RIU | 1900 pm/nm | $1.02\times10^{-3}$ RIU | [117] |

***Slot waveguide.***

The common structure has been widely used for sensing is the slot waveguide, which consists of a small slot filled with low refractive index material, sandwiched between two high index strips (rails). Compared to traditional strip waveguides, the interaction between incident light and cladding material can be significantly enhanced due to the strong confinement of the optical field in the small slot.

Since their proposal by Almeida et al. in 2004 [143], slot waveguides have been studied extensively in biochemical sensing applications. In 2007, Barrios group reported slot-waveguide microring resonator fabricated on $SiN_4$-$SiO_2$ platform, as shown in figure 3.4a [144]. This structure obtained the bulk sensitivity of 212 nm/RIU and LOD of $2.3 \times 10^{-4}$ RIU, designed for working wavelength of 1310 nm. In a follow-up study, a detailed analysis and discussion on an optical slot waveguide ring resonator array packaged for multiplex label-free

has been demonstrated by Carlborg et al [145]. The design, fabrication, and characterization of a packaged array of optical refractive index sensors integrated with microfluidic sample handling in a compact cartridge have been addressed (Figure 3.4b). This device achieved a volume refractive detection limit of $5\times 10^{-6}$ (RIUs) and a surface detection limit of 0.9 pg mm$^{-2}$. In ref [146], a slot photonic crystal waveguide provides the substantial overlap between the optical mode and the analyte, enables detecting changes in refractive index in a given analyte with high sensitivity. This results in a high sensitivity above 1500 nm/RIU, and the quality factor cavities can achieve up to 50000.

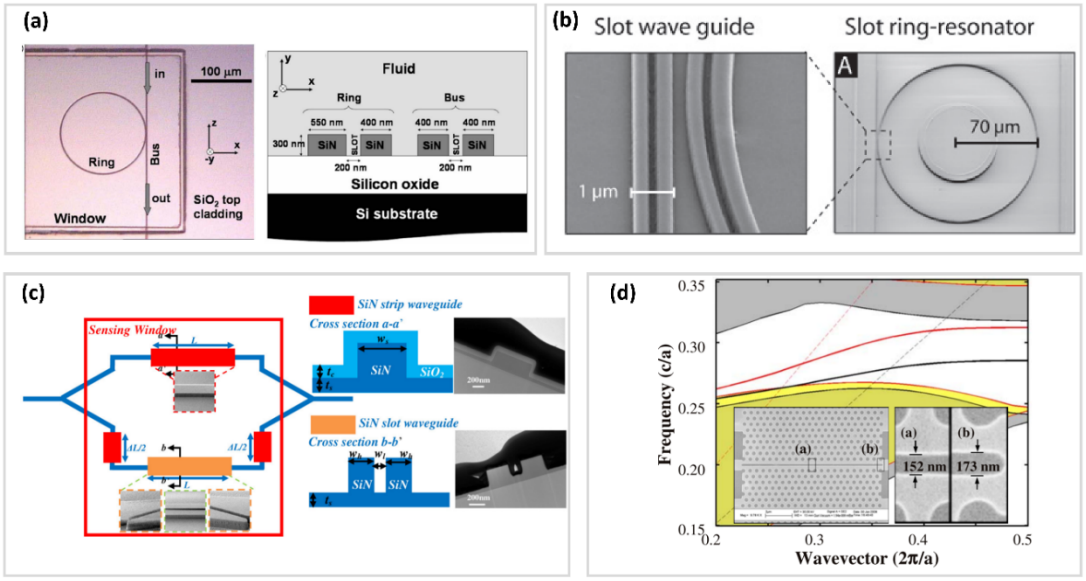


**Figure 3.4**: (a) Optical microscope photograph of a slot waveguide ring resonator and schematic cross section of the coupling region between the bus and the ring slot waveguide [144] ; (b) a slot-waveguide ring resonator with an expansion view of the coupling region [145]; (c) Cross sections schematics with plan-view of the athermal MZI biosensors [138]; (d) SEM image of a slot photonic crystal cavity with zoomed views of slots [146].

Apart from the microring resonator configurations, the slot waveguide was also applied to MZI sensors [138], [147]. A study of the silicon-nitride slot-waveguide MZI biosensor (Figure 3.4c) was carried out by Tu et al. in 2012 [138]. The device is developed to have low temperature dependence while maintaining high sensitivity and detection limits. The reported surface sensitivity and detection limit of the MZI biosensor with air cladding are 7.16 nm/ (ngmm2) and 1.30 (pg/mm$^2$) with a low temperature dependence of 5.0 pm/$^o$C.

### *TM mode*

Another common strategy to improve the evanescent field outside of the waveguide is using the TM polarized mode. For TE polarization, the majority of the electric field is concentrated in the core of the waveguide due to the strong index contrast of Si/SiO2. Thinner waveguide

thickness or TM polarization approaches are sometimes advantageous for sensing because they can provide stronger light-matter interaction. Different from TE polarization, a considerable portion of the optical field in TM mode is strongly localized near the top surface of the waveguide, which can be used to increase detection sensitivity. Several works have been used TM polarization for sensing, including both interferometric configuration [141], [148], [149] and resonant configuration[140], [150].

***Operating wavelength***

It is worth mentioning that the operating wavelength also affects the performance of different sensors. Water absorbs strongly at 1550 nm wavelength, which significantly limits the signal intensity, the Q factor, and therefore the LoD of aqueous sensing [151]. By adjusting the working wavelength to 1330 nm, where the water absorption is substantially less, this issue can be effectively addressed. As an example, Melnik et al. described detecting method of human IgG (hIgG) on integrated-optical Mach-Zehnder interferometer sensors working at 1310 nm [152]. It reported surface limit of detection (sLOD) of 0.03 nM for labeled methods. In 2020, Perez et al. have shown the light-matter interaction improvement in SWG, resulting in higher sensitivity in integrated photonics sensors for a working wavelength of 1310 nm. The sensor achieves a sensitivity of 507 nm/RIU and a quality factor of $4.9 \times 10^4$. Furthermore, the intrinsic inherent detection limit of $5.1 \times 10^{-5}$ RIU is a 10-fold improvement over state-of-the-art resonant waveguide sensors [151].

***Suspended waveguide***

When the light propagates in the waveguide, a large part of it penetrates substrate which has no interaction with the analyte. In addition, the conventional waveguides implemented on the standard platform yield an asymmetrical optical mode distribution, with a considerable part of the optical mode present underlying $SiO_2$ substrate being inaccessible for target analyte. Therefore, the suspended waveguide is a simple and effective way to enhance the overlap between the evanescent field and the target molecules. The suspended silicon ring resonators have already been developed to operate in the near-infrared and mid-infrared spectral bands. In 2006, L. Martinez et al. introduced the suspended ring resonator on the SOI platform [153]. This suspended waveguide achieved a high Q factor of 13 000 for TE polarization. Afterward, a suspended subwavelength waveguide operating at TM polarization has been experimentally demonstrated by G. Gaur et al [142]. This proposed structure can significantly improve bulk sensitivity by 3-fold and surface sensitivity by 2-fold. In addition, suspended waveguide is also considered as one of the potential solutions for SOI-based sensors at mid-IR wavelength, where $SiO_2$ is known to cause absorption at wavelengths greater than 4 μm, making conventional SOI impractical at the MIR wavelength. Then,

several groups have developed suspended waveguides as an alternative solution for mid-IR on-chip spectroscopy.

***Subwavelength waveguide***

In recent years, subwavelength metamaterial waveguide arises as a promising approach for manipulating light-matter interaction for application in sensing. The subwavelength waveguide structure with the alternative segments of dielectric materials allows flexibility in engineering the effective index of the waveguide, thereby, enables controlling the light confinement. The advantage of the metamaterial structure is the capability for improving the light-matter interaction as the mode in the SWG waveguide enters the evanescent field at a higher proportion as a result of its lower effective index, leading to higher sensing performance.

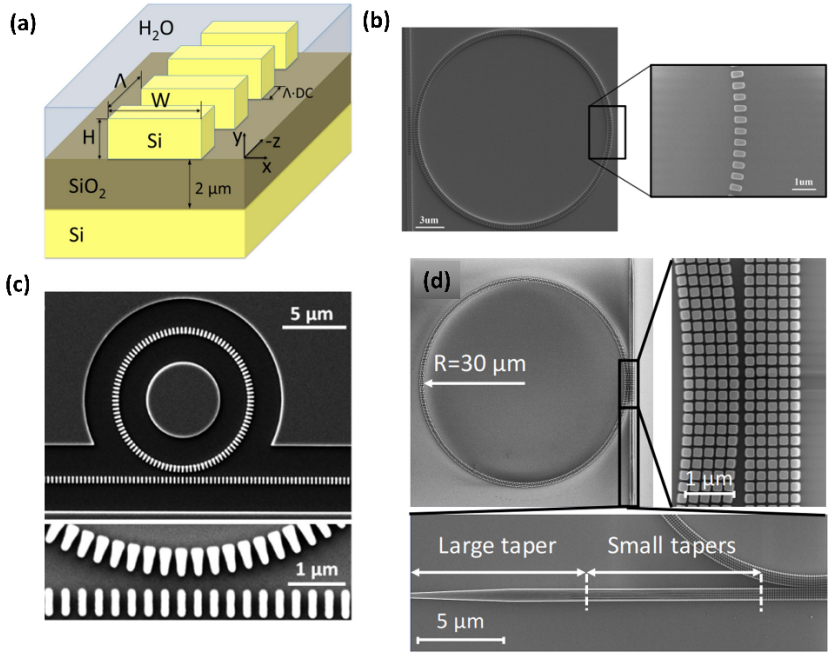


**Figure 3.5**: a) schematic illustration of the subwavelength waveguide for sensing application [119]; b) SEM image of SWG ring resonator [118]; c) SEM image of the fabricated trapezoidal silicon SWG micro-ring resonator (T-SWGMR) for improving the quality factor [102] ; d) SEM image of the 30 µm-radius multi-box ring resonator with five rows [117].

There is extensively study on subwavelength waveguide for biosensing applications. In 2014, Wangüemert-Pérez et al. first proposed subwavelength grating waveguide in SOI platform for sensing application (Figure 3.5a) [119]. They examined the effects of various duty cycles on sensing performance using a Fourier-type 2D vectorial simulation tool. Fully vectorial 3D-FDTD simulations validate the sensitivity improvement, with sensitivities of 0.83 RIU/RIU and $1.5\times10^{-3}$ RIU/nm for bulk and surface sensing, respectively. Latter work in 2016,

Flueckiger et al. presented how to engineer the effective refractive index and mode profile using subwavelength grating ring resonator sensor in silicon-on-insulator (SOI) platform [118] (shown in Figure 3.5b). The performance of SWG rings for biosensing is experimental demonstrated in this work, achieving the Q factor of 7000, the bulk sensitivities of 400 – 500 nm/RIU, and the LoD of $45\times10^{-4}$ RIU.

In order to improve the quality factor of the ring, trapezoidal silicon pillars were proposed instead of conventional rectangular silicon pillars for ring resonator [102] (Fig. 3.5d). This work demonstrated that using trapezoidal silicon pillars can generate an asymmetric effective refractive index profile which may greatly minimize bend loss and thereby improve quality factors. The 5 μm radius SWG ring resonator made of trapezoidal silicon pillars achieves the Q factor of 11,500 which is 4.6 times higher than that of standard SWG ring made of rectangular silicon pillars. Recently, a subwavelength multi-box waveguide ring resonator was proposed to enhance the sensitivity for label-free biosensors [117] (as shown in Figure 3.5d). The structures consist of several rows of periodic silicon box separated by 60 nm gap lengths to obtain better bulk and surface sensitivity than standard strip waveguides due to the large surface contact area and low optical confinement. They showed a bulk sensitivity of 579.5 nm/RIU and surface sensitivity of 1900 pm/nm. Despite the greatly enhanced sensitivity, this concept meets some limitations, i) the bulk iLoD of $1.02\times10^{-3}$ RIU and surface iLoD of $3.13\times10^{-1}$ nm are similar to conventional SWG and silicon based sensors due to the comparatively low observed Q value of 2600 in water, ii) this "multi-box" structure required the advanced lithography technique for fabricating the silicon photonics features down to 50 nm. In the following work, the approach of a multi box waveguide has been expanded with the integration of a Bragg-grating and a MZI-based sensing structure.

## 3.2 Dual-metamaterial silicon waveguides

### 3.2.1 Motivation

Many applications, like as sensing [126] and hybrid integration of active materials [154], [155], benefit from the ability to control the modal confinement in silicon nanophotonic waveguides. As mentioned in literature reviews, the use of subwavelength metamaterial engineering to shape modal confinement in silicon photonic waveguides has been emphasized as a promising approach. Different from photonic crystals which rely on resonant light confinement, SWG waveguides perform well below the bandgap, propagating light by metamaterial refractive index difference. This way, the SWG yields low propagation loss comparable to conventional waveguide in wide spectral bandwidth. In principle, the optical mode confinement may be modified at will simply by lowering the refractive index of the metamaterial. However, the loss due to leakage into the silicon substrate limits the minimum

metamaterial index and maximum achievable evanescent field in practice [156]. The majority of SWG waveguides rely on metamaterial engineering of either the core [157] or the cladding [158]–[160], but not both. The index of the cladding or core is fixed in these geometries, limiting the flexibility in adjusting modal confinement in perpendicular and parallel directions to the chip surface, respectively. In the waveguide with a subwavelength metamaterial cladding only, the evanescent field can be adjusted by manipulating the refractive index contrast between the waveguide core and cladding, and by engineering cladding anisotropy. However, the feasible evanescent field in the vertical dimension is restricted by the tight confinement in the core silicon strip. In waveguides with a subwavelength metamaterial core, on the other hand, lowering the metamaterial index enlarges simultaneously the mode in both vertical and horizontal directions. As a result, leakage into the silicon substrate due to excessive vertical expansion severely limits maximum evanescent field, while the latter can be lessened by increasing waveguide width. The single-mode operation does, nevertheless, limit the maximum waveguide width. Leakage into the substrate is a particularly significant concern when air acts as the top-cladding material (superstrate), and it is the case in gas sensing applications. Because of the large imbalance between the top and bottom cladding, there is a significant loss due to leakage into the substrate, which makes metamaterial waveguides with the nanostructured core problematic to utilize. This is particularly the case when considering the widely used silicon-on-insulator (SOI) technology, which features a 220-nm-thick silicon guiding layer and wavelengths close to 1.55 μm. This drawback could be overcome by removing the buried oxide (BOX) layer and replacing it with a silicon membrane with upper and lower cladding of air. For example, subwavelength membrane waveguides interleaving shifted silicon strips have recently been described to use different metamaterials in the core and cladding. However, the core and cladding shape are defined by the same silicon strips, restricting the design flexibility of the index contrast. Furthermore, membrane waveguides require complicated fabrication processes, thus compromising the mechanical stability of the device.

The strip waveguide, which operates in transverse-magnetic (TM) polarized mode, provides a comparatively large evanescent field with a weaker interaction with sidewall roughness, resulting in lower propagation loss, is the preferable choice for many sensing applications.

In this dissertation, we introduce and experimentally demonstrate a new waveguide geometry that incorporates different subwavelength metamaterials in the core and cladding [14]. This approach allows controlling independently the synthesized metamaterial indices in the core and cladding, releasing new degrees of freedom in tailoring modal confinement. In particularly, the metamaterial in the waveguide core determines the vertical index contrast, whereas the difference between the metamaterial indices in the core and cladding defines the lateral index contrast. We favor horizontal field expansion while allowing single-mode

operation for comparably broader waveguides by lowering the lateral index contrast. We relax constraints in the core metamaterial index due to leakage into the silicon substrate by extending the waveguide width and increasing the lateral expansion. To verify the feasibility of this approach, we fabricated dual-metamaterial waveguides in the SOI platform with a 220-nm-thick guiding silicon layer, working with TM polarization near 1.55 μm wavelength. Our simulations indicate that the proposed waveguide can operate in single mode for core widths as wide as 900 nm while obtaining greater overlap with the environment in comparison with the strip waveguide's TM modes.

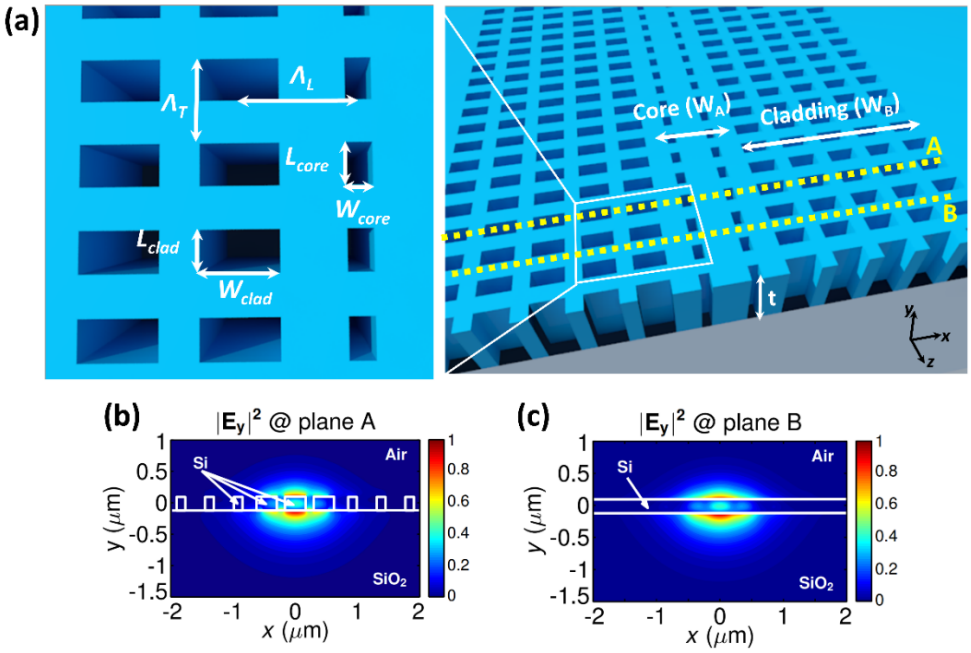


**Figure 3.6**: (a) schematic of the proposed dual-metamaterial waveguide; Electric field profile of the fundamental TM mode at wavelength of 1550 nm (b) the plane A and (c) plane B ($L_{core}$ = $L_{clad}$ = 100 nm, $W_{core}$ = 100 nm, $W_{clad}$ = 300 nm, $N_{core}$ = 2).

### 3.2.2 Design

Figure 3.6 shows the proposed dual-metamaterial waveguide geometry consisting of multiple holes placed at regular intervals within the core and cladding. The longitudinal ($\Lambda_L$) and transversal ($\Lambda_T$) periods of all the holes in the lattice are the same. The period in the proposed structure is designated small enough to enable subwavelength operation. The waveguide has $N_{core}$ holes in the core and $N_{clad}$ holes on each side of the cladding in longitudinal period. We used a silicon layer thickness of 220 nm and air as the upper cladding for the waveguide design.

The sidewall roughness effect affects the transverse-electric (TE) polarized modes, which can result in larger propagation loss. We decided to work with the TM polarized mode to get over this limitation. We used $\Lambda_L$ = 200 nm and $\Lambda_T$ = 450 nm as the longitudinal and transversal periods, respectively, to ensure mitigation of diffraction effects in the longitudinal and transversal directions. $N_{core}$ = 2 and $N_{clad}$ = 16 are the number of holes in the core and cladding, respectively. The length of the holes in the core and cladding is $L_{core}$ = $L_{clad}$ = 100 nm, resulting in a duty cycle of 50% in the longitudinal direction. The holes in the core are $W_{core}$ = 100 nm wide, whereas the holes in the cladding are $W_{clad}$ = 300 nm wide.

The proposed dual-metamaterial structure is studied using three-dimensional finite-difference time domain (3D-FDTD) simulations. Details of this simulation are presented in the previous chapter. The upper cladding had a refractive index $n_{air}$ = 1 while the buried oxide had a refractive value of $n_{BOX}$ = 1.44. The electric field distribution for the TM mode at the planes A and B, as specified in Figure 3.6a, is shown in Figure 3.6b and 3.6c. We observe that the evanescent field concentrates at the top and bottom silicon surfaces, interacting weakly with the vertical walls.

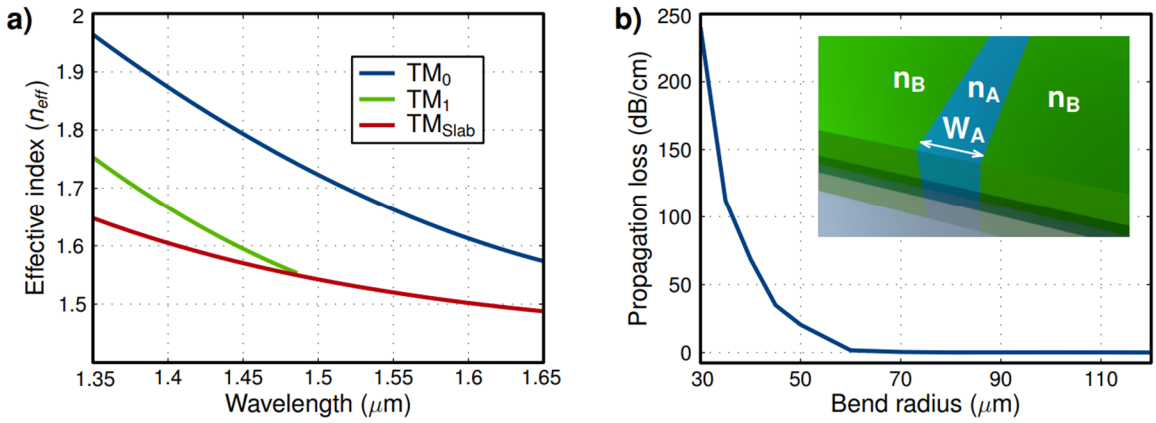


**Figure 3.7**: a) The calculated effective index of the fundamental and first order TM modes of the dual-metamaterial waveguide using 3D FDTD simulation ($\Lambda_L$ = 200 nm, $\Lambda_T$ = 450 nm, $N_{core}$ = 2, $N_{clad}$ = 16, $L_{core}$ = $L_{clad}$ = 100 nm, $W_{core}$ = 100 nm wide, and $W_{clad}$ = 300 nm); b) the propagation loss of the dual-metamaterial waveguide calculated as a function of the bending radius using the 2D model shown in the inset.

To determine single-mode range of the proposed waveguide, we begin by calculating the effective index of its fundamental and first order TM modes as a function of wavelength and compare them to the metamaterial cladding's effective index. Note here that the waveguide modes need to have a higher effective index than the metamaterial cladding to be guided. For wavelengths greater than 1.5 µm, the waveguide with a width of 900 nm (transversal period

$\Lambda_T$ = 450 nm and $N_{core}$ = 2) yields single mode operation, as shown in Fig. 3.7(a). Meanwhile, the maximum waveguide width for single-mode operation for TM strip is ~ 600 nm.

To estimate the minimum bending radius of the dual-metamaterial waveguide we use the two-dimensional (2D) waveguide model, presented in the inset of Fig. 3.7(b). In this 2D model, the metamaterials in the core and cladding are substituted by their equivalent effective index ($n_A$ = 3.34, $n_B$ = 3.04 for TM polarization at 1550 nm wavelength). The results obtained with the 2D model are less accurate than those obtained with 3D-FDTD calculations. Still, they stand as a simple and valid means to study the behavior of the waveguide and considerably simplifes the calculation of the bending loss. In Fig. 3.7(b) we plot the propagation loss bend as a function of the radius for $W_A$ = 900 nm (corresponding to $\Lambda_T$ = 450 nm and $N_{core}$ = 2). The minimum radius to yield negligible bending loss is 70 μm. This minimum bending radius could be reduced by lowering the metamaterial cladding at the outer part of the bend. This could be seamlessly achieved by increasing the hole size in this region.

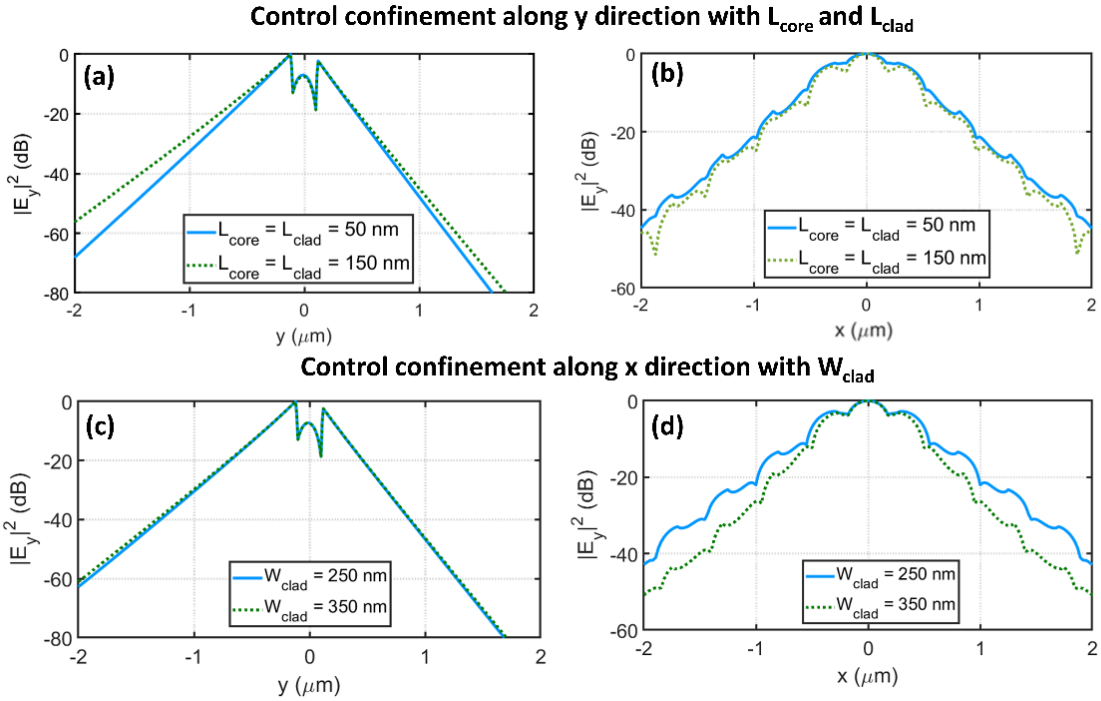


**Figure 3.8**: Example of independent control of vertical and lateral confinement (a) vertical and (b) horizontal electric field distribution for different values of $L_{core}$ and $L_{clad}$. ($N_{core}$ = 2, $N_{clad}$ = 16, $L_{core}$ = $L_{clad}$ = 100 nm, $W_{core}$ = 100 nm, $W_{cladd}$ = 300 nm). (c) vertical and (d) horizontal electric field distribution for different values of $W_{clad}$ ($N_{core}$ = 2, $N_{clad}$ = 16, $L_{core}$ = $L_{clad}$ = 100 nm, $W_{core}$ = 100 nm, $W_{clad}$ = 300 nm).

Figure 3.8 shows the independent control of electric field distribution of subwavelength along the vertical and horizontal direction independently. It is feasible to tune the vertical confinement by changing the gap length in the core ($L_{core}$) and cladding ($L_{clad}$), with minimal

influence on the lateral confinement. On the other hand, changing the width of the holes in the cladding ($W_{clad}$), has almost no impact on vertical confinement (Fig. 3.8c) but has a significant influence on lateral confinement (Fig. 3.8d). This simulation proves the capability of metamaterial waveguide in shaping the light confinement in vertical and horizontal direction.

We also compare the field distributions for the TM modes of the strip and dual metamaterial waveguides along the horizontal and vertical directions in Fig. 3.9b and 3.9c. We examined two waveguide widths for the strip waveguide: 350 nm and 550 nm. The optical mode in the 350 nm width is strongly evanescent, with an effective index of 1.45 near the cut-off limit. The 550 nm waveguide width is near to the single-mode limit (600 nm), yielding a strongly confined optical mode. Along the vertical direction, the proposed dual-metamaterial waveguide has a field profile that resembles that of a highly confined strip waveguide (W = 550 nm). However, in the horizontal direction, the field profile of the dual-metamaterial waveguide is similar to that of the highly evanescent strip waveguide (W = 350 nm). This particular field distribution demonstrates the versatility in field confinement engineering of the proposed dual-metamaterial waveguide.

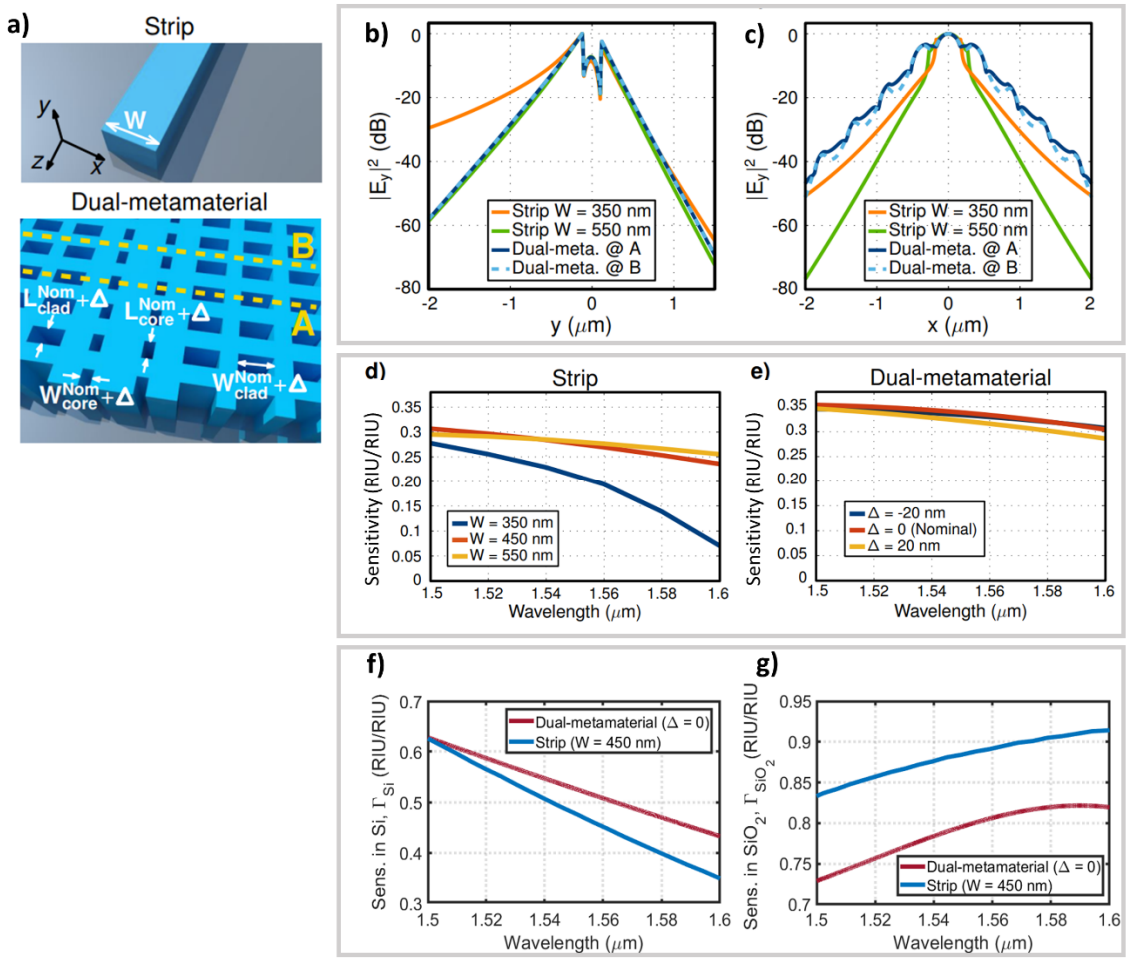


**Figure 3.9**: a) Schematic of the strip and dual-metamaterial waveguides; comparison of the electric field distributions along of b) vertical and c) horizontal dimensions for the strip waveguide and proposed dual-metamaterial waveguide. Comparison the bulk sensitivity in the air between d) strip waveguides and e) dual-metamaterial waveguides. Calculated the bulk sensitivity of the strip and dual-metamaterial waveguides in f) silicon core and g) silica under cladding.

To determine the performance of the proposed dual metamaterial, we calculated the bulk sensitivity (Eq. 3.1) and compared with the strip waveguide operating at TM polarization near 1550 nm. Figure 3.9d and 3.9e show the bulk sensitivity as a function of wavelength. Strip waveguides are modeled using a 2D finite-difference eigenmode solver, while dual-metamaterial waveguides are investigated using 3D-FDTD simulations. We examined three different waveguide widths for the strip waveguide: 350 nm, 450nm, and 550 nm. For the dual-metamaterial, we take into account the nominal design ($L_{core}$ = $L_{clad}$ = 100 nm, $W_{core}$ = 100 nm, $W_{clad}$ = 300 nm, $N_{core}$ = 2) as well as geometrical changes caused by fabrication imperfections. $L_i = L_i^{Nom} + \Delta$ and $W_i = W_i^{Nom} + \Delta$ are the length and width of the holes in the core and cladding, respectively, and Δ describes the deviation from the nominal dimension. The dual-metamaterial waveguide has a higher bulk sensitivity in air than the strip

waveguide, as illustrated in Figs 3.9d and 3.9e. The sensitivity of the dual-metamaterial waveguide is highly robust to fabrication defects, with deviation below 0.01 for errors as large as 10 nm. The dual-metamaterial waveguide exhibits higher bulk sensitivity in silicon than the strip waveguide, as seen in Figure 3.9f, particularly for longer wavelengths. In comparison to the dual-metamaterial waveguide, the strip waveguide has increased bulk sensitivity in the bottom silica cladding (see Fig. 3.9g). The dual-metamaterial waveguide's higher bulk sensitivity in air and silicon is due to a combination of a large external field in the horizontal direction (Figure 3.9c) and a controlled confinement in the vertical direction (Figure 3.9b), prevents leakage towards the silica cladding, which is a major limitation in the case of air cladding.

### 3.2.3 Experimental characterization

We have fabricated and experimentally investigated several dual-metamaterial waveguides. We used 200 mm SOI wafers with a 220-nm thick guiding silicon layer and a 3 μm thick BOX layer to make the micro-ring resonators. Electron beam lithography was used to define the patterns. A single-step reactive ion etching procedure was used to transfer the patterns into silicon.

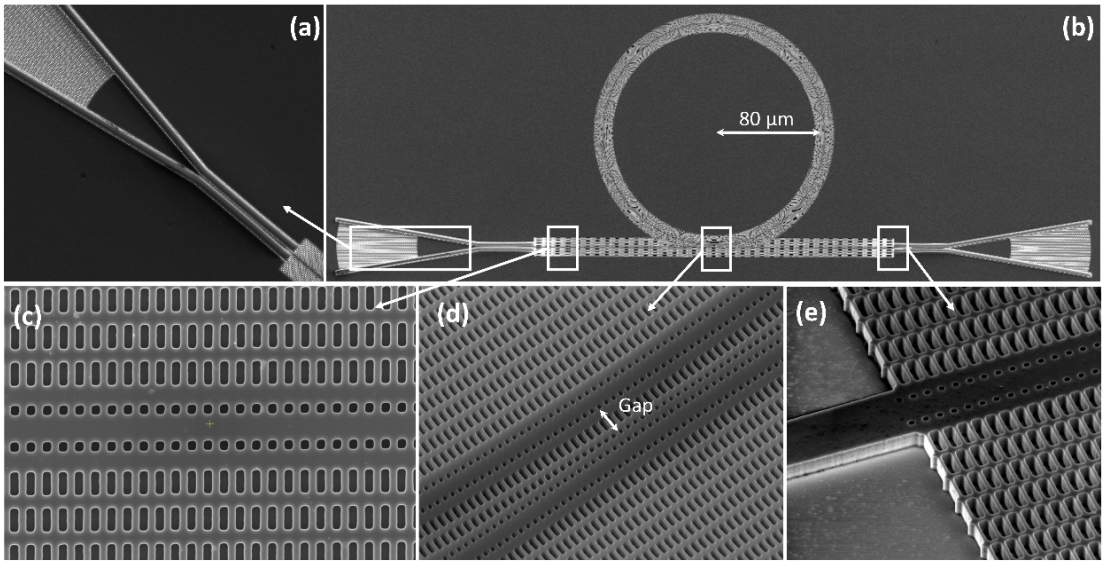


**Figure 3.10**: SEM images of the complete ring resonator (a) fiber-chip grating coupler (b) entire dual-metamaterial micro-ring resonator; (c) dual-metamaterial waveguide, (d) coupling region between bus waveguide and ring resonator; (e) transition between grating coupler and metamaterial waveguide.

For applications in sensing, achieving a high quality factor is highly desired for enhancing light-matter interaction in ring-resonator. High quality factors require not only low

propagation loss, but also low bending loss and low coupling loss between the bus waveguide and the ring resonator. The TM polarized light is injected into the chip from a continuous-wave tunable laser source using single-mode fibers (SMF-28) and polarization rotator. At the input and output of the chip, fully etched subwavelength engineered fiber-chip grating couplers adapted for TM polarization (pitch of 1.2 μm, duty cycle of 0.5, and coupling efficiency of -10 dB) are used. The strong polarization dependence grating couplers and the three-paddle polarization controller ensure that negligible TE-polarized light is introduced into the device (40 dB rejection). The transition between the strip and the dual-metamaterial waveguide is shown in Figure 3.10(e). In the beginning, the holes in the core have a length of 50 nm and width of 50 nm, while the holes in the cladding have a size of 150 nm × 400 nm. The size of the holes is increased adiabatically along 30 μm long taper to reach the values of the dual-metamaterial waveguide. This transition has a measured insertion loss lower than 1.5 dB. The transmission spectra were scanned using CT400 Yenista with a resolution of 1 pm near 1550 nm wavelength. For the nominal dual-metamaterial waveguide, we use geometrical parameters: $\Lambda_L$ = 200 nm, $\Lambda_T$ = 450 nm, $L_{core} = L_{clad}$ = 100 nm, $W_{core}$ = 100 nm, $W_{clad}$ = 300 nm, $N_{core}$ = 2 and $N_{clad}$ = 16. The waveguide width for strip resonators is 450 nm. Both the dual-metamaterial and strip ring resonators have an 80 μm radius. We changed the spacing between 500 and 720 nm in both types of resonators.

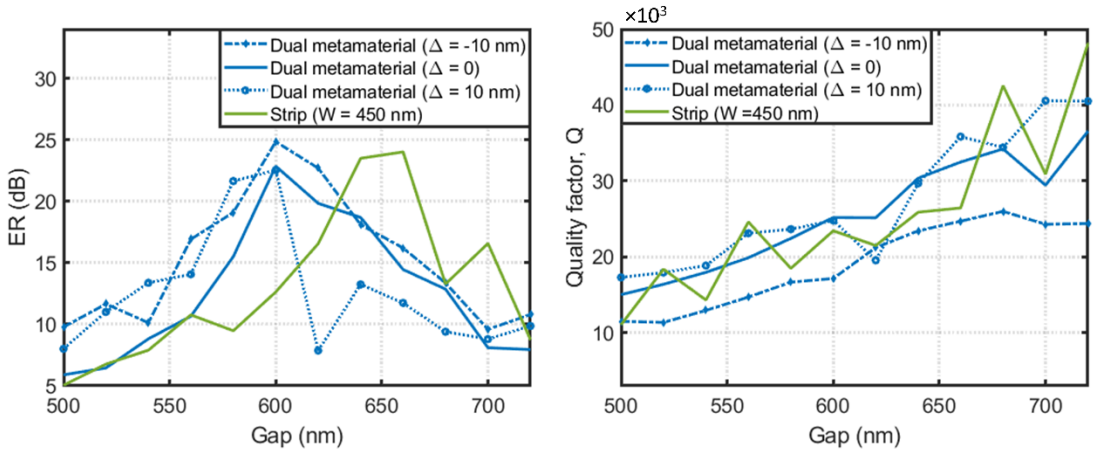


**Figure 3.11**: Comparison of measured (a) extinction ratio and (b) quality factor between dual-metamaterial- based ring resonators (nominal Δ = 0, and Δ= ± 10 nm) and strip-based ring resonator (W = 450 nm).

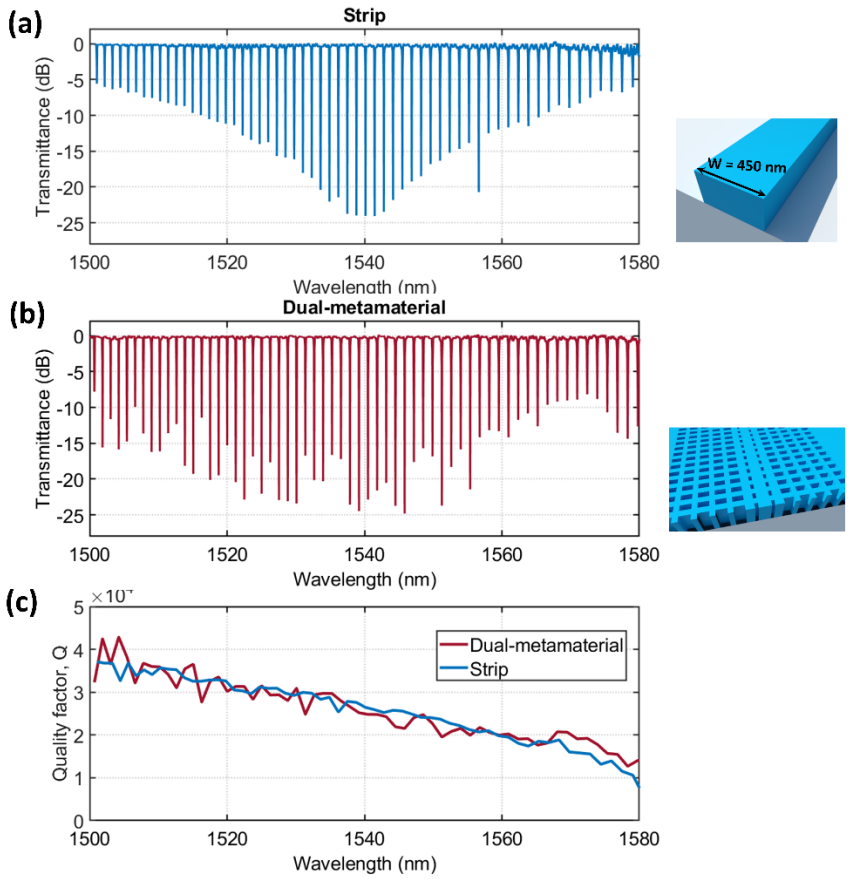


**Figure 3.12**: Comparison of spectral response of (a) dual-metamaterial (nominal $\Delta = 0$) and (b) strip waveguide (W = 450 nm), both at critical coupling with a gap between bus waveguide and resonator of 600 nm, and radius of 80 µm.

Figure 3.11 compares the measured extinction ratio (Figure 3.11a) and loaded quality factor (Figure 3.11b) as a function of the gap between the ring and the bus waveguide for dual-metamaterial ring resonators and a strip ring. The quality factors of the dual-metamaterial rings are comparable to those of the strip rings, as shown in Figure 3.11b. The critical couplings are achieved in three dual-metamaterial design for a gap of 600 nm, with the extinction ratio of 25 dB, which is comparable to the strip case. The quality factor increases monolithically with the gap width in all cases. This could be explained by the fact that coupler loss is lower at longer spacing. The transmittance spectrum of the dual-metamaterial ring is shown in Figure 3.12a, with a free-spectral range (FSR) approximately 1.4 nm at 1540 nm wavelength without observations of multimode activity. We compute a group index of 3.5 based on the observed FSR, which is in good agreement with the calculated value of the fundamental TM mode (3.4). Both strip and dual-metamaterial rings display similar quality factors in the observed wavelength range, as illustrated in Figure 3.12c. In comparison to strip waveguide, these findings reveal that the proposed dual-metamaterial waveguide has no penalty in quality factor.

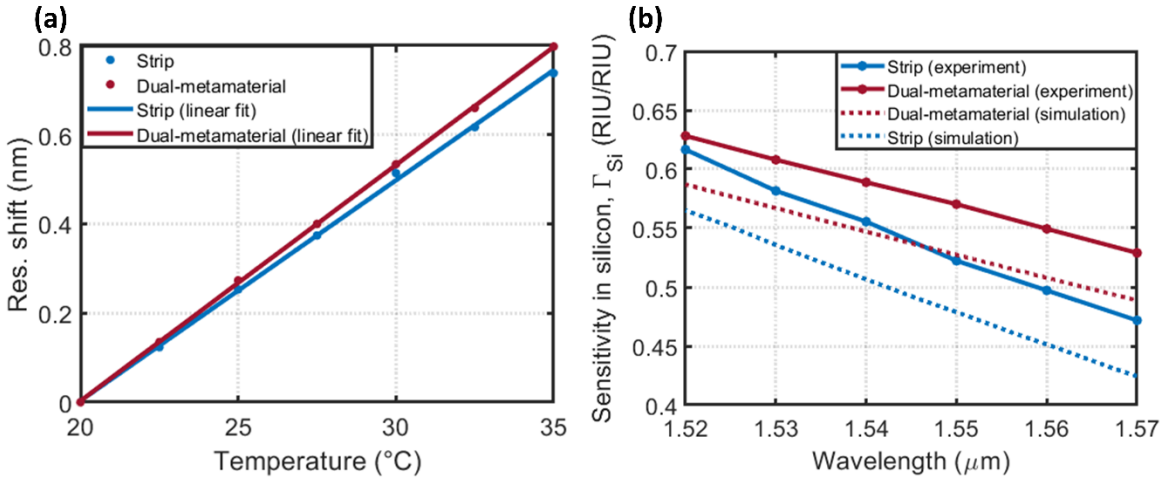


**Figure 3.13**: a) Measured wavelength resonator shift with the temperature for strip and dual-metamaterial ring resonators at the wavelength near 1550 nm, b) comparison of the simulation and experiment bulk sensitivity of the strip and dual-metamaterial resonators.

We conducted a refractive index sensing experiment to validate our modeling results, taking advantage of the substantial thermal dependency of the refractive index of silicon. We employed a Peltier device to control the chip temperature, producing a shift in the resonance wavelength of the strip and dual-metamaterial rings resulting from a change in the refractive index of silicon. To experimentally recover the bulk sensitivity in silicon (Si), we monitored the thermally induced resonance shift. In figure 3.13, we plot the measured resonance shift with the temperature as a function of the wavelength of the dual-metamaterial and strip rings described in Figure 3.13a. The temperature-induced resonance shift is calculated by fitting the resonance wavelength shift, which was recorded at temperatures ranging from 20 to 35 degrees Celsius. To experimentally recover $T_{Si}$ from the measured temperature-induced resonance shift, we use the observed free-spectral range to estimate the group index and a thermo-optic coefficient for silicon of $dn_{Si}/dT = 1.9\times10^{-4}$ $^{o}C^{-1}$ [161]. The experimental and computed findings are in good agreement, indicating the superior sensitivity in the dual-metamaterial ring. The 10% difference between simulated and experimental findings might be due to manufacturing imperfections.

## 3.3 Suspended dual-metamaterial waveguide

### 3.3.1 Motivation

In the previous part, we have demonstrated the feasibility in shaping the light confinement using dual-metamaterial waveguides. We continue exploiting the proposed dual-metamaterial structure to further enhance the overlap of the optical field and analytes, and hence enhancing the bulk sensitivity. The conventional waveguides implemented on the

standard SOI platform yield an asymmetrical optical mode distribution, with a considerable part of the optical mode present underlying $SiO_2$ substrate being inaccessible for target analyte. In this part of the thesis, the dual-metamaterial structure will be further investigated for maximizing the light-matter interaction by using full suspended waveguide operating in TM mode. This structure not only takes advantage of the flexible mode profile control, but also doubles the sensitivity compared to the previous structure, proving excellent capabilities for application sensing while maintaining a high Q factor.

### 3.3.2 Design

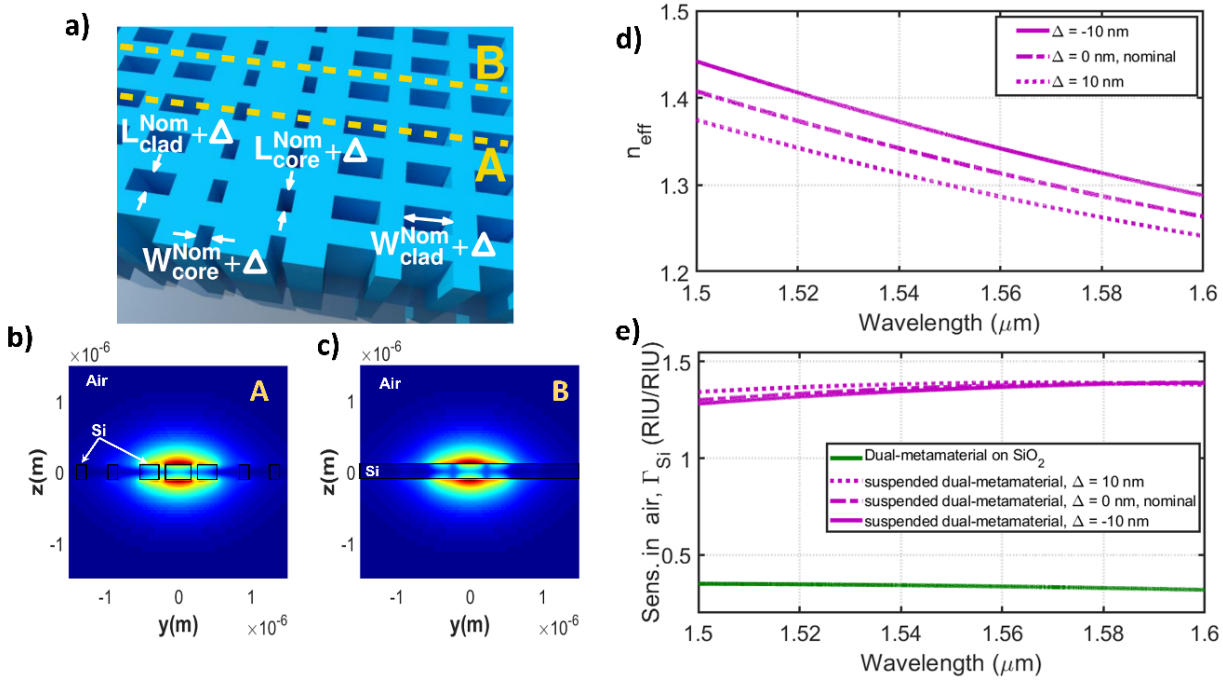


**Figure 3.14**: a) Schematic of the dual-metamaterial waveguide. Electric field distribution of the fundamental TM mode b) at the plane A and c) at the plane B with the defined parameters: $N_{core}$ = 2, $N_{cladd}$ = 16, $L_{core}$ = $L_{cladd}$ = 100 nm, $W_{core}$ = 100 nm, $W_{cladd}$ = 300 nm. d) Calculated effective index of the suspended dual-metamaterial waveguides; e) calculated bulk sensitivity of the suspended dual-metamaterial waveguides and dual-metamaterial on silica bottom cladding.

The suspended structure used in this section is similar to the dual-metamaterial on silica bottom cladding in the previous part which is shown in Figure 3.14a with the longitudinal period $\Lambda_L$ of 200 nm and transversal period $\Lambda_T$ of 450 nm. The number of the hole in the core and cladding are $N_{core}$ = 2, $N_{cladd}$ = 16, respectively. The nominal designs have the length of $L_{core}$ = $L_{cladd}$ = 100 m, the width of the core $W_{core}$ = 100 nm, while the width of the cladding $W_{cladd}$ = 300 nm. Figures 3.14b and 3.14c show the field profile of the suspended dual metamaterial subwavelength waveguide work with fundamental TM polarized mode. The optical field are strong on top and bottom surface of the waveguide, while the presence of the

electric field in the gaps is negligible. Thus, this structure enables enhancing the mode overlap with the analyte while not being greatly affected by sidewall roughness. By removing the silica under cladding, the proposed waveguide generates a symmetrical optical distribution that allows molecules to interact with both the top and bottom field profile. The simulation results show that the fraction of achievable optical field extending into the surrounding medium is above 70%.

To illustrate the advantage of the proposed structure in sensing applications, we calculated the bulk sensitivity of the suspended dual metamaterial waveguides using 3D-FDTD model. Figure 3.14d presents the calculated effective index of the suspended waveguide as a function of the wavelength. The effective indices of the suspended waveguide decrease overall with increasing wavelength, proving that the mode confinement is weaker. The less confinement of the guided mode leads to expand the evanescent field, and then enhance the overlap with the target molecules. As the consequence, the bulk sensitivity increases significantly. As shown in figure 3.14e, the bulk sensitivities of the suspended dual-metamaterials achieve approximately $\Gamma \sim 1.35$ at 1550 nm, which is 3.5 and 4.5 times higher compared with the dual metamaterial on silica bottom cladding $\Gamma \sim 0.35$ (displayed in Figure 3.9e), and the conventional strip waveguide $\Gamma \sim 0.28$ (W = 450 nm). This simulation results reveal that the proposed structure yield great bulk sensitivity, exhibit the excellent capability for sensing application.

### 3.3.3 Experimental characterization

This suspended dual-metamaterial micro ring resonators were fabricated with similar steps like the previous part, except that in the last step, we use HF evaporation to remove the silica under-cladding. Figure 3.15 shows the SEM images of the suspended micro-ring resonator fabricated in C2N cleanroom. The grating couplers at the input and output were designed to be optimized for TM polarization (Fig. 3.15b). For the transition between the grating coupler to dual-metamaterial, we used interconnecting waveguides with subwavelength-grating serving as cladding to support core waveguides mechanical, as shown in Fig. 3.1c. The ring radius is 80 µm to minimize the bending loss, the coupling gap between bus waveguide and ring varies from 500 nm to 1100 nm.

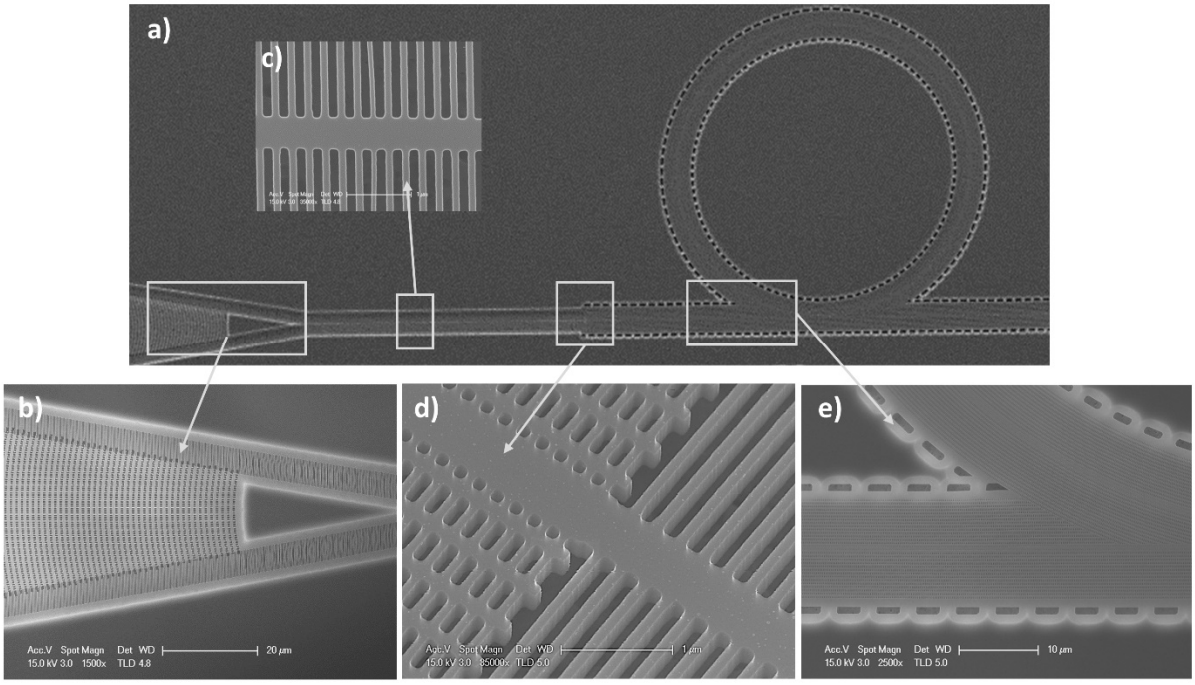


**Figure 3.15**: SEM images of a) the overall suspended dual-metamaterial micro-ring resonator; b) fiber-chip grating couplers, d) waveguides transition between grating coupler and dual-metamaterial waveguide; e) coupling region between bus waveguide and ring resonator.

The microring resonators are characterized using continuous-wave tunable laser source. The single-mode fiber and polarization rotator was used to inject TM polarized into the chip. Figure 3.16 shows the measured loaded quality factor and extinction radio of the ring resonator for the gap of 900 nm. The suspended dual-metamaterial yields the quality factor ~ 20 000 near critical coupling region, the maximum extinction ratio of 25 dB. In comparison with the dual metamaterial on silica cladding bottom, the suspended waveguide ring resonator achieves comparable quality factor and extinction ratio.

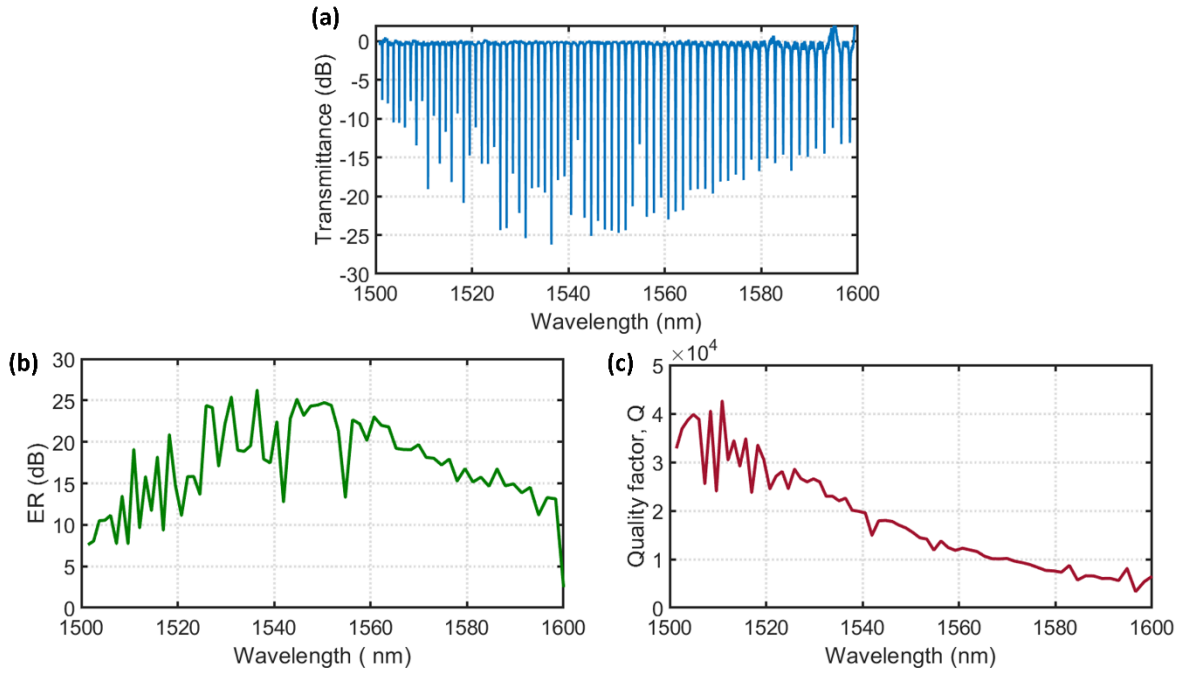


**Figure 3.16**: a) Measured transmission spectral of the suspended dual-metamaterial micro-ring resonator at critical coupling with radius of 80 µm, the coupling gap of 900 nm, b) Measured extinction ratio and c) loaded quality factor as the function of the wavelength.

## 3.4 Conclusions

We presented and experimentally validated a novel type of nanophotonic waveguide that allows for adjustable control of modal field confinement by incorporating two different metamaterials in the core and cladding [14]. The dual-metamaterial design offers new degrees of freedom for shaping vertical and horizontal index contrast separately, as well as for engineering the single-mode condition. The vertical index contrast is determined by the metamaterial index in the core, whereas the horizontal index contrast and single-mode conditions are governed by the difference between the metamaterials in the core and cladding. With careful design of the holes in the subwavelength lattice by a single etching process, the indices in the core and cladding can be adjusted with high precision and flexibility. The dual metamaterial waveguide allows for the seamless implementation of wider single-mode waveguides with tailored vertical and horizontal evanescent fields, maximizing overlap with the analyte while avoiding substrate leakage limits.

We have developed dual-metamaterial ring resonators working with TM polarization in SOI wafers with a 220-nm-thick guiding silicon layer, 3 µm-thick BOX, and air as a cladding to demonstrate the potential of this concept. Due to significant propagation loss resulting from leakage into the silicon substrate, the implementation of slot and traditional SWG metamaterial geometries is hindered by the thin silicon guiding layers and asymmetric

cladding. As a result, strip waveguides are the preferred choice for applications where air acts as the top cladding, such as gas sensing. Recent theoretical studies indicated that, although having greater external confinement factors, slot and SWG metamaterial waveguides perform worse than strip waveguides in terms of sensing performance due to increased propagation loss, regardless of the cladding material. According to our 3D-FDTD simulations, the TM mode of our dual-metamaterial waveguide provides a higher external confinement factor in the air (0.35) than strip waveguides with TM polarization (0.3). Besides this, the vertical confinement of the dual-metamaterial waveguide is equivalent to that of the strip waveguide, circumventing the substrate leakage loss of the slot and SWG waveguides. Our experiments confirmed that strip and dual-metamaterial ring resonators perform similar quality factors of around 30,000. The proposed dual-metamaterial metamaterial ring resonators are the promising alternative to conventional strip waveguides since they have similar quality factors and a greater bulk sensitivity. We also validated our simulation results by experimentally measuring the wavelength resonant shift with temperature variation.

The described dual-metamaterial waveguide was further investigated, aiming at maximizing the overlap of the optical field with the surrounding medium by exploiting the full suspended waveguide. By removing the silica bottom cladding using HF vapor, we successfully fabricated the suspended subwavelength waveguide designed for TM polarization. This freestanding micro-ring resonator performs excellent bulk sensitivity of 1.35, which is 3.5-fold and 4.5-fold times higher than that of dual-metamaterial structure on silica cladding and conventional strip waveguide, while remaining at a high loaded quality factor of 20 000 at critical coupling with the extinction ratio of 25 dB.

The proposed dual-metamaterial approach offers an entire new set of capabilities for engineering the index profile in silicon waveguides that would otherwise be unachievable in state-of-the-art strip, slot, or SWG metamaterial geometries. The dual-metamaterial structure, for example, allows for asymmetric index contrast with distinct cladding metamaterials on either side of the waveguide, or graded index contrast with the effective metamaterial index progressively varying between the core and the cladding. These configurations might be used to minimize the minimum bending radius and further relax single-mode conditions, as an example. Furthermore, multiple designs might be simply combined within the same silicon circuit with only a single etch process. The adjustable index contrast engineering enabled by the proposed dual-metamaterial structures could be useful for applications requiring large evanescent fields, such as sensing, but it could also be useful for improved dispersion and confinement engineering in nonlinear applications. The concept of a suspended structure can be further expanded for use in the longer mid-IR region. We believe that these findings pave the way for the realization of advanced modal confinement and dispersion engineering in silicon photonic devices.

# Chapter 4: Fourier transform spectrometer

Miniaturized silicon photonics spectrometers have a great potential for mass market applications, ranging from medicine, biological and environmental sciences to astrophysics and telecommunication [162]. This chapter is devoted to the study of the spatial heterodyne Fourier transform spectrometers (SHFTS) implemented in silicon for near-IR (section 4.2) and mid-IR wavelengths (Section 4.3). This chapter is divided into four sections. Section 4.1 comprises a brief review of different kinds of on-chip Fourier transform spectrometers (FTS) including SHFTS, temporal heterodyne FTS, and standing wave FTS. In Section 4.2, we introduce a novel approach to improve the throughput of integrated SHFTS. Based on this approach we demonstrated, for the first time, an integrated silicon SHFTS exploiting the Jacquinot's advantage. The SHFTS is implemented in silicon with integrated Ge photodetectors, and operates at near-IR, with wavelength near 1550 nm. In Section 4.3, we develop a mid-IR SHFTS using silicon suspended waveguides with subwavelength cladding. The SHFTS is demonstrated in the 5-6 μm wavelength range. This is the longest wavelength reported for a silicon SHFTS. General conclusions are summarized in Section 4.4.

## 4.1 The state of the art of integrated Fourier transform spectrometers

Free-space optical FTS use bulk optical elements leading to large-scale, unstable, and high-cost devices. Conversely, on-chip integrated FTS, have a unique potential to provide unprecedented compactness, high robustness, and large-volume, low-cost fabrication, key for widespread deployment of spectroscopy-based applications in medicine, environmental monitoring, or industry process control, among others. An alternative approach to FTS is wavelength demultiplexing based on dispersive elements. Most common dispersive-based approaches, include arrayed waveguide gratings (AWG) [163], waveguide echelle gratings [164] or cascaded micro-ring resonators [165]. These devices present some important disadvantages that limit their performance in terms of sensitivity to fabrication imperfections and environmental conditions, signal-to-noise ratio (SNR) and optical throughput. Most of these limitations are overcome with SHFTS [166]–[172], which provide the high SNR and optical throughput of conventional FTS [173], while obviating the need of moving elements or heaters [174].

**Table 4.1**: Summary of the key figures of merit for integrated FTSs. SWIFT: stationary wave integrated Fourier transform, TO-FTS: Thermo-optic Fourier transform spectroscopy, TT-SH-FTS, EO: Electro-optic.

| Design | Platform | Central wavelength (nm) | Spectral resolution | Bandwidth | Input | Ref. |
|---|---|---|---|---|---|---|
| SWIFT | SOI | 1550 | 4 nm | 96 nm | single | [169] |
| SWIFT | $Si_3N_4$ | 895 | 6 nm | 100 nm | single | [170] |
| TO-FTS | - | 1550 | 9.6 nm | 150 nm | multiple, excited one by one | [48] |
| TO-FTS | SOI | 1584.6 | 0.47 nm | 90 nm | single | [175] |
| SHFTS | SOI | 1365 | 0.025 nm | 2.5 nm | multiple, excited one by one | [176] |
| SHFTS | SOI | 1550 | 0.04 nm | 0.75 nm | single | [166] |
| SHFTS | Si-SWG | 1550 | 0.048 nm | 0.78 nm | single | [177] |
| SHFTS | SOI | 3750 | 2.7 nm | 57 nm | single | [178] |
| TT-SH-FTS | SiGe | 7700 | 88.9 nm | 3575.2 | multiple, excited one by one | [179] |
| EO-SWIFT | Thin film Lithium niobate-silicon nitride (LN) | 1550 nm | 5.5 nm | 500 nm | single | [180] |
| SHFTS | SOI | 1570 nm | 80 pm | 600 pm | Multiple, excited simultaneously | This PhD [15] |
| SHFTS | Suspended silicon | 5.5 µm | 50 nm | 300 nm | multiple, excited one by one | This PhD [16] |

### 4.1.1 Spatial heterodyne Fourier transform spectrometers (SHFTS)

The SHFTS architecture was proposed by P. Cheben in 2007, as an integrated alternative to benchtop free-space Fourier transform spectrometers [176]. As an example, Figure 4.1 compares the architectures and working principle for FTS based on free-space Michelson interferometer (Fig. 4.1a) and integrated SHFTS (Fig. 4.1b). In Michelson-based FTS, the physical length of one arm of the interferometer is varied with a moving mirror to from an interferogram. The input spectrum is retrieved from the interferogram by inverse Fourier transform [181]. Bandwidth and resolution of the retrieved spectrum are governed by the Nyquist-Shannon criterion, i.e. the bandwidth is determined by the sampling frequency (related to separation between sampling points) and the resolution is determined by the size of the interferogram (number of points). Hence, the maximum bandwidth is determined by the minimum achievable size of the steps used to vary the mirror position, while the resolution is determined by the maximum mirror displacement that can be implemented. The SHFTS implements a conceptually similar approach. Instead of moving a mirror to vary the optical path length difference between the arms of one interferometer, the SHFTS utilizes an array of MZIs, each with a different optical path length difference. The path-length difference increases linearly along the MZI array. This way each MZI in the SHFTS array is equivalent to one mirror position in the Michelson-based FTS. The outputs of all the MZIs form an interferogram from which the input spectrum is retrieved by inverse Fourier transform [178]. The SHFTS does not require moving parts and collects the full interferogram at the same time, which is advantageous in terms of noise. In addition, this MZI array is compatible with a multi-aperture architecture, with each MZI connected to a different input waveguide, which can be advantageous in terms of optical throughput (Jacquinot's advantage). The achievable bandwidth, also referred as free-spectral range (FSR), and resolution ($\delta\lambda$) are determined by the number of MZIs ($N$) and the maximum path length imbalance ($\Delta L_{max}$) by [166]:

$$\delta\lambda = \frac{\lambda_0^2}{\Delta L_{max} n_g} \tag{4.1}$$

$$\mathrm{FSR} = \delta\lambda \frac{N}{2} \tag{4.2}$$

with $\lambda_0$ the central wavelength and $n_g$ the group index of the integrated waveguides in the MZI. The maximum optical path length imbalance ($\delta\lambda$), that can be implemented is limited by propagation loss, while the maximum number of MZIs ($N$) is limited by footprint. Hence, the design of SHFTS is constrained by trade-offs between bandwidth and resolution.

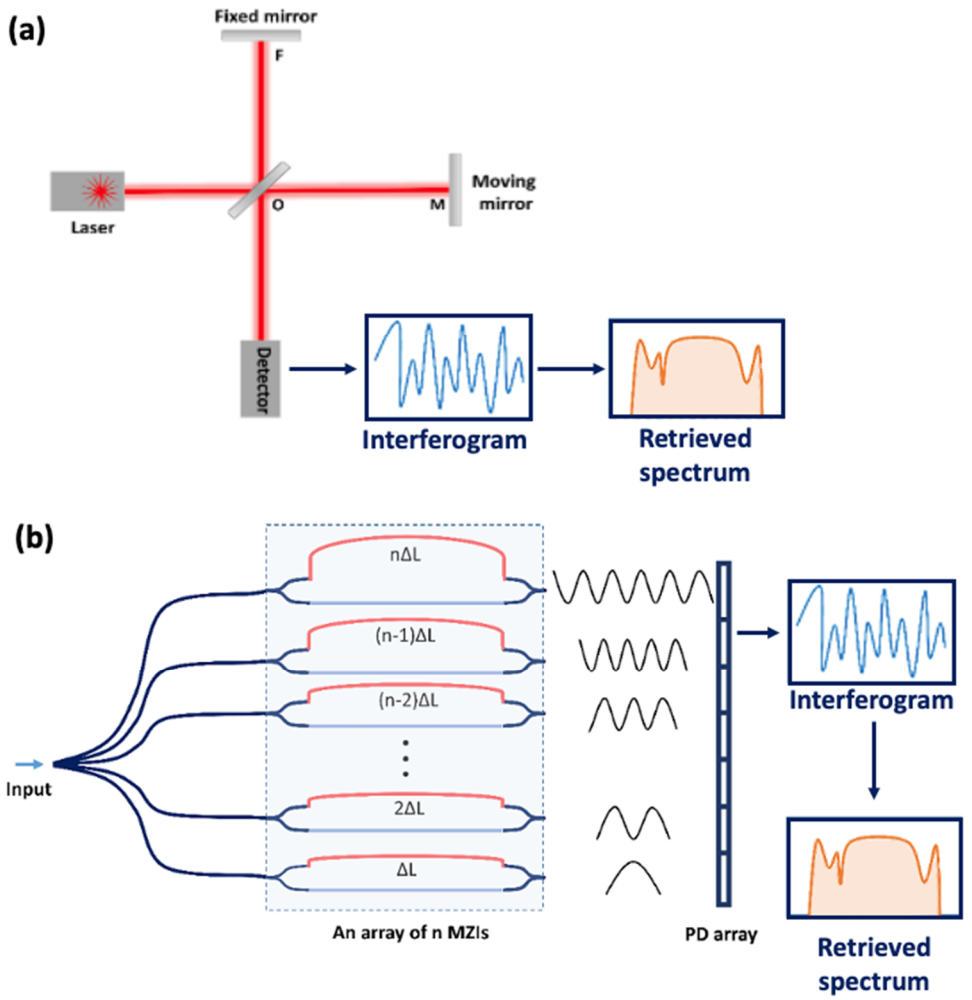


**Figure 4.1**: Schematic view of: a) Fourier transform spectrometer based on free-space Michelson interferometer, b) integrated spatial heterodyne Fourier transform spectrometer. PD: photodetector.

The first integrated SHFTS demonstration was realized in SOI technology in 2007 [176]. The SHFTS comprised multiple inputs, one per MZI (see Fig. 4.2a). MZIs in the array were excited one by one to form the interferogram, achieving a measured resolution of 0.025 nm (~0.13 $cm^{-1}$) a bandwidth of 2.5 nm (~13.4 $cm^{-1}$) for a wavelength near 1365 nm. Later, a passive calibration process was developed that allowed compensating fabrication imperfections during the spectrum retrieval process [166]. This method was applied to a SHFTS comprising 32 MZIs with one single input and a power splitting tree (see Fig. 4.2b), to demonstrate experimentally a resolution of 40 pm (~0.17 $cm^{-1}$) and a bandwidth of 0.75 nm (~3 $cm^{-1}$) for a wavelength of 1550 nm. Since them, a myriad of demonstrations has been reported using different technologies and wavelength ranges. A thorough review can be found in [162]. Some relevant examples include the demonstration of SHFTS in the mid-IR using: i) SOI technology (see Fig. 4.2c), with a resolution and bandwidth of 2.7 nm (2 $cm^{-1}$) and 57 nm (42 $cm^{-1}$),

respectively for a wavelength of 3.75 µm [178], and ii) Ge rich GeSi platform (see Fig. 4.2d), with a resolution of 37.5 nm (15 $cm^{-1}$) and a bandwidth of 132 $cm^{-1}$ for wavelength between 5 µm and 8 µm [182].

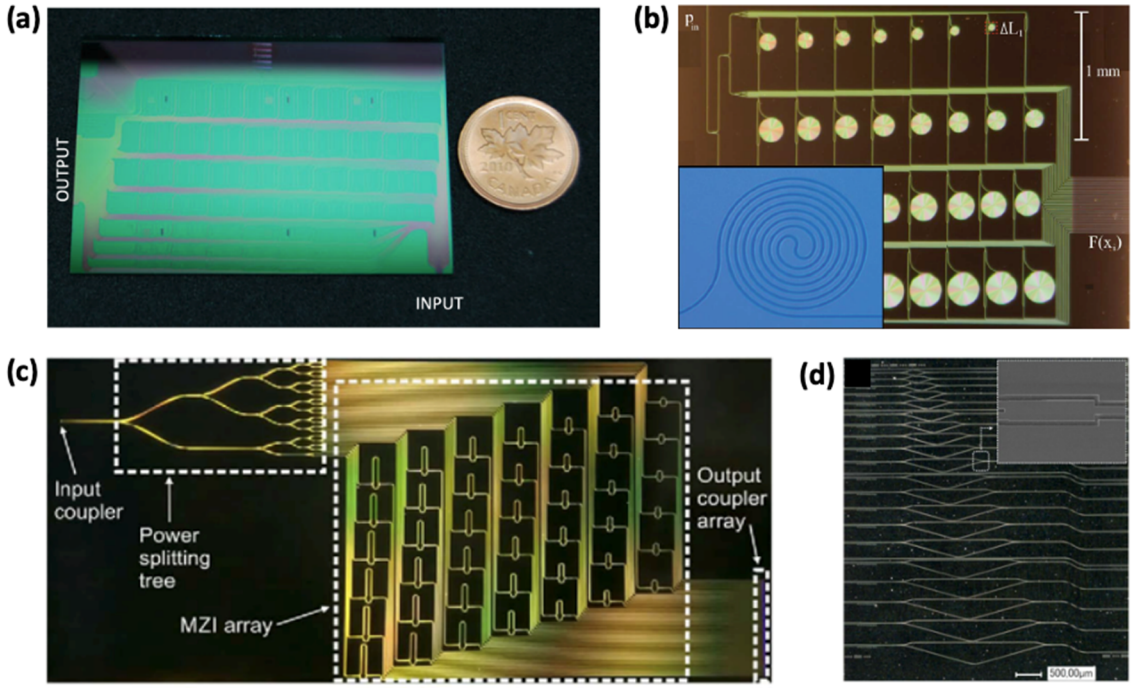


**Figure 4.2**: Spatial heterodyne Fourier transform spectroscopy. **(a)** an image of Fourier transform spectrometer chip, **(b)** Optical image of integrated SHFTS using 32 MZIs with spiral waveguides working at 1550 nm wavelength [166], **(c)** Optical image of SHFTS on SOI platform operating in the mid-IR wavelength [167], **(d)** Optical image of integrated SH-FTS on Ge rich SiGe platform [182].

### 4.1.2 Temporal heterodyne Fourier transform spectrometer

We use here the term temporal heterodyne to refer to FTS that use one interferometer (typically a MZI) to generate a temporally variant interferogram that is used to retrieve the input spectrum, in opposition to spatial heterodyne FTS that use an array of MZIs to generate the interferogram. As discussed in section 4.1.1 Michelson-based FTS dynamically change the physical length of one of the interferometer arms to generate a temporally variant interferogram from which the input spectrum is retrieved. Integrated temporal heterodyne FTS use a MZI (see Fig. 4.3) with a fixed physical path length, as defined by fabrication. The time-dependent interferogram is formed by changing the accumulated optical phase in one of the arms exploiting the thermo-optic [174], [175], [179] or electro-optic effects [183]. As for Michelson-based FTS and SHFTS, the bandwidth and resolution of temporal heterodyne spectrometers follow the Nyquist-Shannon criterion. In the integrated temporal heterodyne case, the resolution is determined by the minimum phase variation that can be induced, while

the resolution is determined by the maximum achievable phase variation. Thermo-optic and electro-optic phase shifters can yield small phase changes, but have a limited maximum accumulated phase change, determined by trade-offs in optical path length (and loss), and power consumption. Hence these devices generally yield remarkably wide bandwidths with limited resolutions.

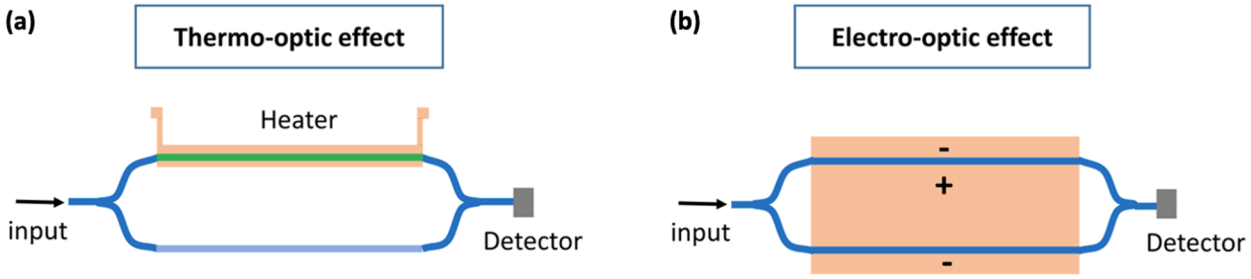


**Figure 4.3**: Schematic of temporal heterodyne FTS using (a) thermo-optic effect and (b) electro-optic effect.

There are several demonstrations of temporal heterodyne FTS using thermo-optic and electro-optic effects. For example, Zheng et al. used the thermo-optic effect in silicon to implement a tunable MZI allowing FTS with a resolution of 9.6 nm (40 $cm^{-1}$) with a broad bandwidth exceeding 150 nm (569 cm-1) for a wavelength near 1550 nm [48]. However, the large temperature variations required to maximize the resolution result in thermal nonlinearities and thermal expansion of waveguides that need to be carefully considered for proper spectrum retrieval [174]. Experimental calibration of thermal nonlinearities and waveguide dispersion was used to demonstrate 3.05 nm (12.7 $cm^{-1}$) resolution with a bandwidth of 56 nm (233.5 $cm^{-1}$) for a wavelength near 1550 nm, using Si MZI and metal heaters (see Figure 4.4a). The use of microfluidic channels as also been proposed to tune the phase in the arms of the MZI [184], providing a calculated resolution of 3.1 nm (12.1 $cm^{-1}$) with 200 nm (755.5 $cm^{-1}$) bandwidth near 1.6 μm wavelength.

The use of a microring resonator-assisted Fourier-transform (RAFT) spectrometer (Fig. 4.4b) has been proposed to increase resolution [175]. This architecture comprises a tunable microring resonator, a temporal heterodyne FTS (MZI tuned by thermo-optic effect), and an integrated photodetector. The ring resonator selects only a narrowband portion of the input signal, before injecting it into the FTS. This way the total resolution is determined by the bandwidth of the ring resonance and not by the FTS itself. This approach was used to demonstrate a large bandwidth of 90 nm (354 $cm^{-1}$) with a high resolution of 0.47 nm (2 $cm^{-1}$) which exceeds the Rayleigh criterion of classical FTS.

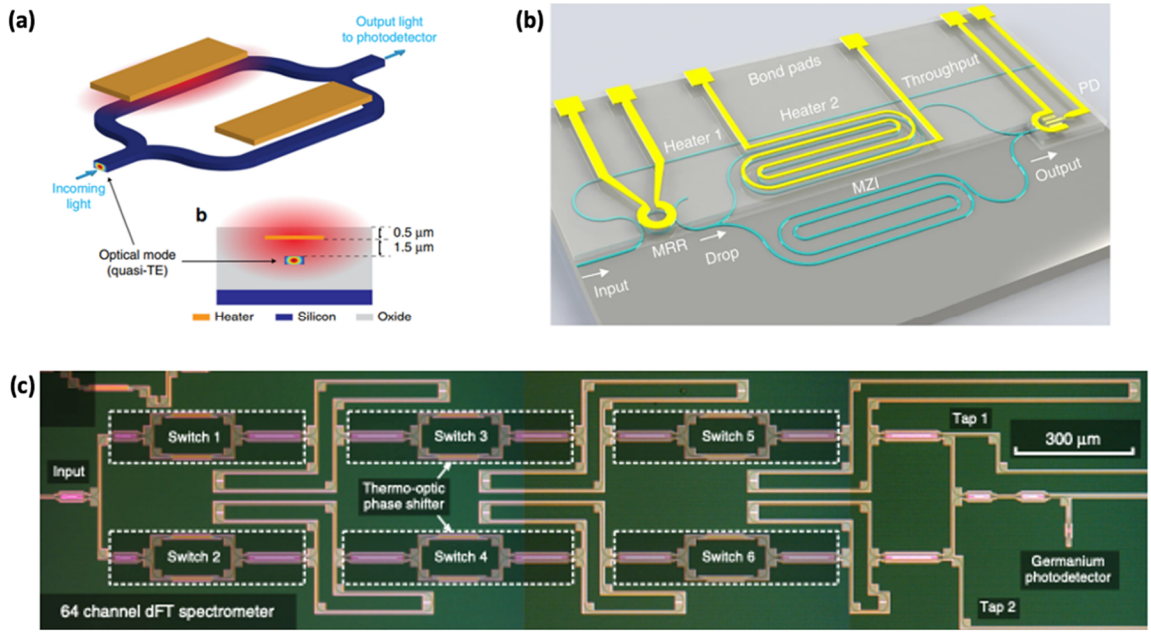


**Figure 4.4**: (a) schematic view of FTS using thermo-optic effects implementing on SOI platform [174]; (b) schematic of the micro-ring resonator assisted Fourier spectrometer consisting of an MRR and an MZI with heaters on top [175]; (c) optical micrograph of the 64-channel digital Fourier Transform spectrometer [185].

An alternative approach utilized one MZI with optical switches that select different optical path lengths (see Fig. 4.4c) [185]. This architecture does not allow the fine tuning of the optical phase of temporal heterodyne FTS, having a limited bandwidth, but allows substantially larger maximum optical length difference, resulting in improved resolution. This approach allowed the experimental demonstration of a resolution of 0.2 nm (0.8 $cm^{-1}$) for a wavelength near 1560 nm.

### 4.1.3 Stationary wave integrated Fourier transform spectrometers

The concept of on-chip stationary-wave integrated Fourier transform spectrometers (SWIFTS) was proposed in 2007 by E. Le Coarer et al. [169], based on the so-called Lippman configuration (see Fig. 4.5a). The light propagating along an integrated waveguide is reflected by a mirror placed at the end of the waveguide to generate a standing wave interferogram. This concept is inspired on color photography of Gabriel Lippmann [186]. The spatial interferogram is recorded using optical near-field detection of the evanescent waveguide field. The input spectrum is retrieved by inverse Fourier transform of the spatial interferogram. In an alternative configuration (Fig. 4.5b), the standing wave is formed through interference of the light injected from the two opposite sides of a waveguide. This configuration is also referred as SWIFTS-counter-propagative. A detector array was placed on the surface of the

waveguide to collect the evanescent field. Again, the input spectrum is retrieved by inverse Fourier transform of the spatial interferogram.

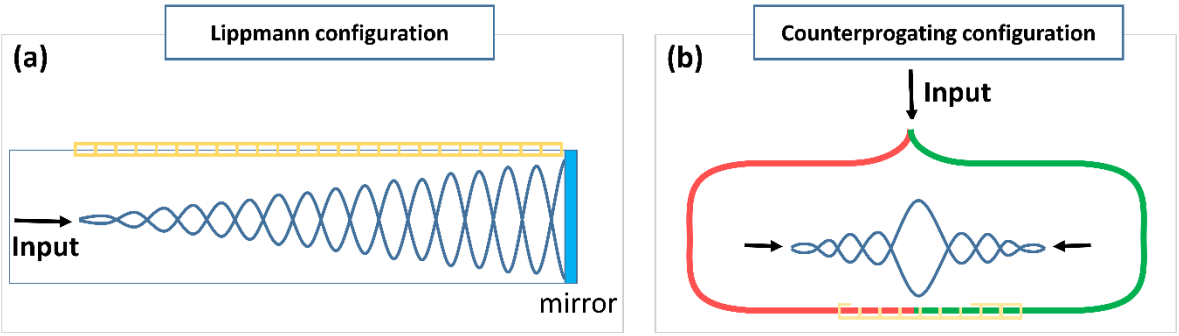


**Figure 4.5**: Schematic view of two different approaches for SWIFTS: (a) Lippmann configuration; (b) counter-propagating configuration.

The counter-propagating approach was demonstrated in 2007, using SOI substrate. The input light was injected to single mode waveguide and coupled into a closed loop using a multimode interference splitter (MMI) (see Fig. 4.6a). The interferogram was characterized using a scattering-type scanning near-field optical microscope (s-SNOM). This SWIFTS device performs a spectral resolution of 4 nm (16.6 $cm^{-1}$) over a spectral wavelength of 96 nm (400 $cm^{-1}$) at a wavelength of 1550 nm. In a follow-up study, SWFTS based on co-propagating waveguide modes was demonstrated on silicon nitride waveguide platform (Fig. 4.6b) [170], achieving a resolution of 6 nm (76 $cm^{-1}$) over a bandwidth of 100 nm (1270 $cm^{-1}$). In this case, the spatial interferogram is recorded using a diffractive grating and an array of photodetectors.

One of the major drawbacks of the SWIFTS is that the spectral bandwidth of the device is limited by the precision in sampling the spatial interferogram (Nyquist-Shannon criterion). S-SNOM technique allows precise sampling of the interferogram but complicates integration. On the other hand, the approach based on photodetector array facilitates integration. However, the resolution is limited by the photodetector size and minimum distance among adjacent detectors. In 2020, the counter-propagating configuration based SWIFTS device using electro-optic effect on Lithium niobate-silicon nitride (LN-SiN) platform was proposed to overcome this obstacle [180]. The electro-optic properties of LN-SiN were exploited to induce a phase shift in the propagating optical mode, resulting in a spatial shifting of the interferogram (positions of maxima and minima) along the waveguide over time (see Figure 4.6c). Consequently, the interferogram can be precisely sampled by spatially shifting the interferogram applying a bias voltage. This LN-SiN SWIFTS achieved an operational bandwidth of 500 nm (2136 $cm^{-1}$) and the spectral resolution of 5.5 nm (23 $cm^{-1}$) at central

wavelength of 1550 nm. Another approach based on parallel waveguides with interleaved sampling points (see Fig. 4.6d) was proposed to enlarge the throughput and improve spectral bandwidth compared with conventional spectrometer [187]. This approach allowed 0.25 µm sampling spacing, yielding a bandwidth of 256 nm (6661 $cm^{-1}$) at 633 nm central wavelength.

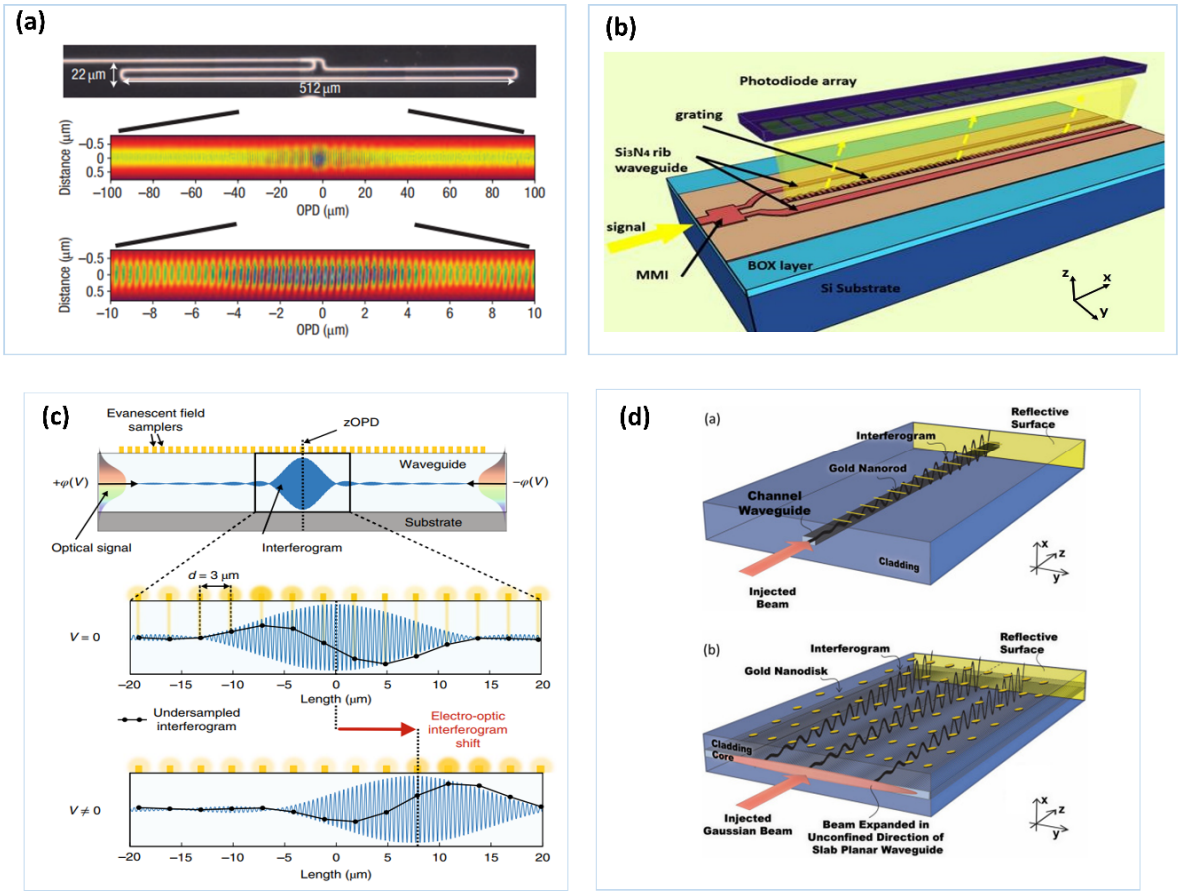


**Figure 4.6**: Standing wave integrated Fourier Transform spectroscopy. (a) Top figure is optical view of SWIFTS counter-propagative fabricated on SOI substrate and below is-SNOM (scattering-type scanning near-field optical microscope) intensity image of the interferogram inside the component [169] (b) Schematic SWFTS based on co-propagating waveguide modes was demonstrated on silicon nitride waveguide platform [170] (c) Top figure is the schematic of SWIFTS using thermo-optic effect on Lithium niobate-silicon nitride and below is the interferogram along the waveguide length overtime of the SWIFT by applying bias voltage[180], (d) illustration of two waveguide spectrometers [187].

## 4.2 Silicon SHFTS exploiting the Jacquinot's advantage

As discussed in the previous section, integrated SHFTS provide some key advantages in terms of resolution and robustness against fabrication imperfections, enabled by passive calibration techniques. In addition, the MZI array configuration is compatible with a multi-aperture configuration that could allow a large optical throughput (étendue), exploiting the so-called Jacquinot's advantage. Still, such key Jacquinot's advantage had not been experimentally demonstrated yet. State-of-the-art SHFTS demonstrations used single-waveguide input and power splitting trees [166], [167], [178] or multiple inputs that are accessed separately, one by one [182], [188].

In this section, we discuss our novel silicon on-chip SHFTS architecture that allowed exploiting the Jacquinot's advantage, by implementing a wide-area collecting input formed by two grating couplers, side by side (see Fig. 4.7a) [15]. One grating is designed for a positive coupling angle $\theta$ and the other for a negative angle $-\theta$. Light illuminating the collecting surface is redirected in the chip plane in opposite directions by respective gratings. This two-way-fed grating geometry was originally proposed to improve the bandwidth of fiber-chip couplers [189]. Here, we used it to increase the light collecting surface and the number of waveguides fed simultaneously. Based on this approach, we fabricate SHFTS using 193-nm deep-UV lithography. The input interface, with a surface of 90 μm × 60 μm, simultaneously feeds 16 MZIs, 8 on each side (see Fig. 4.7b). The output of the MZIs is readout with monolithically integrated germanium photodetectors. The deep-UV fabrication and monolithic integration with Ge photodetectors shown here open new perspectives for large-volume fabrication of on-chip SHFTS. We experimentally show a resolution of 85 pm with a ~13 dB étendue improvement for a wide-area input beam with a radius of 0.5 mm, compared with a conventional surface grating coupler (20 × 20 $\mu m^2$ size).

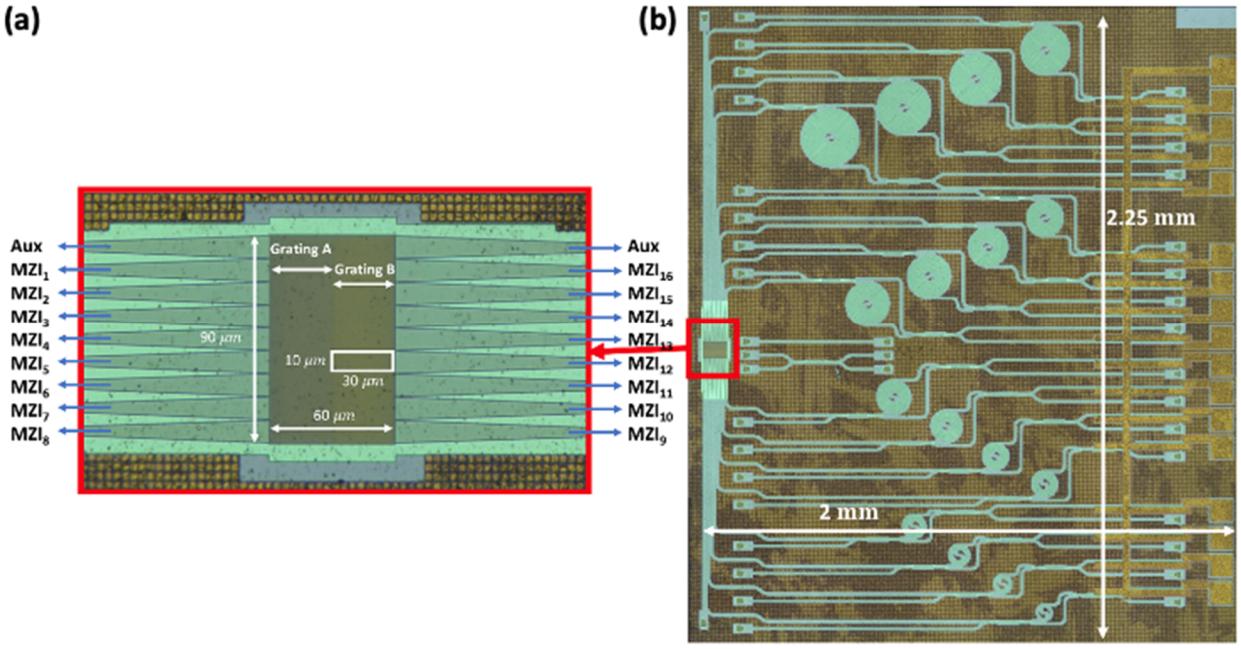


**Figure 4.7**: Optical images of fabricated (a) two-way-fed grating couplers and (b) full SHFTS comprising a wide-area grating coupler, an array of MIZs, and integrated Ge photodetectors.

### 4.2.1 Theoretical study of two-way-fed grating coupler

For the design of the SHFTS, we consider the geometrical parameters provided by the SOI technology at CEA Leti, that is used for fabrication. The main parameters include the silicon layer and the buried oxide (BOX) layer thickness of 300 nm and 720 nm, respectively, two etch steps of 300 nm (full etch) and 150 nm (shallow etch), integrated Ge photodetectors with typical responsivity of 0.6 A/W. We chose a wavelength of 1570 nm, covering the overtone and combination-band transitions of $CO_2$, and CO [190], and transverse-electric (TE) polarization.

First, we consider the design of the proposed two-way-fed grating coupler. Due to the large difference between grating width and thickness, the design of transversal (along $y$ axis) and longitudinal (along $x$ axis) geometries can be treated separately [191]. On the one hand, grating couplers can be made arbitrarily wide. Thus, they can be readily designed to match any desired input beam width. On the other hand, the maximum effective grating length that can be implemented is limited by grating radiation strength. The effective grating length can be increased, weakening the radiation strength by reducing the grating contrast, e.g. using subwavelength index engineering [89]. Nevertheless, the minimum achievable strength may be limited by fabrication constraints like minimum feature size or sensitivity to imperfections.

The proposed two-way-fed architecture connects two grating couplers with opposite radiation angles to double the total length, without the need to halve the grating strength, while

facilitating the excitation of multiple waveguides as light is coupled towards the two sides of the grating.

Figure 4.8 shows the 2D geometry considered for the design of the two-way-fed grating. The large-area coupler is made up of two separate gratings, A and B, which are created to couple light in the $x$ and $-x$ directions, respectively. The grating duty cycle is fixed to $L_A^{Si}/\Lambda_A = L_B^{Si}/\Lambda_B = 0.5$ for both gratings to facilitate fabrication. The periods are set to $\Lambda_A = 550$ nm and $\Lambda_B = 600$ nm, to obtain radiation angles of $\theta_A = -5°$ and $\theta_B = 5°$ for a wavelength of 1570 nm and TE polarization.

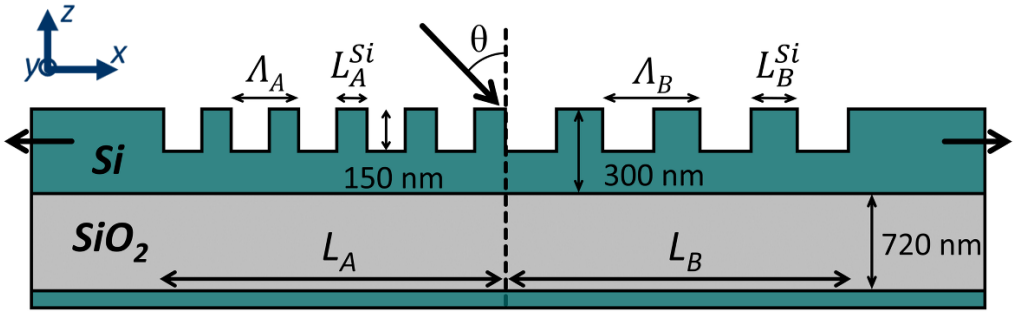


**Figure 4.8**: 2D schematic of the proposed two-way-fed grating coupler comprising of two different gratings A and B which are placed side by side.

To illustrate the improvement of the throughput of the proposed grating, we consider three different scenarios which are shown in Figure 4.9a. We calculate the coupling efficiency as a function of the grating length considering: (i) single grating with $\Lambda_A = \Lambda_B = 550$ nm and coupling light towards the positive $x$ direction; (ii) single grating with $\Lambda_A = \Lambda_B = 600$ nm and coupling light towards the negative $-x$ direction; (iii) two gratings with periods of $\Lambda_A = 550$ nm and $\Lambda_B = 600$ nm coupling both positive $x$ and negative $-x$ directions. In all cases, both grating sections have the same length $L_A = L_B = L/2$. The simulation results for the three different cases are shown in Fig. 4.9b. In the single grating cases, the coupling efficiency increases with increasing grating coupler length, reaching a saturation around 20 μm for $\Lambda_A = \Lambda_B = 550$ nm, and 30 μm for $\Lambda_A = \Lambda_B = 600$ nm. The two-way-fed grating has a significantly longer saturation length of 60 μm, allowing at least a 2.5 dB improvement in coupling efficiency compared with single grating cases. Figure 4.9c presents the simulation results of the angular aperture as the function of the grating coupler length for the three configurations. The proposed wide-area grating allows increasing the effective coupling length with a penalty of only 3° in the angular aperture, compared with conventional gratings.

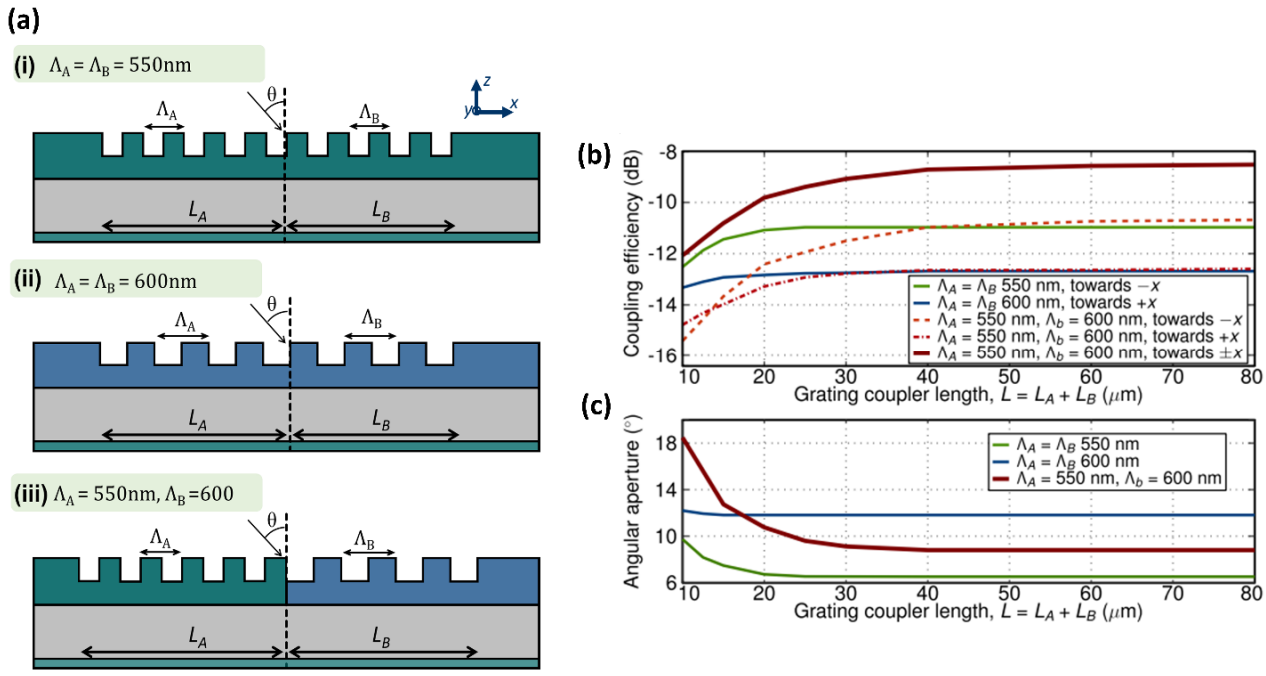


**Figure 4.9**: (a) Schematic illustrating the two-way-fed grating coupler considering three different regimes (i) single grating $\Lambda_A = \Lambda_B = 550$ nm, (ii) single grating $\Lambda_A = \Lambda_B = 600$ nm , (iii) two gratings of $\Lambda_A = 550$ nm and $\Lambda_B = 600$ nm (b) Simulation results of coupling efficiency as a function of the grating coupler length, (c) Angular aperture as a function of grating coupler length.

### 4.2.2 SHFTS fabrication and experimental characterization

The proposed SHFTS comprises 16 MZIs with a maximum path-length imbalance of 7.5 mm, resulting in a theoretical resolution of 75 pm [166]. The SHFTS was fabricated at CEA Leti with 193-nm deep-UV optical lithography. The integrated photodetectors were fabricated using Ge epitaxial growth, boron, phosphorus ion implantation, and standard CMOS metallization steps. Figure 4.7 shows optical images of the complete SHFTS chip.

Interconnection waveguides are 450 nm wide, ensuring single-mode operation. Length imbalance in the MZIs is implemented using spirals with bending radius ranging from 10 µm to 100 µm. The MZIs are implemented with 2×2 multi-mode interference couplers. One input of each MZI is connected to the wide-area two-way-fed grating coupler, and one MZI output is connected to an integrated germanium photodetector, with the responsivity of 0.6 A/W. The other two ports of the MZI are connected to conventional fiber-chip grating couplers, for reference. Conventional fiber-chip grating couplers have a period of 600 nm, a duty cycle of 0.5 and size of $20 \times 20$ µm$^2$. The MZIs in the SHFTS can be excited simultaneously using the two-way-fed grating, or one by one using conventional fiber-chip couplers. The output of each MZI is readout either using integrated photodetectors, or with SMF-28 fibers and analyzed

using external photodetectors. To illuminate the wide-area grating, we use a fiber gradient-index (GRIN) lens collimator with a beam diameter of 0.5 mm, at full-width at half maximum (FWHM).

The two-way-fed collecting input has an area of 90 μm × 60 μm, comprising 18 inputs of 10 μm × 30 μm, each. Access waveguides have a width of 9.8 μm and are separated by 200 nm. Waveguide width is adiabatically reduced to 450 nm with 150 μm-long linear tapers. Eight waveguides on each side are connected to the MZIs in the SHFTS array, while two are connected to auxiliary outputs used for alignment.

To experimentally validate the throughput improvement, we compare the transmittance of the proposed two-way-fed grating coupler with that of a conventional grating with a size of 20 × 20 $\mu m^2$. The conventional grating has a similar area to that of individual inputs in the two-way-fed grating (10 × 30 $\mu m^2$), so they have similar angular apertures. We illuminate the wide-area grating with the GRIN collimator and collect the output of the 16 MZIs, using an SMF-28 fiber and the ports connected to conventional fiber-chip grating couplers. The signal collected at each output port is normalized by the transmittance of two conventional grating couplers in a back-to-back configuration when using the GRIN collimator at the input and SMF-28 fiber at the output. Figure 4.10 shows the transmittance of the 16 MZIs near 1570 nm wavelength. According to simulations, the efficiency from the grating with a negative angle should be about 2 dB higher compared to the grating with a positive angle. The larger experimental difference, of 3-4 dB, can be attributed to fabrication imperfections, misalignment of the input collimator, and larger propagation loss penalty in highly imbalanced MZIs. The total collected power using two-way-fed grating (90 × 60 $\mu m^2$) is 13.3 dB larger than with conventional grating couplers, validating the superior etendue of this configuration.

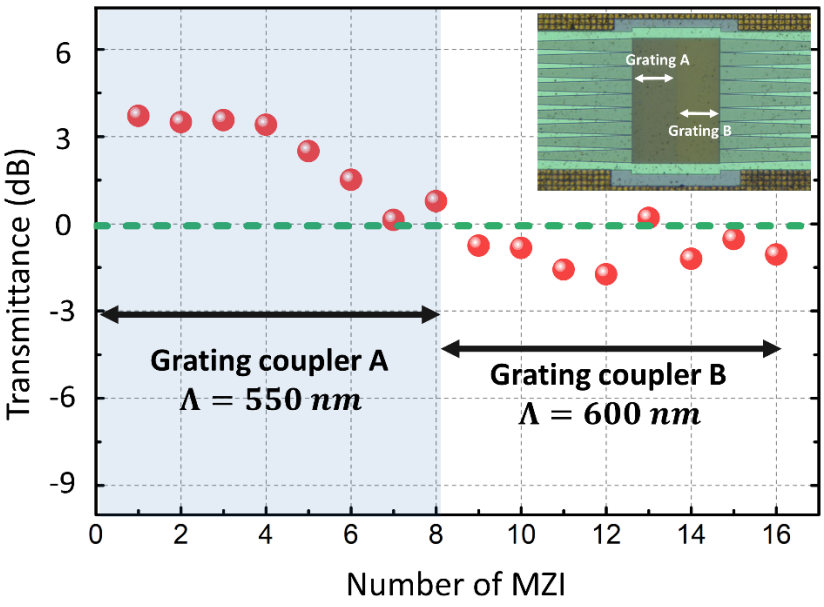


**Figure 4.10**: Transmission of the 16 MZIs near 1570 nm (illuminated with collimators to grating couplers).

Then, we experimentally compare the retrieved spectrum using different input/output configurations in our SHFTS. At the SHFTS input, we can simultaneously excite all MZI using wide-area two-way-fed grating or excite MZIs one-by-one using conventional gratings. The output of the MZIs can be recorded with integrated Ge photodetectors or collected with conventional gratings and recorded using external photodetector.

We perform the spectral retrieval using the passive calibration method proposed in [166]. The outputs of the MZI array form an interferogram $I$. This interferogram can be expressed as $I = B \times T$, where $B$ is the spectrum at the input and $T$ is a transformation matrix containing the measured transmittance data for each MZI. The input spectrum is retrieved by multiplying the interferogram by the pseudoinverse of the transformation matrix $T$. This retrieval method allows passive correction of amplitude and phase errors arising from fabrication imperfections [166].

Figure 4.11a shows the recorded transformation matrix, $T$, when all the MZIs are illuminated simultaneously using a GRIN collimator and the two-way-fed grating coupler. The output is read out with integrated photodetectors. For comparison, Figure 4.11b shows the transformation matrix $T$, recorded using conventional grating couplers at the input and output of the MZIs. There is no significant difference between these two matrices, demonstrating the good performance of the wide-area grating coupler and integrated Ge photodetectors.

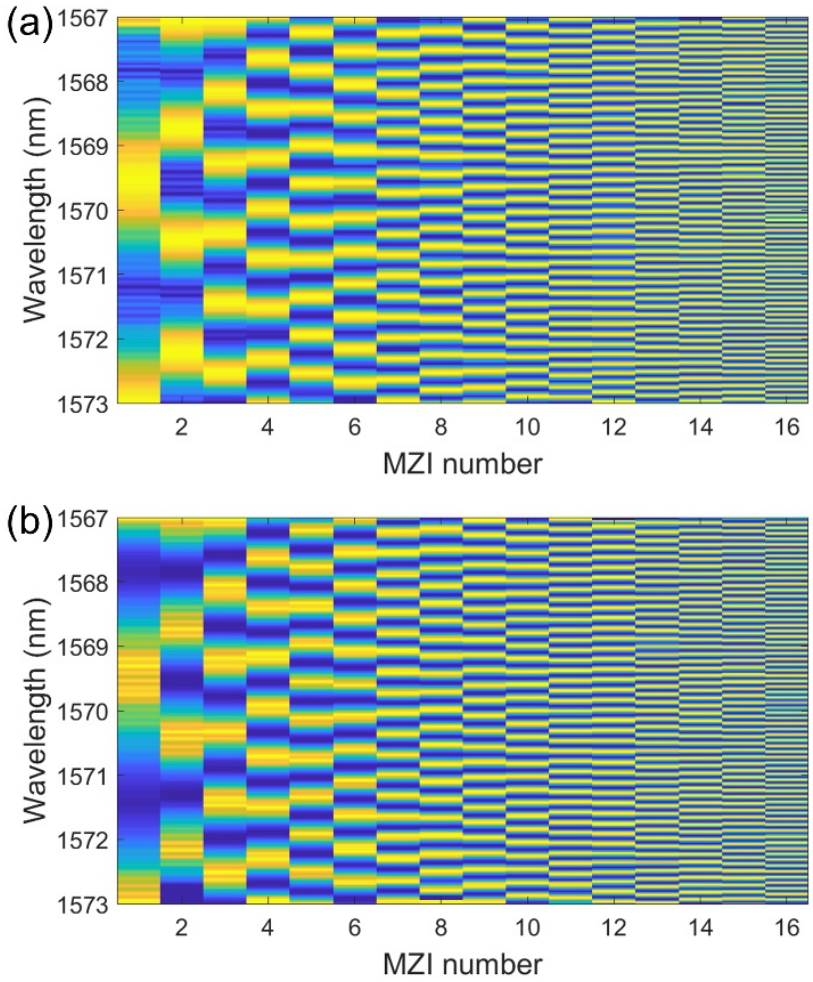


**Figure 4.11**: Transformation matrix of an array of MZIs of Fourier transform spectroscopy with input aperture illuminated using GRIN lens collimator and output readout by integrated Ge photodetectors (a) and illuminated separately convention grating couplers and ouput read out by an external detector (b).

Figure 4.12 shows the measured retrieved input spectrum for four different cases: (i) illumination with a conventional fiber-chip grating SMF-28 fiber, output collected by conventional grating coupler and external photodetector, Fig. 4.12a; (ii) illumination with a wide-area proposed grating coupler and output readout by the conventional grating coupler and integrated Ge photodetectors, Fig. 4.12b; (iii) illumination with the wide-area grating and GRIN collimator, collected with the conventional grating coupler and external photodetector, Fig. 4.12c; (iv) illumination with the wide-area grating coupler and GRIN collimator, read out with integrated Ge photodetectors, Fig. 4.12d. To optimize the signal-to-noise ratio of the retrieved spectrum, we truncate the transformation matrix to 600 pm wavelength range. We also use Gaussian apodization to reduce sideband lobes.

The retrieved spectrum in all cases show similar performance with the spectral resolution of 86 pm, proving the good agreement with the theoretical results. In addition, the retrieved spectra have comparable signal-to-noise ratio with the side lobe below 0.08, demonstrating the calibration can correct imperfections from non-uniform intensity distribution of MZIs.

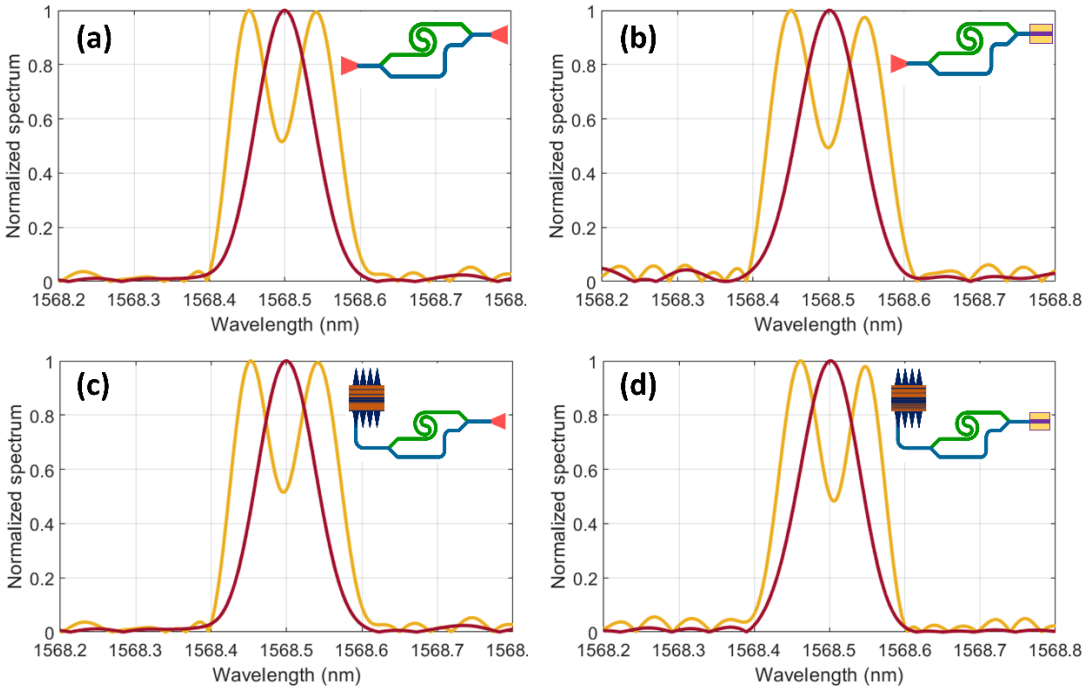


**Figure 4.12**: Retrieved spectra of monochromatic and droplet with peak-to-peak separation of 85 pm at four different configurations; illumination with a conventional fiber-chip grating, output collected by external photodetector (a) or integrated photodetector (b); illumination with a wide-area proposed grating coupler and output readout by the conventional grating coupler (c) or integrated photodetector (d).

Further studies have been carried out to validate the operation of the SHFTS using the two-way-fed grating in wide wavelength range. Figure 4.13 shows the experimentally retrieved spectrum of monochromatic and droplet at four different wavelengths near (a) 1568.5 nm, (b) 1569.2 nm, (c) 1570.8 nm, (d) 1569.8 nm using GRIN collimator and two-way-fed grating coupler as input. There is no significant difference in spectral resolution between the four different spectra.

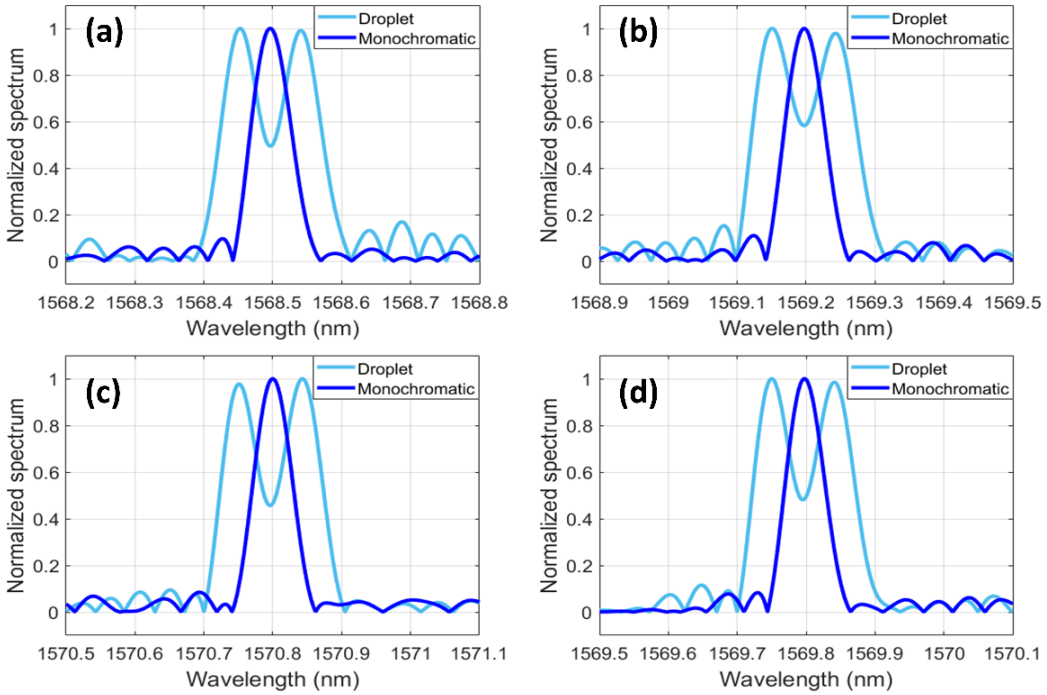


**Figure 4.13**: Retrieved spectrum of monochromatic input and doublet with peak-to-peak separation of 85 nm at different central wavelengths (a) 1568.5 nm, (b) 1569.2 nm, (c) 1570.8 nm, (d) 1569.8 nm.

In conclusion, we experimentally demonstrate a SHFTS fabricated using 193-nm deep-UV optical lithography at CEA leti, comprising a wide-area light collecting aperture of 90 µm × 60 µm and integrated Ge photodetector array. The device relies on a novel two-way-fed grating geometry, combining two grating couplers with opposite radiation angle to simultaneously feed 16 Mach-Zehnder interferometers. We experimentally show a ~13 dB increases in étendue, compared with a conventional input grating coupler aperture, when using a wide-area illumination beam of 0.5 mm FWHM. We compared different device configurations, illuminating all MZI simultaneously with wide-area collection input or one by one with conventional fiber-chip couplers, and recording the MZI outputs with integrated Ge photodetectors and external photodetectors. The large etendue of the proposed configuration and the powerful phase and amplitude corrections provided by the pseudoinverse technique allowed the demonstration of 85 pm resolution using wide-area input aperture and integrated photodetectors, with no significant performance degradation compared to individual illumination of each MZI and readout with external photodetectors. These results open a new route to large-volume production of miniaturized silicon photonic on-chip spectrometers exploiting the Jaquinot's advantage, which can be particularly interesting for sensing

applications in embarked systems where weight, robustness, and étendue are key parameters [192].

## 4.3 Mid-IR SHFTS implemented using suspended Si waveguides with subwavelength cladding

The mid-IR is a particularly interesting wavelength range for spectroscopic applications as it contains the absorption fingerprints of many chemical and biological substances of interest [5], [17]. As discussed in previous sections, integrated SHFTS provide key advantages in terms of optical throughput, resolution and robustness against fabrication imperfections, compared to dispersive devices like arrayed waveguide grating (AWGs) [193] and echelle gratings [164], [194]. Integrated Mid-IR SHFTS have been recently demonstrated using the Ge rich SiGe technology to reach 8.5 µm wavelength with a resolution of 15 $cm^{-1}$ [182]. However, SHFTS demonstrations using SOI technology were limited to 3.75 µm wavelength (2 $cm^{-1}$ resolution) [178]. The main reason for this is the strong absorption of the silica cladding for wavelengths above 4 µm [5]. This limitation has been partially overcome by using the silicon-on-sapphire technology to reach 5 µm wavelength (transparency limit of sapphire). Yet, the only demonstration of an SHFT spectrometer in the silicon-on-sapphire technology operated near 3.3 µm wavelength, with a resolution of 10 $cm^{-1}$ [195]. Suspended silicon membrane waveguides have been identified as a promising solution to exploit the full transparency of silicon (1.1-8 µm wavelength range), as they enable the selective removal of the buried oxide layer under the waveguide core, while taking advantage of the mature SOI technology [34]–[36], [41], [44], [65], [71]. However, this approach has not been yet exploited for the implementation of mid-IR SHFTS in silicon.

In this section, we discuss how we exploited suspended silicon waveguides with subwavelength-grating metamaterials cladding to implement a mid-IR SHFTS [16]. We used the suspended swg-cladded Si waveguides described in Chapter 2 to demonstrate an SHFTS comprising 19 MZIs with a measured resolution of 13 $cm^{-1}$ and a free-spectral range of 120 $cm^{-1}$ near 5.5 µm wavelength. This is, to the best of our knowledge, the largest wavelength for an integrated SHFTS implemented with silicon.

### 4.3.1 Design of mid-IR SHFTS with suspended Si waveguides with subwavelength cladding

The SHFTS is implemented in the SOI technology with 700 nm Si thickness and 3 µm BOX thickness. The swg-cladded waveguides (depicted in Fig. 4.14) have a period of P = 350 nm. We set a gap length of $L_{gap}$= 200 nm to allow penetration of hydrofluoric (HF) acid vapor for substrate removal. The waveguide width of 2.5 µm and the cladding width of 5 µm minimize losses due to optical leakage to the lateral silicon slabs in the 5-6 µm wavelength range.

The SHFTS comprises 20 different MZIs with optical path length gradually increasing from 20 µm to 200 µm. The spectral resolution and the bandwidth of the spectrometer are determined by the equation (4.1) and (4.2) with $\Delta L_{max}$ = 200 µm is the maximum imbalance length, $n_g$ = 3.8 is group index of SWG waveguide calculated from 3D-FDTD, N is the number of MZI and N = 20. The theoretical resolution is approximately 40 nm (~ 13 $cm^{-1}$) at 5.5 µm wavelength, and the free spectral range of the spectrometer is 380 nm (~ 100 $cm^{-1}$). The MZIs are implemented using 1×2 Y-junctions/splitters. Light is injected/extracted to the chip from the facets using 20-µm-wide waveguides.

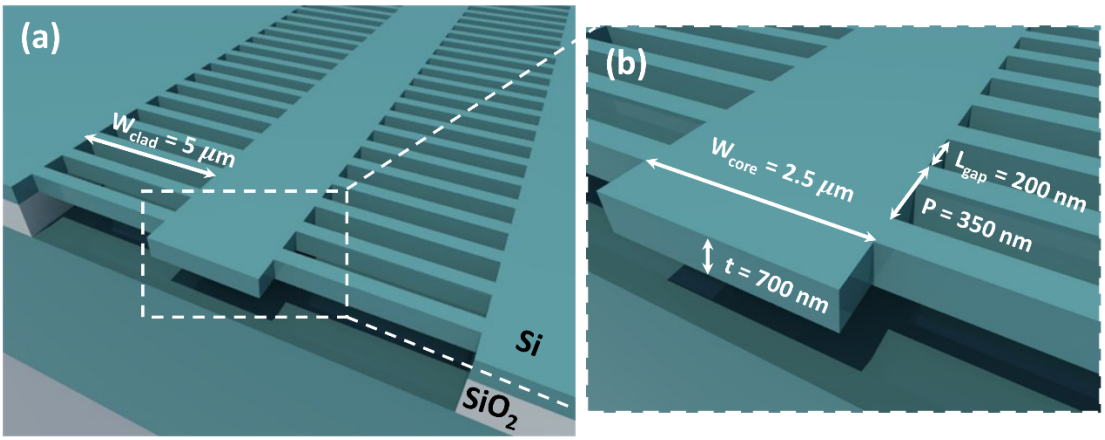


**Figure 4.14**: Schematic view of (a) the suspended silicon subwavelength waveguide, and (b) zoomed top view sowing detail of geometrical dimensions of the proposed waveguides.

### 4.3.2 Fabrication and experimental characterization

The SHFTS is patterned by electron beam lithography, followed by etching step to define the designed structure. The BOX layer is removed locally using the hydro fluoride acid vapor method [196]. Figure 4.15a shows the fabricated device. The whole SHFTS is implemented on a single chip with an area of 18 mm × 7 mm. SEM images of the waveguide, the MZI and the Y-junctions are shown in Figs. 4.15b, 4.15c and 4.15d, respectively. The first MZI, with path-length imbalance of 10 nm was defective. So, the SHFTS was characterized using 19 MZIs.

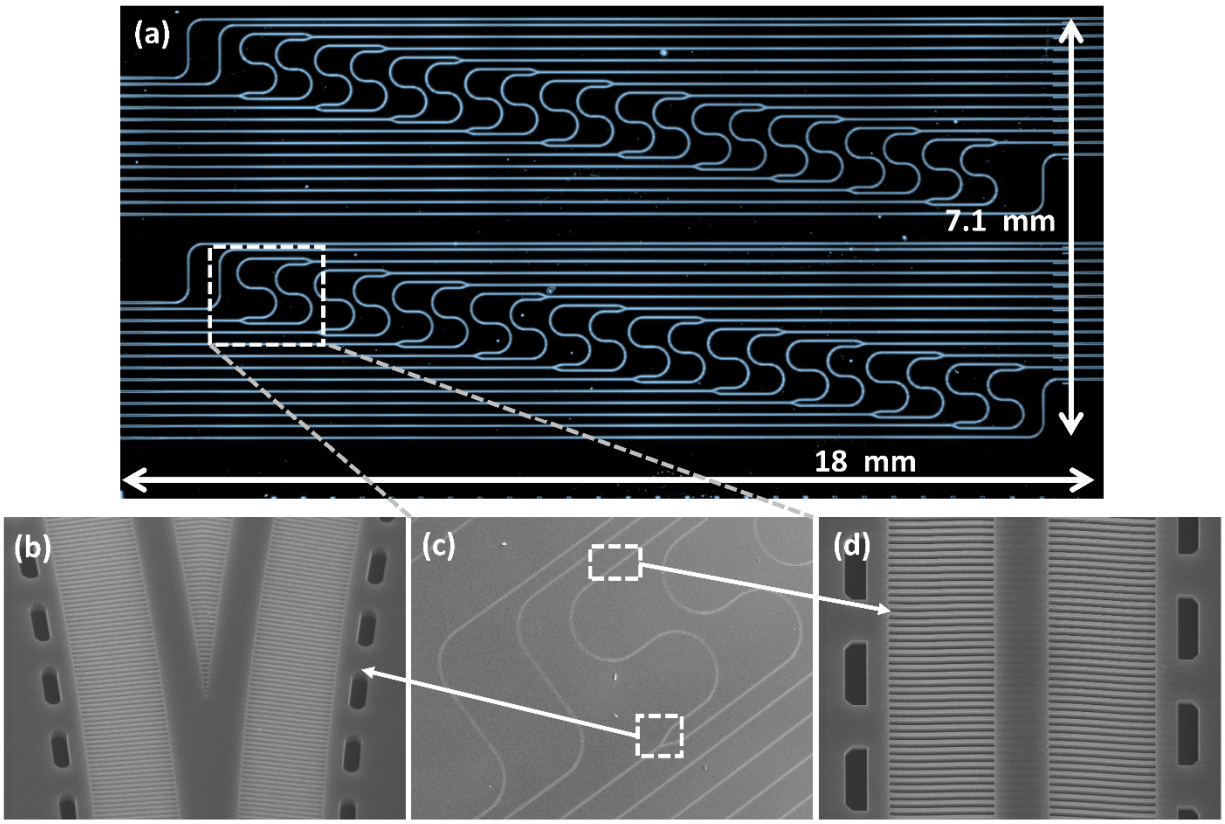


**Figure 4.15**: a) Optical image of fabricated SHFTS operating at mid-IR wavelength comprising of 20 MZI. SEM images of (b) Y junction splitter, (c) Mach-Zehnder interferometer, and (d) suspended subwavelength-grating waveguide.

To experimentally characterize the SHFTS, we used the mid-IR set up presented in Fig. 4.16. The light from external cavity-based quantum cascade laser is butt-coupled into the chip with an aspheric ZnSe lens. Each MZI is characterized separately. The output of the MZI is collected with an aspheric ZnSe lens and recorded with an external MCT (Mercury Cadmium Telluride) photodetector (DSS-MCT (14)020, Horiba). The propagation losses of the suspended subwavelength waveguide are measured below 2 dB/cm at 5.5 μm wavelength (see chapter 2). The measured loss of the Y junction/splitter is less than 1 dB.

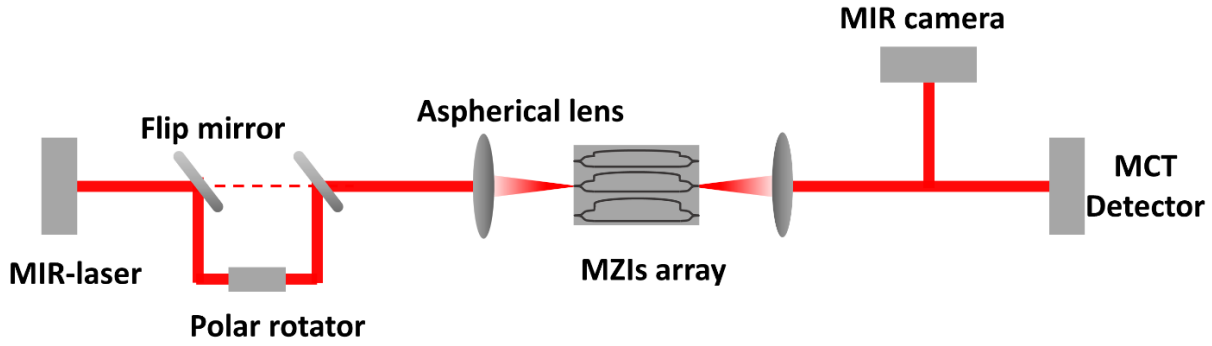


**Figure 4.16**: Schematic of the experimental setup in MIR wavelength.

The input spectrum is retrieved from the output interferogram using the passive calibration matrix, described in section 4.2.2. The measured transformation matrix, $T$, comprising the spectra of the 19 MZIs is presented in Fig. 4.17a. The transformation matrix is formed by measuring the transmittance of each MZI using a tunable quantum cascade laser with a resolution of 1 $cm^{-1}$. For input spectrum retrieval we use a bandwidth of 100 $cm^{-1}$, corresponding to the theoretical FSR. The retrieved spectra for monochromatic input, and a doublet input with a peak-to-peak separation of 40 nm are experimentally reconstructed at different central wavelengths of 5440 nm (Fig. 4.17b), 5520 nm (Fig. 4.17c), 5500 nm (Fig. 4.17d), and 5600 nm (Fig. 4.17e). The spectral resolution is 13 $cm^{-1}$ in the three cases. The linewidth of the tunable quantum cascade laser is 1 $cm^{-1}$, while the linewidth of the retrieved signals is 13 $cm^{-1}$, illustrating the resolution limit of our SHFT.

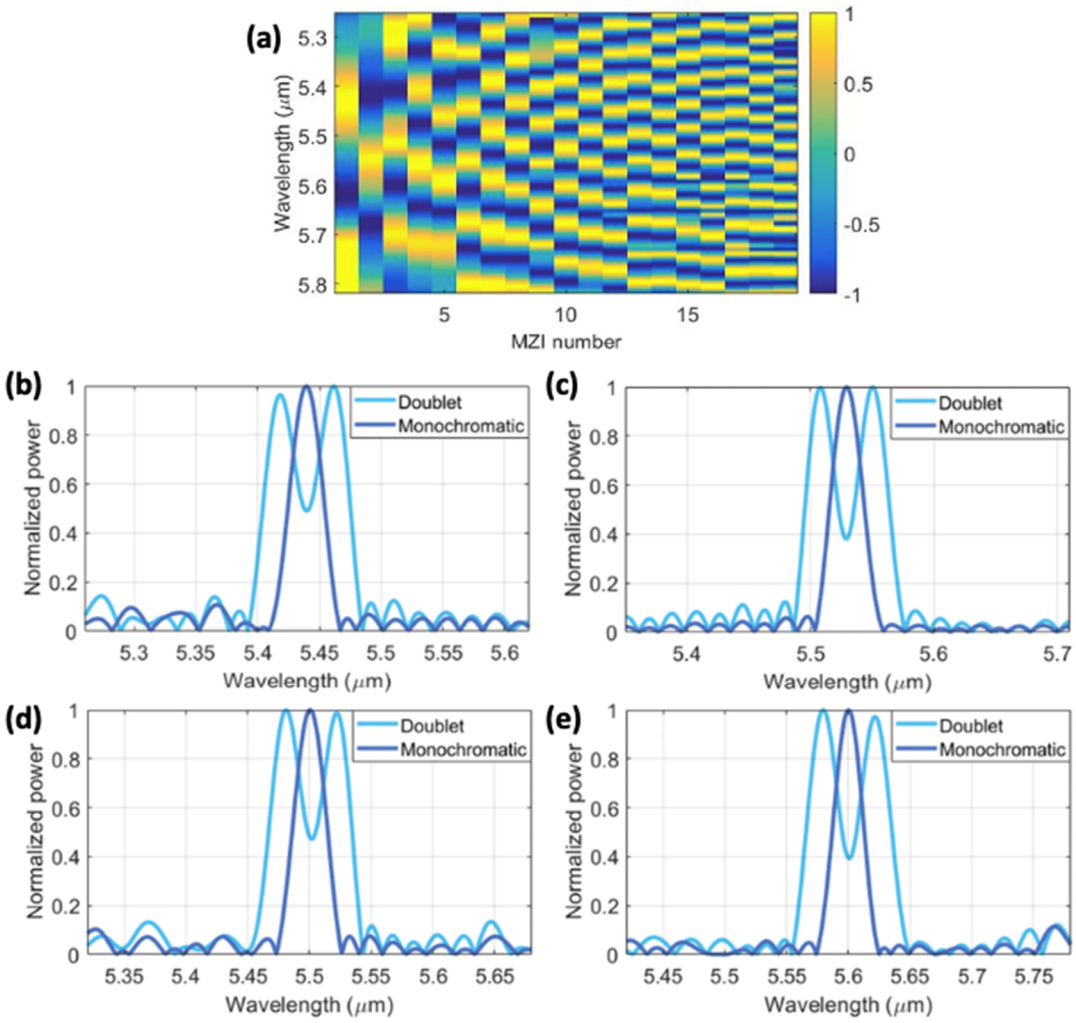


**Figure 4.17**: (a) Calibration matrix of SHFTS on subwavelength silicon. Retrieved spectrum of SHFTS based suspended SWG operating TE polarization at different wavelengths (a) 5440 nm, (b) 5520 nm, (c) 5500 nm, and (d) 5600 nm.

In conclusion, we demonstrated an integrated mid-IR SHFT spectrometer realized using suspended silicon waveguides with metamaterial-grating cladding. This strategy circumvents the absorption constrain of silica cladding for wavelengths above 4 µm, overcoming the major limitation of the SOI technology in the mid-IR. The SHFT spectrometer comprises an array of 19 MZIs with a maximum imbalance length of 200 µm, achieving a measured resolution of 13 $cm^{-1}$ and a bandwidth of 100 $cm^{-1}$, near 5.5 µm wavelength. This is to the best of our knowledge the longest wavelength reported for an integrated silicon SHFT spectrometer. These results open a promising route for the implementation of integrated spectrometers harnessing of the large throughput and robustness against fabrication imperfections of the SHFT architecture, exploiting the full silicon transparency range (1.1-8 µm wavelength) while taking advantage of the mature SOI technology.

## 4.4 Conclusion

Silicon photonics have a great potential for addressing the integration challenges of compact and low-cost integrated spectrometers, and particularly of SHFTS, due to its unique high-index contrast and mass-fabrication advantages. Here, we have demonstrated two strategies that overcome two key limitations of Si SHFTS: i) no experimental demonstration of Jacquinot's advantage, ii) limited operation in the mid-IR for wavelengths above 4 μm.

We have experimental demonstrated the Jacquinot's advantage in an integrated Si SHFTS, fabricated employing 193 nm deep-UV optical lithography with an integrated Ge photodetector array. The device uses a new approach based on two-way-fed grating to implement a wide-area light collecting aperture of 90 μm × 60 μm that feeds 16 integrated MZIs simultaneously. Using a wide-area illumination beam of 0.5 mm FWHM, we show a measured 13 dB increase in étendue when compared to a conventional grating coupler. In addition, examined several device configurations by illuminating all MZIs at the same time with a wide-area collecting input or one at a time using traditional fiber-chip couplers and collecting the MZI outputs with integrated Ge photodetectors and external photodetectors. Compared to the individual illuminating in MIZ using conventional fiber-chip grating, the SHFTS using two-way-fed grating coupler allows a significant etendue increase without any measurable penalty in terms of resolution or bandwidth.

We also demonstrated the first time a SHFTS implemented with suspended silicon SWG platform working at mid-IR wavelengths. This SHFTS allowed, reaching mid-IR wavelengths in the 5-6 μm range with a silicon technology. The SHFTS is comprises 19 MZIs with a maximum imbalance length of 200 μm, achieving a measured resolution of 40 nm (~13 $cm^{-1}$) and a bandwidth of 380 nm (~100 $cm^{-1}$). The resolution and bandwidth can be readily improved in the future by increasing the optical path length difference and the number of integrated MZI. This work is the first demonstration of integrated SHFTS on suspended subwavelength grating working at mid-IR wavelength.

# Chapter 5: Supercontinuum generation in the Near-IR and Mid-IR using suspended silicon waveguides with subwavelength cladding

This chapter provides brief overview of supercontinuum generation in silicon waveguide. In the first section, we will recall the fundamental background of supercontinuum generation in nanostructured waveguide and recent achievements in silicon photonics. In the second section we detail how we exploit the unique degree of freedoms released by subwavelength waveguides to engineer the waveguide dispersion and control the position of the dispersive waves, experimentally demonstrating supercontinuum generation 2.35 octaves, between two dispersive waves near 1.55 μm and 7.5 μm wavelength [13]. This is, to the best of our knowledge, the widest supercontinuum generation in silicon and one of the widest demonstrations using integrated waveguides. Conclusions are drawn in the last section of the chapter.

## 5.1 Introduction

### 5.1.1 Principle of supercontinuum generation

Supercontinuum generation (SCG) is a complex process that results from the propagation of high-power short pulses along a dispersive nonlinear medium, e.g. a silicon waveguide. It should be mentioned that SCG can also be obtained by pumping in normal dispersion regime. However, in this section, particular emphasis is placed on the scenario of SCG pumped by femtosecond pulses in the anomalous group velocity dispersion regime of the waveguide. SCG is based on the propagation of solitons, which result from the interplay between group velocity dispersion (GVD) and self-phase modulation (SPM). GVD is a linear property of the waveguides, while SPM is a nonlinear property that in silicon is associated to third-order nonlinear Kerr effect.

**Group velocity dispersion**

When a pulse propagates along a waveguide, it is affected by the dispersion, i.e. different wavelength components propagate at different velocities due to the wavelength dependence of the refractive index, affecting both the phase and group velocity of the pulse. In an optical

waveguide, the total dispersion depends on material chromatic dispersion and the geometry. The frequency dependence of the propagation constant $\beta(\omega)$, can be described using a Taylor series expansion around the center frequency $\omega_o$:

$$\beta(\omega) = \sum_{k=0}^{\infty} \frac{\beta_k}{k!}(\omega - \omega_0)^k \tag{5.1}$$

$$\beta_k = \frac{\partial^k \beta}{\partial \omega^k} \tag{5.2}$$

Where $\beta_k$ are the higher order dispersion coefficients, $\beta_0$ is the wave number at the center frequency $\omega_0$, $\beta_1 = 1/v_g$ where $v_g$ is the group velocity, and $\beta_2$ corresponds to the GVD. Note that both $\beta_2$ and D are used to describe the GVD in the literature. D can be calculated from $\beta_2$ (unit of $s^2m^{-1}$) using the relation $D = -(2\pi c/\lambda^2)\beta_2$ (unit of ps/nm/km).

The GVD can be divided into different regimes:

- Normal dispersion ($D < 0$, $\beta_2 > 0$): longer wavelength (shorter frequency) travel faster than shorter wavelength (longer frequency).
- Anomalous dispersion ($D > 0$, $\beta_2 < 0$): longer wavelength (shorter frequency) travel slower than shorter wavelength.

Figure 5.1 shows schematically the dispersion-induced chirp of a pulse when propagating through a dispersive medium. Normal dispersion results in positively chirped pulse, while anomalous dispersion results in a negatively chirped pulse.

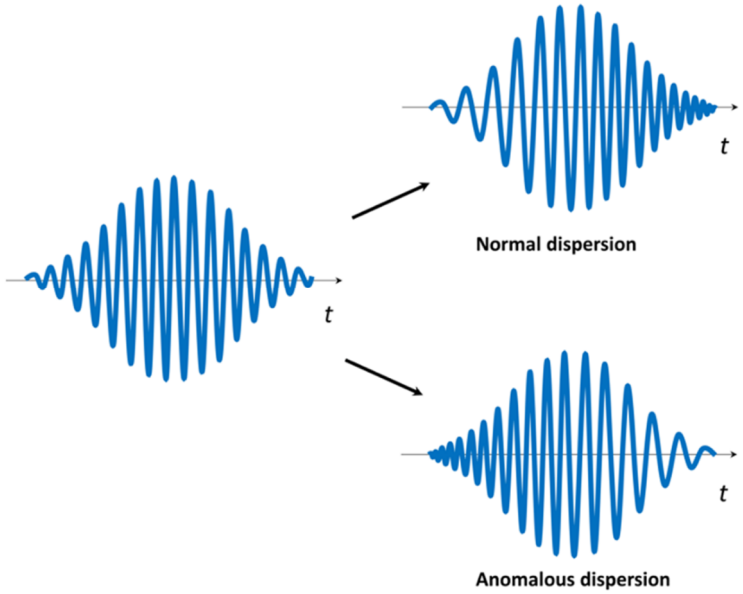


**Figure 5.1**: Schematic of chirping of an optical pulse when propagating trough, a medium with: normal dispersion (D < 0, $\beta > 0$), resulting in positively chirped pulse, or anomalous dispersion (D > 0, $\beta < 0$), resulting in negatively chirped pulse.

### Self-phase modulation

When a high-intensity pulse propagates along a waveguide, the refractive index of the material changes with the intensity through the third-order nonlinear Kerr as [197]:

$$n = n_0 + n_2 I \tag{5.3}$$

Where $n$ is the complex refractive index, $n_0$ is the real refractive index, $I$ is the intensity of the electric field, $n_2$ is the nonlinear Kerr coefficient. In the case of a pulse, this intensity-dependent refractive index variation results in the SPM phenomena. Since most materials have a positive $n_2$, the SPM generally results in a positively chirped pulse (see Figure 5.2).

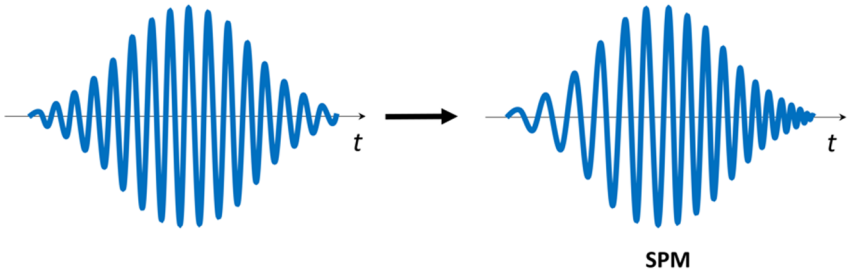


**Figure 5.2**: SPM chirping of an optical pulse for positive $n_2$ (most of materials).

### Optical soliton

The optical soliton is a common term used to describe the phenomenon in which the optical pulse shape is preserved during transmission as the consequence of the balance between the SPM and GVD in the medium. As can be seen in Fig. 5.3, anomalous GVD and SPM with positive $n_2$ result in opposite pulse chirping. Perfect compensation of GVD and SPM result in propagation with no variation of the pulse shape, also referred as fist-order soliton. Periodic compensation of GVD and SPM result in propagation of higher order solitons.

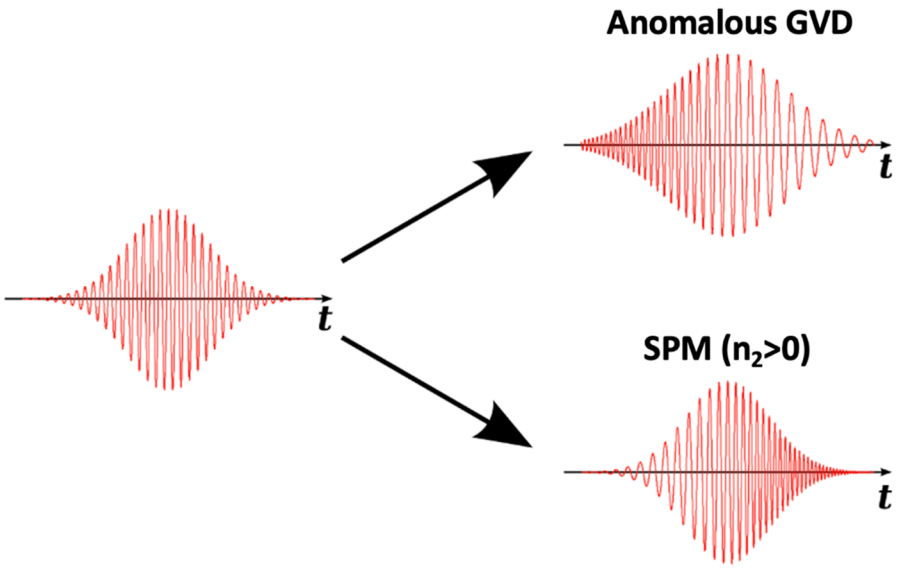


**Figure 5.3**: Comparison of pulse chirping produced by anomalous GVD and SPM with positive $n_2$.

The interplay between GVD and SPM is generally analyzed using the characteristic linear dispersion length ($L_d$) and nonlinear length ($L_{nl}$), defined as:

$$L_d = \frac{T_0^2}{|\beta_2|} \tag{5.4}$$

$$L_{nl} = \frac{1}{\gamma P_0} \tag{5.5}$$

where $\gamma$ is the nonlinear coefficient, $P_0$ is the input peak power, and $T_0$ is the initial pulse duration. The nonlinear coefficient $\gamma$ is calculated from the nonlinear index and the effective area $A_{eff}$ as:

$$\gamma = \frac{\omega_0 n_2(\omega)}{c A_{eff}(\omega_0)} \tag{5.6}$$

$$A_{eff} = \frac{\left(\iint_{\infty} |F(x,y)|^2 \, dx \, dy\right)^2}{\iint_{\omega g} |F(x,y)|^4 \, dx \, dy} \tag{5.7}$$

These characteristic lengths do not correspond to any particular value, but they allow comparing the contributions of GVD and SPM on pulse propagation. If $L_d \ll L_{nl}$, nonlinear effects are negligible compared to dispersion effects. Conversely, if $L_d \gg L_{nl}$ dispersion effects are negligible compared to nonlinear effects. In the case where $L_d$ and $L_{nl}$ are within the same order of magnitude, interplay between GVD and SPM play a key role in pulse propagation. When $L_d = L_{nl}$, GVD and SPM compensate perfectly, creating a first order soliton (see Fig. 5.4a). On the other hand, higher-order solitons can exist under the following condition:

$$N^2 = \frac{L_D}{L_{NL}} = \frac{T_0^2 \gamma P_0}{|\beta_2|} \tag{5.8}$$

With N, the soliton order, an integer number.

Higher order solitons exhibit periodic spectral and temporal change across a soliton period (see Fig. 5.4b). However, the soliton is unstable and can be easily affected by the perturbations. The term "soliton fission" is used to describe the phenomena when a higher order soliton is perturbed and splits into a sequence of N smaller amplitude pulses. Soliton fission plays an important role in the initial spectrum broadening of SCG. Figure 5.4c shows an example of the soliton fission and supercontinuum generation in temporal and spectral domains. It can be clearly observed that each generated soliton has a distinct central frequency and travels with different group velocity.

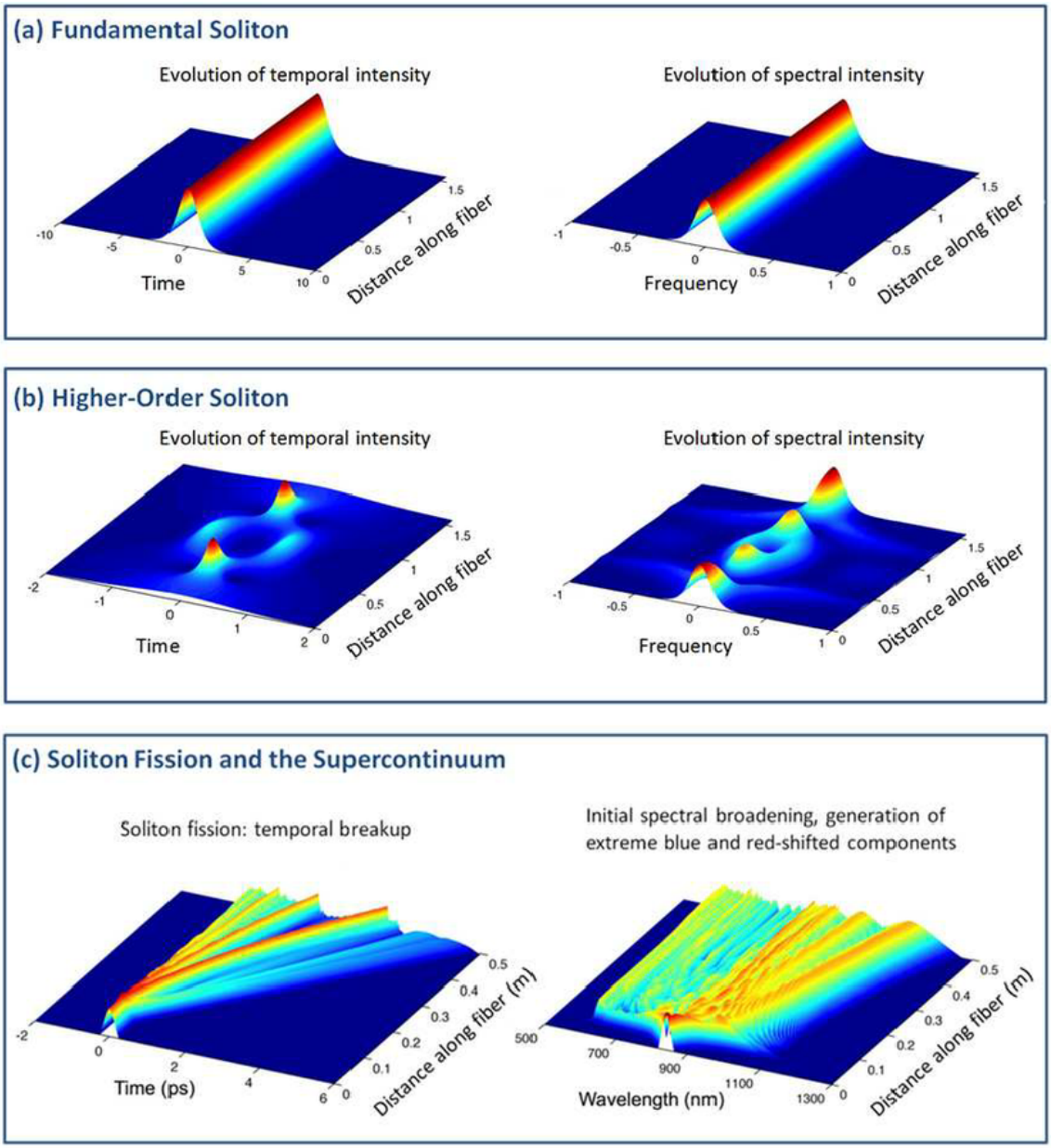


**Figure 5.4**: Comparison of temporal and spectral evolution between a) fundamental soliton, b) higher order soliton, c) soliton fission and supercontinuum generation [198].

### Dispersive waves

When a soliton propagates close to the zero-dispersion wavelength in the presence of higher-order dispersion, a part of this energy can be transferred from the soliton to the normal GVD regime, resulting in the formation of a low amplitude temporal pedestal known as a "dispersive wave" (“non-solitonic radiation” or “Cherenkov radiation”). By solving a nonlinear phase-matching equation, the frequencies of the dispersive wave can be numerically

calculated. The maximum achievable bandwidth of the SCG on both the long and short wavelength edges of is determined by the position of the dispersive waves.

The position of the dispersive waves can be predicted by solving the phase matching condition:

$$\beta_{int} - \frac{\gamma P}{2} = 0 \tag{5.9}$$

Where P is the peak power if the soliton, $\gamma$ is the nonlinear coefficient which is defined by:

$$\gamma = \frac{\omega_0 n_2(\omega)}{c A_{eff}(\omega_0)} \tag{5.10}$$

Where $\omega_0$ is the center frequency, c is the light constant, and $A_{eff}$ is the effective modal area. The integrated dispersion is defined as:

$$\beta_{int} = \beta(\omega_{DW}) - \beta(\omega_s) - \frac{\omega_{DW} - \omega_s}{v_{g,s}} \tag{5.11}$$

In short, SCG is the result of a complicated interaction between dispersion and SPM. It has a significant connection to soliton dynamics. During soliton fission, significant spectrum widening and the formation of DWs occur. The spectral and temporal evolution can be derived from generalized nonlinear Schrödinger equation (GNLSE) [197].

### 5.1.2 State-of-the-art of supercontinuum generation with integrated waveguides

Recent demonstrations show the great potential of nanophotonic waveguides for on-chip nonlinear optics, as they provide tight mode confinement, with modal areas near 1 μm², that result in a substantial reduction of the power required to trigger nonlinear effects. Several studies of SCG based on integrated waveguides made with different material platforms and different waveguide configurations have been reported which achieved octaves spanning bandwidth in the visible, near-IR and mid-IR. The table below summarizes the key figures of merit of some relevant SCG demonstrations

**Table 5.1**: Summary of SCG on different platforms.

| Platform | Structure | Loss | Pump wavelength | Peak power | Bandwidth (μm) | ref |
|---|---|---|---|---|---|---|
| SOI | Rib | 1.5 dB/cm | 1.9 μm | 320 W | 1.06 – 2.4 μm | [199] |
| SOI | strip | - | 2.5 μm | 125 W | 1.5 – 3.6 μm | [61] |
| $SiN_x$ | - | 0.5 dB/cm (1.3 μm wavelength) | 1.2 μm | 3800 W | 0.4 – 1.6 μm | [200] |

| | | | | | | |
|---|---|---|---|---|---|---|
| $SiN_x$ | - | 0.2 dB/cm (2.09 µm wavelength) | 2.09 µm | 6800 W | 1.3 – 4 µm | [201] |
| SOS | Rib | 5 dB/cm (3.7 µm wavelength) | 3.7 µm | 1820 W | 2 – 6 µm | [39] |
| Chacogenides | Rib | 0.6-1 dB/cm (4 µm wavelength) | 4.2 µm | 4500 W | 2 – 10 µm | [64] |
| Chacogenides | Rib | 0.5 dB/cm (4 µm wavelength) | 4 µm | 3260 W | 1.8 – 7.5 µm | [202] |
| Suspended Si | Rib | 2 dB/cm (3.2 µm wavelength) | 3.06 µm | 1100 W | 2 – 7.7 µm | [71] |
| Ge on Si | Rib | 1.2-1.35 dB/cm | 4.6 µm | 3300 W | 3.5 – 5.8 µm | [62] |
| SiGe graded | Rib | 0.5 dB/cm (8 µm wavelength) | 7.5 µm | 2600 W | 3 – 13 µm | [72] |
| Suspended Si | SWG | < 2 dB/cm (5-7 µm wavelength) | 3.5 µm | 1000 W | 1.55 – 7.5 µm | This PhD [13] |

**SCG in the near-IR**

N. Singh et al. demonstrated the coherent SCG on SOI platform in the near-IR to short-mid-IR range (Fig. 5.5a) [199]. By pumping at 1.9 µm wavelength with input pulse average power of 3.6 mW, repetition rate of 200 MHz, and duration between 50 and 100 fs to the rib waveguide, the generated SC expands from approximately from 1.06 to beyond 2.4 µm wavelength at -20 dB level [199]. In addition, the coherence of the spectrum was experimentally characterized, showing good agreement with the simulations with a degree of mutual coherence above 95% over the whole bandwidth. C. Lafforgue et al. have reported the use of $SiN_x$ (Fig. 5.5b) to yield 2-octave SCG spanning from the visible (400 nm) to the near-IR (1600 nm) [200]. Lately, SCG was studied in more elaborated designs such as tapered structures with waveguide width variation along the propagation length instead. In ref [203], the authors have studied numerically SCG in tapered waveguide and dispersion-managed (DM) silicon waveguide with a longitudinal variation of the waveguide width, used to modify The GVD along the pulse propagation. With the 200 fs and 6.4 pJ input pulse, the tapered structure can theoretically achieve spectral spanning of 1.14 octave from 1300 nm to 2860 nm, and the DM waveguides achieve 1.25 octaves from 1200 to 2870 nm at -20 dB level. Later in 2019, Singh et al. reported varying dispersion designs with tapered and cascaded waveguides (Figure 5.5c) [204]. The results showed that the supercontinuum is flatter and more coherent compared to single dispersion waveguide when longer input pulses are used.

When compared to a fixed dispersion waveguide, they reported a16 dB signal improvement in the telecom window and 100 nm of wavelength extension is achieved with a cascaded waveguide. The supercontinuum signal expanded by pumping concurrently with both quasi-TE and quasi-TM modes in the anomalous dispersion regime due to the substantial birefringence of an asymmetric silicon waveguide.

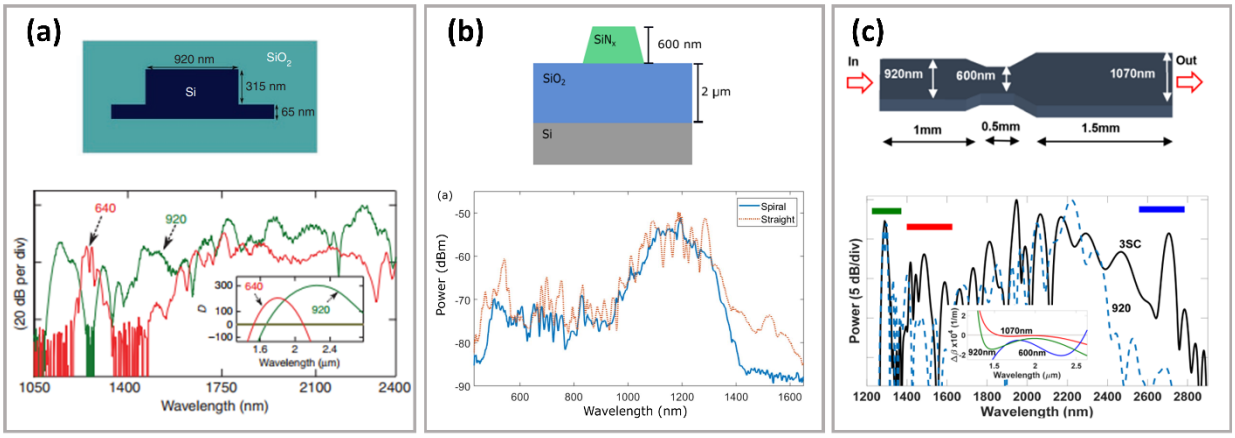


**Figure 5.5**: (a) schematic of the SOI waveguide cross-section (top), and the SC spectrum extends from 1.1 μm to 2.4 μm (bottom) [199]; (b) schematic of the nitrogen-rich silicon waveguide section (top) and SC spectral for an input peak power of 3.8 kW [200]; (c) schematic illustration of the cascaded waveguide with its cross-section (top); and three-section cascade waveguide [204].

### SCG in the mid-IR (not silicon)

SCG based on integrated waveguides has also been studied for the nonlinear light generation in the mid-IR. A remarkably wide mid-IR SCG, from 2 μm to 10 μm wavelength has been demonstrated using chalcogenide waveguides (GeAsSe/GeAsS) (Figure 5.6a) [64]. SCG in an air-clad SiGe-on-Si waveguides (Fig. 5.6b) have been reported with spectral spanning covering from 3 μm to 8.5 μm wavelength [205]. In 2020, M. Monestinos et al. experimentally demonstrated SCG on Ge-rich graded SiGe graded waveguide (Fig. 5.6c) which has the linear increasing concentration of the Ge along the vertical axis up to 80% [72]. This waveguide was injected with a 200 fs pulse at anomalous dispersion regime achieving two-octave SCG from 3 μm to 13 μm which covers almost full Ge transparency window.

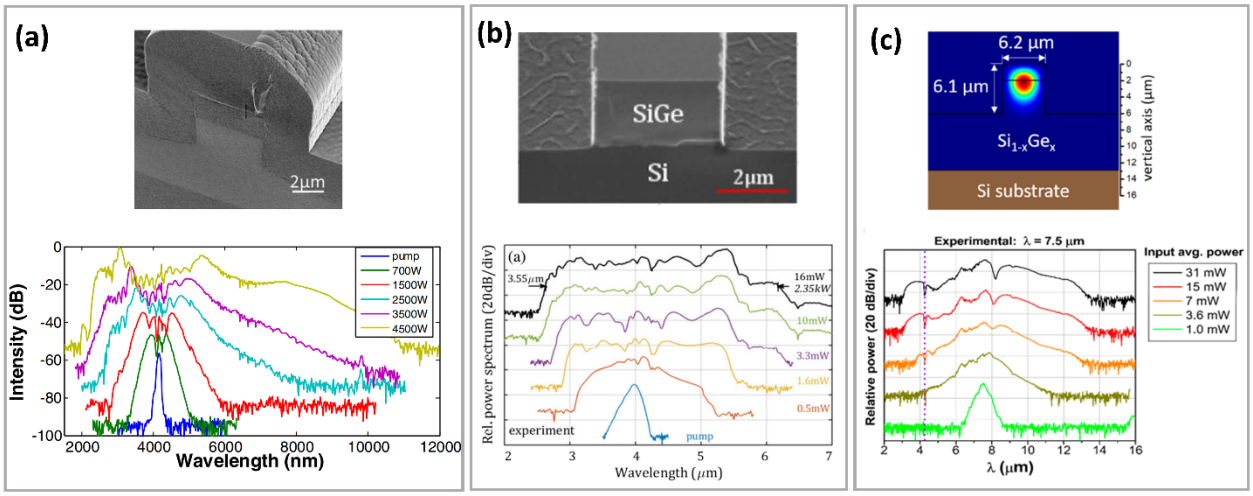


**Figure 5.6**: SCG in the mid-IR (not silicon). (a) SEM image of chalcogenide rib waveguide (top) and experimental SC spectral at pumb wavelength of 4.18 μm with different powers (bottom)[64]; (b) SEM image of SiGe 40%/Si waveguide (top) and measured spectra with increasing coupled power [205]; (c) Schematic of the Ge-rich graded SiGe waveguide (top) and experimental SC spectral at input wavelength of 7.5 μm with different powers (bottom) [72].

### SCG in the mid-IR with silicon

Silicon presents outstanding nonlinear properties for SCG in the mid-IR, including a strong nonlinear Kerr coefficient, 2 orders of magnitude higher than silica [58], [206], and negligible two-photon absorption for wavelengths above 2 μm. In addition, the high index contrast between the silicon (air n~3.48) and the cladding (air n = 1) enables tight optical confinement reducing the effective modal area and allowing advanced dispersion engineering. However, the absorption of silica in the conventional SOI platform limits expanding the spectral broadening in the longer wavelength beyond 3.5 μm [5].

One octave of SCG has been demonstrated on SOI waveguide, achieving the broadband spectrum covering up to 3.6 μm (shown in Fig. 5.7a), near the absorption limit of the silica cladding [61]. In 2015, silicon-on-sapphire (SOS) nanowires were used for SCG in the mid-IR range [39], taking advantage of the wider transparency of the sapphire substrate, up to 5 μm wavelength, compared to that of silica, up to 3.5 μm wavelength. By using a 320 fs pulses source centered at 3.7 μm wavelength and peak power of 2.5 kW, they obtained SCG spanning from 2-6 μm wavelength range in SOS nanowires (shown in Fig. 5.7b). Suspended silicon rib waveguides fabricated via wafer bonding have been used to achieve a wide spectrum from 2 to 7.7 μm by pumping wavelength at 3.06 μm with the peak power of 1.1kW (shown in Fig. 5.7c) [71].

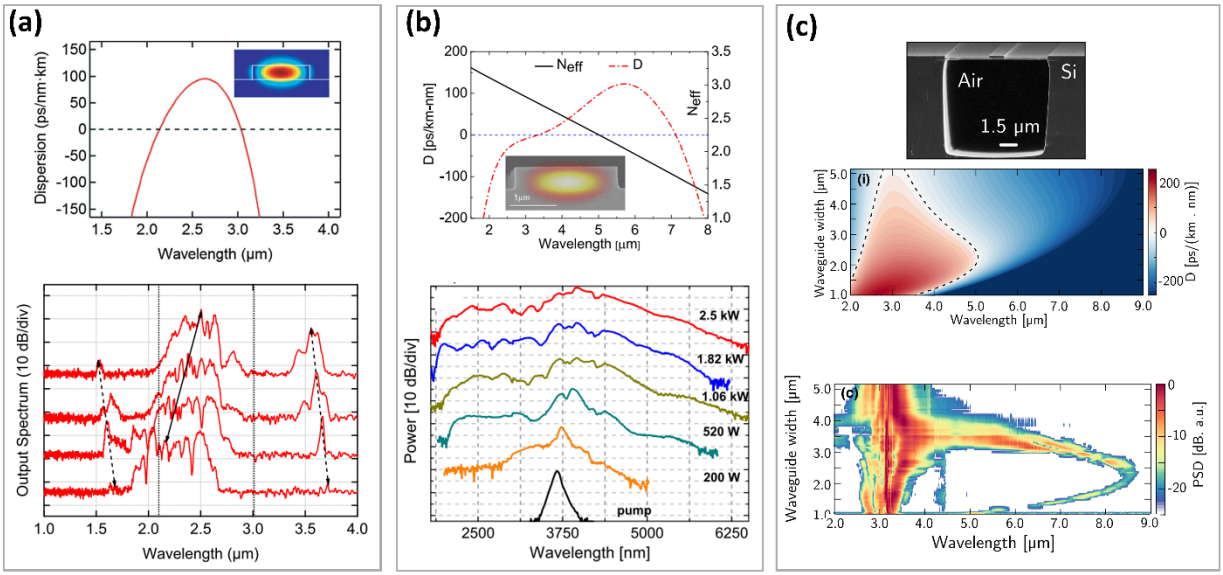


Figure 5.7: SCG in the mid-IR with silicon. (a) simulated GVD for TE mode (top) and experimental output spectra correspond to different pump wavelengths (bottom) of an SOI waveguide [61]; (b) simulated dispersion and effective index for the SOS nanowire (top) and experimental supercontinuum spectra with different input peak power (bottom) [39]; (c) SEM image of suspended Si waveguide (top), calculated GVD as a function of waveguides (middle), and measured supercontinuum spectra of the suspended Si waveguides pumped at 3.06 μm wavelength [71].

## 5.2 Supercontinuum generation in dispersion-engineered suspended Si waveguide with metamaterial cladding

Excitation of dispersive waves is a particularly appealing process allowing high-efficiency nonlinear wavelength conversion, exploiting phase-matching and frequency overlap of solitons and wavelengths in the normal dispersion regime [207]. In waveguides with non-negligible high-order dispersion coefficients ($\beta_{k>3} \neq 0$), which is generally the case in integrated photonics, at least two solutions exist for the phase-matching condition, resulting in the possible generation of two dispersive waves, one on each side of the soliton spectrum. The position of these two dispersive waves determines the maximum achievable bandwidth of supercontinuum generation (SCG).

Most on-chip SCG demonstrations utilized a similar approach to maximize the bandwidth, based on designing the waveguide cross section to excite dispersive waves with wavelengths located far away from the optical pump wavelength [39], [62], [65], [71], [72], [199]–[202], [208]–[214]. This strategy allowed remarkable SCG demonstrations, including among others, 1 octave SCG in the near-IR with indium gallium phosphide [208], 2.3 octaves SCG in the visible to mid-IR range with silicon nitride [212], 1.94 octaves SCG in the mid-IR range with

silicon [71], and 2.1 octaves SCG in the mid-IR range with germanium [72]. Still, proposed strip and rib waveguides yield limited flexibility in the control of the position of dispersive waves [213], [215], [216]. Phase-matching at the two sides of the soliton is strongly affected by variations in the waveguide dimensions, precluding independent selection of the position of the two dispersive waves.

Here, we show that metamaterial silicon waveguides release new degrees of freedom to select the wavelength of dispersive waves [13]. Based on this concept, we experimentally demonstrate excitation of two dispersive waves near 1.55 μm and 7.5 μm allowing ultra-wideband supercontinuum generation, covering most of the silicon transparency window. These results stand as an important milestone for versatile nonlinear frequency generation in silicon chips, with a great potential for applications in sensing, metrology and communications.

### 5.2.1 Dispersion engineering enabled by subwavelength metamaterial lateral cladding

In my dissertation, we propose the novel approach enabled by silicon subwavelength waveguides to tailor the excitation of dispersive waves. We exploit the unique geometrical degrees of freedom in the metamaterial waveguide to independently control the positions of the two dispersive waves. The proposed metamaterial waveguide is illustrated in Fig. 5.8 which is made up of a core strip and lateral metamaterial-grating served as cladding. In this structure, the metamaterial cladding with a period (Λ) less than half the pump wavelength, enables for the removal of the BOX under-cladding, eliminating silica absorption for wavelengths over 4 μm while maintaining mechanical stability and effective-low index cladding to confine the optical mode.

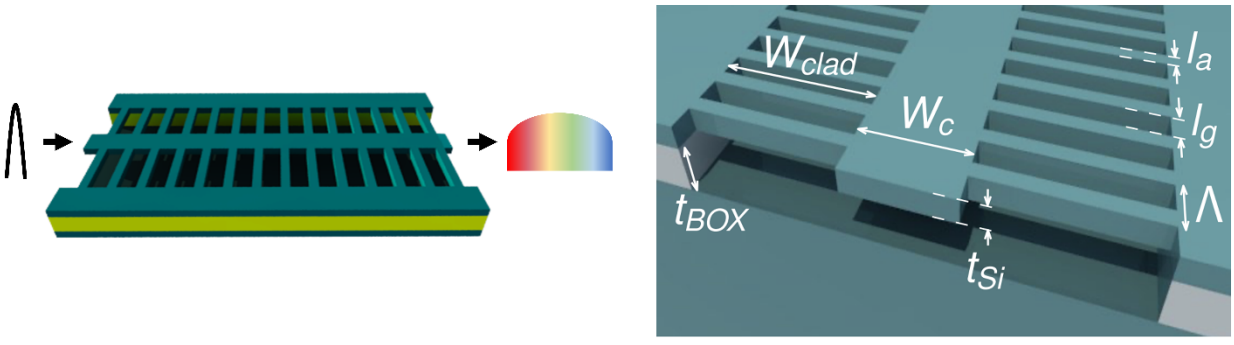


**Figure 5.8**: Schematic illustration of supercontinuum generation our proposed suspended Si SWG structure and detailed dimensions.

The metamaterial waveguide has a thickness of $t_{Si}$ = 700 nm, allowing fabrication with one lithography and one etching steps. The waveguide core has a width of $W_C$ (see Fig. 5.8). The metamaterial-grating cladding has a longitudinal period of Λ, with a gap length of lg and an anchoring arm length of $l_a$. The cladding width is set to $W_{clad}$ = 5 µm to avoid leakage towards the lateral silicon slabs.

To calculate the dispersion of the waveguide we use 3D FDTD simulations. The band structure calculation of SWG waveguide was presented in Chapter 2. The GVD of SWG is determined from the band structure calculation using the following equations:

$$D = \frac{c}{v_g^2 \lambda^2} \frac{\partial v_g}{\partial f} \tag{5.11}$$

Where group velocity $v_g = 2\pi\, \partial f / \partial k$, f is the frequency, k is the wavevector.

To illustrate the flexibility in controlling the dispersive wave position enabled by our approach, we evaluate the right-hand side of Eq. (5.9) for rib (Fig. 5.9a) and metamaterial (Fig. 5.9b-c) waveguides. The crossings by zero determine the position of the dispersive waves. We considered a pump wavelength of 3.5 µm with a peak power of 1 kW. For the rib waveguide, with a core width of $W_{Rib}$, we considered a core thickness of 700 nm and a slab thickness of 310 nm, similar to those used in ref [71]. The dispersion of the rib waveguide can be calculated based on two-dimensional modal analysis, which we perform using finite-difference eigenmode (FDE) solver. In both cases we considered transverse-electric (TE) polarization.

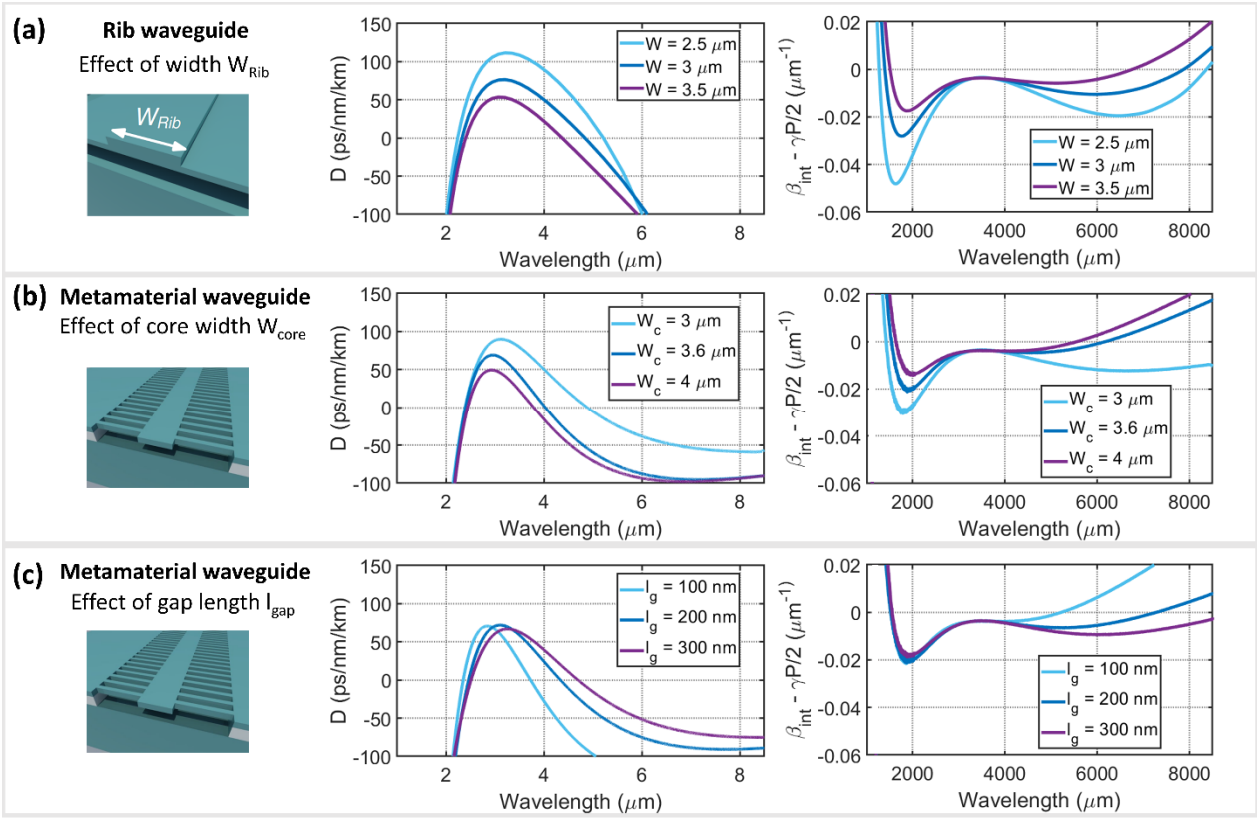


**Figure 5.9**: Calculated GVD and integrated dispersion for (a) considering the change of core width in Rib waveguide, (b) metamaterial waveguide variations in the core width $W_c$ (la = 150 nm and lg = 150 nm) (c) metamaterial waveguide: variation in the gap length $l_g$ (with $W_c$ = 3.6 μm).

As can be seen from Fig. 5.9a, the variations in rib core width ($W_{Rib}$) have a significant impact on the locations of both dispersive waves below and above the pump. When we specify a wavelength for one of the dispersive waves, the waveguide dispersion determines the location of the other. The lack of flexibility in controlling the location of the two dispersive waves makes it difficult to shape the nonlinear generation spectrum in a flexible manner. In the case of the metamaterial-cladded waveguide, the width of the waveguide core $W_C$ has significant influence on the GVD and position of both dispersive waves, as can be seen from Fig. 5.9b. Interestingly, the variations of the gap length ($l_g$) have a little effect on the zero-crossing point at shorter wavelengths but a significant effect at longer wavelengths. For example, we set one dispersive wave at 1.55 μm wavelength selecting a waveguide width of $W_C$ = 3.6 μm, we can modify the location of the other dispersive wave between 5 and 8 μm by changing $l_g$, as shown in Fig. 5.9c. Thus, the metamaterial waveguide core width and gap length can be employed to tailor the position of the dispersive wave at shorter and longer wavelengths. We take benefit of this unique flexibility enabled by SWG to create a waveguide with dispersive waves at 1.55 μm, in the center of the telecommunications C-band, and a

wavelength of 7.5 μm, near the border of the silicon transparency window. The proposed waveguide has $W_C$ = 3.6 μm, Λ = 350 nm, and $l_g$ = 200 nm.

### 5.2.2 Results and discussion

To validate the simulation result, we experimentally examined the effect of the gap length ($l_g$) metamaterial-grating waveguide on the position of the dispersive waves which directly affects the bandwidth of the generated supercontinuum. The suspended SWG were fabricated on a silicon-on-insulator (SOI) wafer with a silicon guiding layer of 700 nm thickness and a buried oxide (BOX) layer of 3 μm thickness. The fabrication processes are described in detail in Chapter 2. We fabricated three waveguides with the waveguide core width of $W_C$ = 3.6 μm, the anchoring arm length of $L_a$ = 150 nm, and different gap lengths of $l_g$ = 100 nm, 200 nm, and 300 nm, respectively. Figure 5.10 shows the SEM images of fabricated suspended SWG with the waveguide width of 3.6 μm, period of 350 nm, and the gap of 200 nm.

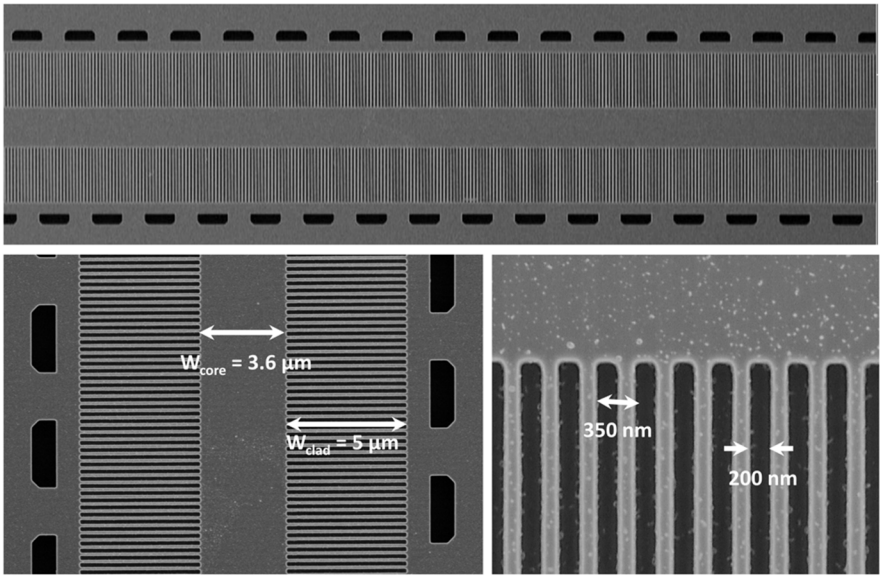


**Figure 5.10**: SEM images of the fabricated suspended SWG with the defined waveguide geometries: $W_{core}$ =3.6 μm, $W_{clqd}$ =5 μm, P = 350 nm, and g = 200 nm.

The supercontinuum generation and dispersive wave excitation are experimentally characterized using the setup described in Fig. 5.11. The suspended SWG waveguides are pumped using a femtosecond laser coupled to an optical parametric amplifier (OPA). The generated pulse has a 1 MHz repetition rate and a 220 fs pulse length. Light is injected and extracted from the chip facet using aspherical ZnSe lenses and 20 μm wide waveguides (insertion loss of ~ 12 dB). A polarization controller is used to selectively introduce TE polarized light into the chip. To examine the chip output, a monochromator and two photodetectors, an indium gallium arsenide photodetector for near-IR wavelengths (1-2.4 μm)

and a mercury cadmium telluride photodetector for mid-IR wavelengths (2.4-13 μm wavelength).

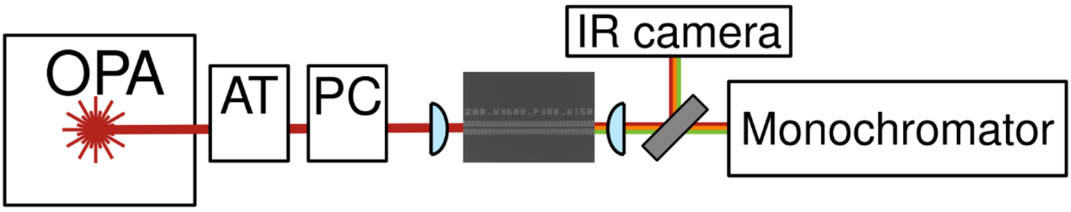


**Figure 5.11**: experimental setup used to characterize supercontinuum generation in suspended SWG.

Figure 5.12 shows the calculated integrated dispersion and experimental supercontinuum generation of metamaterial-grating waveguides with three different gap lengths of (a) $l_g$ = 100 nm, (b) $l_g$ = 200 nm, (c) $l_g$ = 300 nm. The length of the SWG waveguides is 4 mm, the pump wavelength at 3.5 μm, and the measured average power of approximately 3.5 mW (peak power ~ 1 kW). The position of measured short-wavelength and long-wavelength dispersive waves are marked with blue and green bars, respectively. For comparison, in Figure 5.12e-f we evaluate Eq. (5.9) for the three waveguides, considering a pump wavelength of 3.5 μm and a peak power of 1 kW. The crossings through zero indicate the calculated position of the dispersive waves. The dispersive wave positions obtained experimentally are in reasonably good agreement with the theoretical predictions via the waveguide integrated dispersion. The discrepancy in the short-wavelength dispersive wave position in the case of $l_g$ = 100 nm could be attributed to fabrication imperfections that are accentuated for smaller gaps. We note that for $l_g$ = 300 nm, the estimated position of the long-wavelength dispersive wave falls outside the silicon transparency window (1.1-8 μm wavelength), precluding experimental observation. The gap length of the metamaterial geometry has a strong effect on the position of the dispersive wave at longer wavelengths, while exhibiting a minor impact on the position of the short-wavelength dispersive wave. For gap length of $l_g$ = 200 nm, the supercontinuum spectrum expands over 2.35 octaves across a wavelength range between 1.53 μm and 7.8 μm wavelength (-20 dB bandwidth). For this waveguide configuration ($W_C$ = 3.6 μm, Λ = 350 nm, and $l_g$ = 200 nm) we measured propagation loss of 1-2 dB/cm in the 5-6 μm wavelength range, characterized using a quantum cascade laser with the cutback method with 6 different waveguides with lengths varying between 1.4 cm and 2.6 cm.

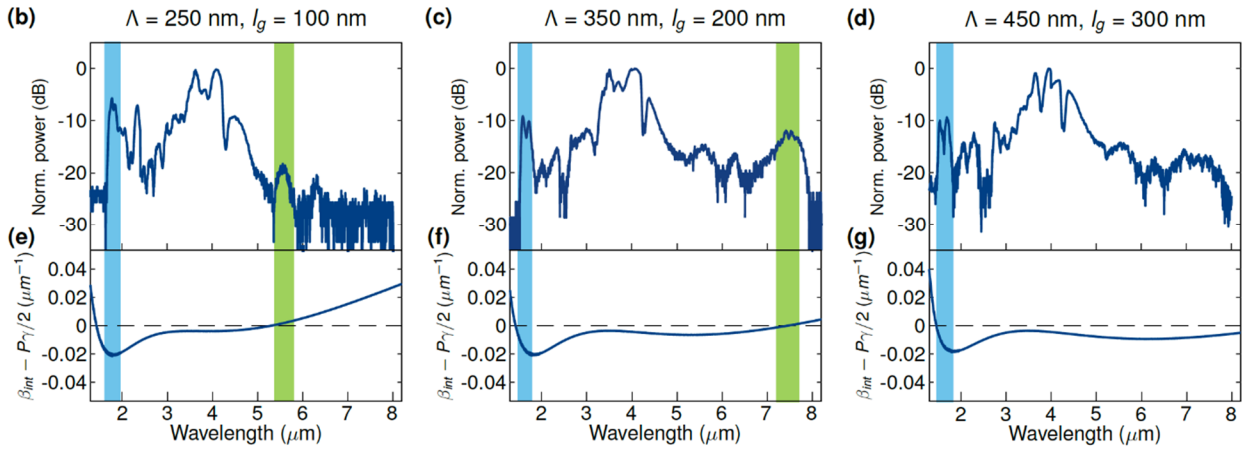


**Figure 5.12**: Calculated integrated dispersion and experimental supercontinuum characterization of metamaterial-grating waveguides with different gap lengths (a) $l_g$ = 100 nm, (b) $l_g$ = 200 nm, (c) $l_g$ = 300 nm, for injected wavelength of 3.5 µm and peak power of 1 kW. The grey region is corresponding to the dispersive wave positions at longer wavelength.

We have modelled the supercontinuum generation in the SWG waveguide by solving the generalized nonlinear Schrodinger equation (GNLSE) [197] using a 4th order Runge-Kutta algorithm [217], including the effect three-photon absorption [218].

$$\frac{\partial A}{\partial z} = -\frac{\alpha}{2}A + \sum_{k\geq 0}\beta_k \frac{i^k}{k!}\frac{\partial^k A}{\partial t^k} + i\gamma\left(1 + i\tau_{shock}\frac{\partial}{\partial t}\right)\left(|A|^2 A - \frac{\gamma_{3PA}}{3A_{eff}^2}|A^4|A\right) - \frac{\sigma}{2}(1 + i\mu)N_c A$$

Where A is the pulse temporal envelope, $\alpha$ is the propagation loss, z is the propagation distance. $\tau_{shock}$ describes the self-steepening effect and first-order frequency dependence of the modal area. $\gamma$ is nonlinear coefficient and it can be determined from the effective area $A_{eff}$ and the nonlinear index $n_2$ using equation (5.10). We consider the pump pulse with 220 fs duration, 1 MHz repetition rate, and a quadratic hyperbolic secant shape in time domain. We consider a nonlinear index silicon of $n_2 = 2.5 \times 10^{-18}$. For the calculation, we have used a pump wavelength of 3.5 µm and a peak power of 1 kW compatible with the measured average optical powers, taking into account the laser repetition rate and the insertion loss of the chip (~12 dB). The numerical simulation of the of the SCG have been performed using the codes developed by C. Lafforgue in our group.

Figure 5.13 shows the calculated evolution of the pulse in the spectral and temporal domain while it propagates along the suspended SWG waveguide ($Wc$ = 3.6 µm, Λ = 350 nm, $lg$ = 200 nm, L = 4 mm) with the peak power of 1 kW at input wavelength of 3.5 µm. As we can observe from the figure that the spectral broadening covers the wavelength range from 1.5 µm to roughly 8 µm, with the dispersive waves expanding at two wings of the spectrum located near 1.5 µm and 7.5 µm at level of -30 dB.

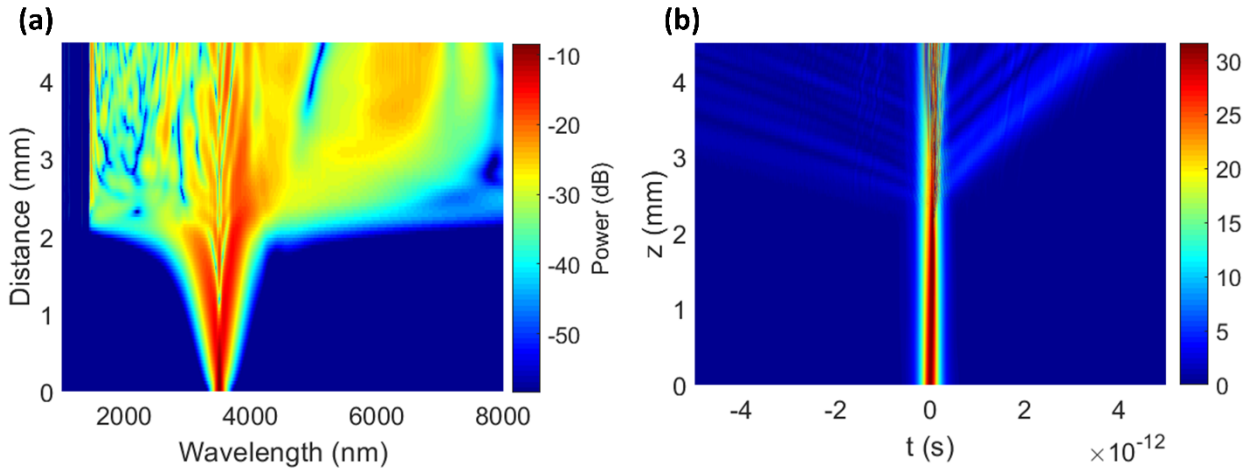


**Figure 5.13**: Numerical simulation of a pulse evolution in suspended silicon SWG waveguide (Wc = 3.6 µm, $\Lambda$ = 350 nm, lg = 200 nm, L = 4 mm) in (a) spectral and (b) temporal domain for a pump wavelength at 3.5 µm, and peak power of 1 kW.

## 5.3 Conclusion

In summary, we propose and demonstrate a novel approach to control the excitation of dispersive waves on chip by exploiting silicon metamaterial waveguides. We show that judicious optimization of metamaterial waveguide geometry can yield an effective and independent control of the position of the short-wavelength and long-wavelength dispersive waves [13]. We experimentally demonstrate tuning of the long-wavelength dispersive wave between 5.5 µm and 7.5 µm wavelength, with negligible variation of the short-wavelength dispersive wave. We use this dispersion engineering flexibility to demonstrate a supercontinuum expanding over 2.35 octaves, between two dispersive waves near 1.55 µm and 7.5 µm wavelength. This is, to the best of our knowledge, the widest supercontinuum generation in silicon and one of the widest demonstrations using integrated waveguides. These results open a promising route for the implementation of versatile nonlinear light broadening and frequency generation bridging telecom and mid-IR wavelengths using silicon photonics. We foresee that the metamaterial waveguide approach will foster the development of a new generation of high-performance nonlinear silicon photonic circuits exploiting flexible control of dispersive wave excitation for emerging applications in sensing metrology and communications.

# Chapter 6: Conclusions and perspectives

## Conclusions

This PhD work is framed within a long-term research activity focused on the development of integrated spectroscopic devices for sensing applications in the mid-IR, based on metamaterial-grating silicon waveguides. To that end, we have developed fundamental building blocks for sensing applications comprising of three major components: an ultra-broadband mid-IR supercontinuum source, a light-matter interaction component using metamaterial microring resonator, and SHFT spectrometers for spectrum analysis. Throughout this thesis, the SWG is the key and indispensable tool for improving functional devices. The suspended Si SWG platform is the practical solution to solve the silica absorption problems in the mid-IR, expanding the operating bandwidth of the SOI platform to cover the full silicon transparency window, from 1.1 μm to 8 μm wavelength. In addition, this PhD work studies the versatility and feasibility of SWG microstructures for controlling field confinement, effective index, phase-matching, and dispersion. During my PhD, I have performed modeling simulations, designs, and experimental characterizations.

I developed suspended silicon waveguides with metamaterial cladding to overcome the silica absorption limitation. I experimentally characterized demonstrated propagation losses of 1–2.5 dB/cm in the wavelength range between 5 μm and 7 μm. Such low propagation loss stands as an important advancement in suspended silicon photonic waveguides for the mid-IR, and are a key feature that allowed the demonstration of Fourier-transform spectrometer (see Chapter 4) supercontinuum generation (see Chapter 5). These suspended silicon SWG offer a wide range of opportunities to develop innovative photonic devices in the mid-IR range, particularly interesting for application in sensing, imaging, and free-space optical communications.

I presented and experimentally validated a novel type of nanophotonic waveguide that allows adjustable control of modal field confinement by incorporating two separate metamaterials in the core and cladding [14]. The dual-metamaterial design offers new degrees of freedom for shaping vertical and horizontal index contrast separately, as well as for engineering the single-mode condition. The vertical index contrast is determined by the metamaterial index in the core, whereas the horizontal index contrast and single-mode conditions are governed by the difference between the metamaterials in the core and cladding. The dual metamaterial waveguide allows for the seamless implementation of wider single-mode waveguides with tailored vertical and horizontal evanescent fields, maximizing overlap with the analyte while avoiding substrate leakage limits.

I have developed dual-metamaterial ring resonators working with TM polarization in SOI wafers with a 220-nm-thick guiding silicon layer, 3-μm-thick BOX, and air as a cladding. According to our 3D-FDTD simulations, the TM mode of our dual-metamaterial waveguide provides a higher external confinement factor in the air (0.35) than strip waveguides with TM polarization (0.3). My experiments confirmed that strip and dual-metamaterial ring resonators perform similar quality factors of around 30,000. The proposed dual-metamaterial metamaterial ring resonators are the promising alternative to conventional strip waveguides since they have similar quality factors and a greater bulk sensitivity. I also validated the simulation results by experimentally measuring the wavelength resonant shift with temperature variation.

I extended the dual-metamaterial concept, to implement full suspended waveguides, achieving excellent calculated bulk sensitivity of 1.35, which is 3.5-fold and 4.5-fold times higher than that of dual-metamaterial structure on silica cladding and conventional strip waveguide. The measured loaded quality factor of 20,000 at critical coupling with the extinction ratio of 25 dB, validate the feasibility of this approach.

The proposed dual-metamaterial approach offers an entire new set of capabilities for engineering the index profile in silicon waveguides that would otherwise be unachievable in state-of-the-art strip, slot, or SWG metamaterial geometries. The concept of a suspended structure can be further expanded for use in the longer mid-IR region.

In terms of the integrated spectroscopic devices, I have experimental demonstrated the Jacquinot's advantage in an integrated Si SHFTS, fabricated employing 193 nm deep-UV optical lithography with an integrated Ge photodetector array [15]. The device uses a new approach based on two-way-fed grating to implement a wide-area light collecting aperture of 90 μm × 60 μm that feeds 16 integrated MZIs simultaneously. Using a wide-area illumination beam of 0.5 mm FWHM, we show a measured 13 dB increase in étendue when compared to a conventional grating coupler.

I also demonstrated the first time SHFTS implemented with suspended silicon SWG platform working at mid-IR wavelengths [16]. This SHFTS allowed, for the first time, reaching mid-IR wavelengths in the 5-6 μm range with a silicon technology. The SHFTS is comprises 19 MZIs with a maximum imbalance length of 200 μm, achieving a measured resolution of 40 nm (~13 $cm^{-1}$) and a bandwidth of 380 nm (~100 $cm^{-1}$). The resolution and bandwidth can be readily improved in the future by increasing the optical path length difference and the number of integrated MZI. This work is the first demonstration of integrated SHFTS on suspended subwavelength grating working at mid-IR wavelength.

Finally, I have demonstrated a novel approach to control the excitation of dispersive waves on chip by exploiting silicon metamaterial waveguides [13]. Judicious optimization of metamaterial waveguide geometry can yield an effective and independent control of the position of the short-wavelength and long-wavelength dispersive waves. I experimentally demonstrate tuning of the long-wavelength dispersive wave between 5.5 μm and 7.5 μm wavelength, with negligible variation of the short-wavelength dispersive wave. I use this dispersion engineering flexibility to demonstrate a supercontinuum expanding over 2.35 octaves, between two dispersive waves near 1.55 μm and 7.5 μm wavelength. This is, to the best of our knowledge, the widest supercontinuum generation in silicon and one of the widest demonstrations using integrated waveguides. These results open a promising route for the implementation of versatile nonlinear light broadening and frequency generation bridging telecom and mid-IR wavelengths using silicon photonics. We foresee that the metamaterial waveguide approach will foster the development of a new generation of high-performance nonlinear silicon photonic circuits exploiting flexible control of dispersive wave excitation for emerging applications in sensing metrology and communications.

## Perspectives and future work

This PhD work has opened different routes for the development of high-performance silicon photonic circuits for applications in the mid-IR. I highlight some of them here.

We have proposed and experimentally demonstrated the low propagation losses of suspended waveguide with metamaterial-grating lateral cladding in mid infrared wavelength range. In the short-term perspective, it would be interesting to study numerically and experimentally the propagation losses of the suspended subwavelength-cladding waveguide considering the lateral leakage, vertical leakage, fabrication losses, and intrinsic loses of the materials. Based on that, it is feasible to improve the propagation loss by optimizing the fabrication processes and waveguide dimensions including width, thickness, single-mode condition for TE, TM mode, and so on.

We already successfully developed dual-metamaterial Si structures for enhancing the light-matter interaction in near-IR wavelengths. Still, the practical demonstration of this approach for mid-IR wavelengths is lacking. Therefore, we want to take advantage of this dual-metamaterial approach to demonstrate high-performance suspended micro-ring resonators in the mid-IR wavelength range, containing key features several important substances, e.g. $CH_4$, $NO_2$, $NH_3$ and $H_2S$. Such resonators, could enable actual gas sensing experiments in the mid-IR.

In terms of supercontinuum generation, we want to develop deeper understanding of the links between the geometrical parameters of the SWG-cladding and the dispersion properties to improve frequency conversion efficiency. More research should be carried out to optimize a flatter broadband spectrum and achieve a high coherence source. The findings in the SC generation have suggested new opportunities to discover more interesting applications. Besides supercontinuum

generation, the capability in engineering the group velocity dispersion of the metamaterial-cladding waveguide is also beneficial for different nonlinear applications, including pulse compression, parametric conversions, and frequency combs.

This work in this PhD set the initial foundation for the development of complete set of spectrometer devices in a single chip. The questions raised in this section are whether these functional components can be combined to build full integrated complex devices. A further study could assess the integration the whole passive devices including fiber-chip couplers, ring resonators, multiplexer, and Fourier Transform spectroscopy. In addition, another critical objective that should take into consideration is the integration of the mid-IR source. The nonlinear SC generation spectrum requires sufficiently high-power light source to seed the nonlinear generation. Therefore, it necessitates an external mid-IR source with sufficient power. Further improvements of the nonlinear efficiency and light injection efficiency may allow using high-performance mid-IR quantum cascade lasers or interband cascade lasers for pumping the nonlinear generation. And finally, greater efforts are needed to combine both nonlinear mid-IR source with passive devices including sensing element using micro-ring resonator, and SHFT spectrometers.

# Publication list

**International journal papers:**

1. C. Lafforgue, M. Montesinos-Ballester, T. T. D Dinh, X. Le Roux, E. Cassan, D. Marris-Morini, C. Alonso-Ramos, and L. Vivien, "Supercontinuum generation in silicon photonics platforms", Photonic Research, Vol. 10, Issue 3, pp. A43-A56 (2022).

2. T. T. D. Dinh, X. Le Roux, N. Koompai, D. Melati, M. Montesinos-Ballester, D. González-Andrade, P. Cheben, A. V. Velasco, E. Cassan, D. Marris-Morini, L. Vivien, and C. Alonso-Ramos, "Mid-infrared Fourier-transform spectrometer based on metamaterial lateral cladding suspended silicon waveguides", Optics Letters, Vol. 47, Issue 4, pp. 810-813 (2022).

3. V. Vakarin, D. Melati, T. T. D. Dinh, X. Le Roux, W. Kut King Kan, C. Dupré, B. Szelag, S. Monfray, F. Boeuf, P. Cheben, E. Cassan, D. Marris-Morini, L. Vivien and C. Alberto Alonso-Ramos, "Metamaterial-Engineered Silicon Beam Splitter Fabricated with Deep UV Immersion Lithography", Nanomaterials 11, 2949 (2021).

4. D. González-Andrade, T. T. D. Dinh, S. Guerber, N. Vulliet, S. Cremer, S. Monfray, E. Cassan, D. Marris-Morini, F. Boeuf, P. Cheben, L. Vivien, A. V. Velasco, and C. Alonso-Ramos, "Broadband Fourier-transform silicon nitride spectrometer with wide-area multiaperture input", Optics Letters. Vol. 46, Issue 16, pp. 4021-4024 (2021).

5. T. T. D. Dinh, D. González-Andrade, M. Montesinos-Ballester, L. Deniel, B. Szelag, X. Le Roux, E. Cassan, D. Marris-Morini, L. Vivien, P. Cheben, A. V. Velasco, and C. Alonso-Ramos, "Silicon photonic on-chip spatial heterodyne Fourier transform spectrometer exploiting the Jacquinot's advantage", Optics Letters Vol. 46, Issue 6, pp. 1341-1344 (2021).

6. T. T. D. Dinh et al., "Shaping the modal confinement in silicon nanophotonic waveguides through dual-metamaterial engineering," arXiv preprint arXiv:2105.14929, 2021 (Under review).
7. T. T. D. Dinh et al., "Dispersive wave control enabled by silicon metamaterial waveguides," arXiv preprint arXiv:2201.06516, 2022.

# References


[1] Barbara H. Stuart, *Infrared spectroscopy: Fundamentals and Applications*. 2004.

[2] E. Ng and R. Acharya, "Remote-sensing infrared thermography," *IEEE Eng. Med. Biol. Mag.*, vol. 28, no. 1, pp. 76–83, Jan. 2009, doi: 10.1109/MEMB.2008.931018.

[3] R. Furstenberg *et al.*, "Stand-off detection of trace explosives via resonant infrared photothermal imaging," *Appl. Phys. Lett.*, vol. 93, no. 22, p. 224103, Dec. 2008, doi: 10.1063/1.3027461.

[4] M. C. Estevez, M. Alvarez, and L. M. Lechuga, "Integrated optical devices for lab-on-a-chip biosensing applications: Integrated optical biosensors," *Laser & Photon. Rev.*, vol. 6, no. 4, pp. 463–487, Jul. 2012, doi: 10.1002/lpor.201100025.

[5] T. Hu *et al.*, "Silicon photonic platforms for mid-infrared applications [Invited]," *Photon. Res.*, vol. 5, no. 5, p. 417, Oct. 2017, doi: 10.1364/PRJ.5.000417.

[6] C. Hughes and M. J. Baker, "Can mid-infrared biomedical spectroscopy of cells, fluids and tissue aid improvements in cancer survival? A patient paradigm," *Analyst*, vol. 141, no. 2, pp. 467–475, 2016, doi: 10.1039/C5AN01858G.

[7] M.-C. Yu *et al.*, "Label Free Detection of Sensitive Mid-Infrared Biomarkers of Glomerulonephritis in Urine Using Fourier Transform Infrared Spectroscopy," *Sci Rep*, vol. 7, no. 1, p. 4601, Dec. 2017, doi: 10.1038/s41598-017-04774-7.

[8] M. Paraskevaidi *et al.*, "Potential of mid-infrared spectroscopy as a non-invasive diagnostic test in urine for endometrial or ovarian cancer," *Analyst*, vol. 143, no. 13, pp. 3156–3163, 2018, doi: 10.1039/C8AN00027A.

[9] B. Horn, S. Esslinger, M. Pfister, C. Fauhl-Hassek, and J. Riedl, "Non-targeted detection of paprika adulteration using mid-infrared spectroscopy and one-class classification – Is it data preprocessing that makes the performance?," *Food Chemistry*, vol. 257, pp. 112–119, Aug. 2018, doi: 10.1016/j.foodchem.2018.03.007.

[10] R. Stach, B. Pejcic, E. Crooke, M. Myers, and B. Mizaikoff, "Mid-Infrared Spectroscopic Method for the Identification and Quantification of Dissolved Oil Components in Marine Environments," *Anal. Chem.*, vol. 87, no. 24, pp. 12306–12312, Dec. 2015, doi: 10.1021/acs.analchem.5b03624.

[11] L. Cunningham, J. Tibby, S. Forrester, C. Barr, and J. Skjemstad, "Mid-Infrared Spectroscopy as a Potential Tool for Reconstructing Lake Salinity," *Water*, vol. 8, no. 11, p. 479, Oct. 2016, doi: 10.3390/w8110479.

[12] D. Farrah *et al.*, "High-Resolution Mid-Infrared Spectroscopy of Ultraluminous Infrared Galaxies," *ApJ*, vol. 667, no. 1, pp. 149–169, Sep. 2007, doi: 10.1086/520834.

[13] T. T. D. Dinh *et al.*, "Dispersive wave control enabled by silicon metamaterial waveguides," p. 5.

[14] T. T. D. Dinh *et al.*, "Shaping the modal confinement in silicon nanophotonic waveguides through dual-metamaterial engineering," p. 11.
[15] T. T. D. Dinh *et al.*, "Silicon photonic on-chip spatial heterodyne Fourier transform spectrometer exploiting the Jacquinot's advantage," *Opt. Lett.*, vol. 46, no. 6, p. 1341, Mar. 2021, doi: 10.1364/OL.418278.
[16] T. T. Duong Dinh *et al.*, "Mid-infrared Fourier-transform spectrometer based on metamaterial lateral cladding suspended silicon waveguides," *Opt. Lett.*, vol. 47, no. 4, p. 810, Feb. 2022, doi: 10.1364/OL.450719.
[17] R. Soref, "Mid-infrared photonics in silicon and germanium," *Nature Photon*, vol. 4, no. 8, pp. 495–497, Aug. 2010, doi: 10.1038/nphoton.2010.171.
[18] J. M. Ramirez *et al.*, "Low-loss Ge-rich Si_02Ge_08 waveguides for mid-infrared photonics," *Opt. Lett.*, vol. 42, no. 1, p. 105, Jan. 2017, doi: 10.1364/OL.42.000105.
[19] V. Vakarin *et al.*, "Wideband Ge-Rich SiGe Polarization-Insensitive Waveguides for Mid-Infrared Free-Space Communications," *Applied Sciences*, vol. 8, no. 7, p. 1154, Jul. 2018, doi: 10.3390/app8071154.
[20] S. Khan, J. Chiles, J. Ma, and S. Fathpour, "Silicon-on-nitride waveguides for mid- and near-infrared integrated photonics," *Appl. Phys. Lett.*, vol. 102, no. 12, p. 121104, Mar. 2013, doi: 10.1063/1.4798557.
[21] N. Hô *et al.*, "Single-mode low-loss chalcogenide glass waveguides for the mid-infrared," *Opt. Lett.*, vol. 31, no. 12, p. 1860, Jun. 2006, doi: 10.1364/OL.31.001860.
[22] P. Ma *et al.*, "Low-loss chalcogenide waveguides for chemical sensing in the mid-infrared," *Opt. Express*, vol. 21, no. 24, p. 29927, Dec. 2013, doi: 10.1364/OE.21.029927.
[23] T. Baehr-Jones *et al.*, "Silicon-on-sapphire integrated waveguides for the mid-infrared," *Opt. Express*, vol. 18, no. 12, p. 12127, Jun. 2010, doi: 10.1364/OE.18.012127.
[24] R. Shankar, I. Bulu, and M. Lončar, "Integrated high-quality factor silicon-on-sapphire ring resonators for the mid-infrared," *Appl. Phys. Lett.*, vol. 102, no. 5, p. 051108, Feb. 2013, doi: 10.1063/1.4791558.
[25] Z. Cheng, X. Chen, C. Y. Wong, K. Xu, and H. K. Tsang, "Mid-infrared Suspended Membrane Waveguide and Ring Resonator on Silicon-on-Insulator," *IEEE Photonics J.*, vol. 4, no. 5, pp. 1510–1519, Oct. 2012, doi: 10.1109/JPHOT.2012.2210700.
[26] M. M. Milošević *et al.*, "Silicon waveguides and devices for the mid-infrared," *Appl. Phys. Lett.*, vol. 101, no. 12, p. 121105, Sep. 2012, doi: 10.1063/1.4753948.
[27] J. Soler Penades, A. Khokhar, M. Nedeljkovic, and G. Mashanovich, "Low Loss Mid-Infrared SOI Slot Waveguides," *IEEE Photon. Technol. Lett.*, pp. 1–1, 2015, doi: 10.1109/LPT.2015.2414791.
[28] S. A. Miller *et al.*, "Low-loss silicon platform for broadband mid-infrared photonics," *Optica*, vol. 4, no. 7, p. 707, Jul. 2017, doi: 10.1364/OPTICA.4.000707.
[29] Y.-C. Chang, V. Paeder, L. Hvozdara, J.-M. Hartmann, and H. P. Herzig, "Low-loss germanium strip waveguides on silicon for the mid-infrared," *Opt. Lett.*, vol. 37, no. 14, p. 2883, Jul. 2012, doi: 10.1364/OL.37.002883.

[30] M. Nedeljkovic *et al.*, "Surface-Grating-Coupled Low-Loss Ge-on-Si Rib Waveguides and Multimode Interferometers," *IEEE Photon. Technol. Lett.*, vol. 27, no. 10, pp. 1040–1043, May 2015, doi: 10.1109/LPT.2015.2405611.

[31] W. Li *et al.*, "Germanium-on-silicon nitride waveguides for mid-infrared integrated photonics," *Appl. Phys. Lett.*, vol. 109, no. 24, p. 241101, Dec. 2016, doi: 10.1063/1.4972183.

[32] A. Sánchez-Postigo *et al.*, "Suspended germanium waveguides with subwavelength-grating metamaterial cladding for the mid-infrared band," *Opt. Express*, vol. 29, no. 11, p. 16867, May 2021, doi: 10.1364/OE.422764.

[33] A. Osman *et al.*, "Suspended low-loss germanium waveguides for the longwave infrared," *Opt. Lett.*, vol. 43, no. 24, p. 5997, Dec. 2018, doi: 10.1364/OL.43.005997.

[34] J. S. Penades *et al.*, "Suspended silicon mid-infrared waveguide devices with subwavelength grating metamaterial cladding," *Opt. Express*, vol. 24, no. 20, p. 22908, Oct. 2016, doi: 10.1364/OE.24.022908.

[35] W. Liu *et al.*, "Suspended silicon waveguide platform with subwavelength grating metamaterial cladding for long-wave infrared sensing applications," *Nanophotonics*, vol. 10, no. 7, pp. 1861–1870, May 2021, doi: 10.1515/nanoph-2021-0029.

[36] J. S. Penadés *et al.*, "Suspended silicon waveguides for long-wave infrared wavelengths," *Opt. Lett.*, vol. 43, no. 4, p. 795, Feb. 2018, doi: 10.1364/OL.43.000795.

[37] C. Y. Wong *et al.*, "Characterization of Mid-Infrared Silicon-on-Sapphire Microring Resonators With Thermal Tuning," *IEEE Photonics J.*, vol. 4, no. 4, pp. 1095–1102, Aug. 2012, doi: 10.1109/JPHOT.2012.2204734.

[38] Y. Zou *et al.*, "Grating-coupled silicon-on-sapphire integrated slot waveguides operating at mid-infrared wavelengths," *Opt. Lett.*, vol. 39, no. 10, p. 3070, May 2014, doi: 10.1364/OL.39.003070.

[39] N. Singh *et al.*, "Midinfrared supercontinuum generation from 2 to 6 μm in a silicon nanowire," *Optica*, vol. 2, no. 9, p. 797, Sep. 2015, doi: 10.1364/OPTICA.2.000797.

[40] C. Ranacher *et al.*, "Mid-infrared absorption gas sensing using a silicon strip waveguide," *Sensors and Actuators A: Physical*, vol. 277, pp. 117–123, Jul. 2018, doi: 10.1016/j.sna.2018.05.013.

[41] J. Soler Penadés *et al.*, "Suspended SOI waveguide with sub-wavelength grating cladding for mid-infrared," *Opt. Lett.*, vol. 39, no. 19, p. 5661, Oct. 2014, doi: 10.1364/OL.39.005661.

[42] J. Chiles, S. Khan, J. Ma, and S. Fathpour, "High-contrast, all-silicon waveguiding platform for ultra-broadband mid-infrared photonics," *Appl. Phys. Lett.*, vol. 103, no. 15, p. 151106, Oct. 2013, doi: 10.1063/1.4824771.

[43] Y. Wei *et al.*, "Long-wave infrared 1 × 2 MMI based on air-gap beneath silicon rib waveguides," *Opt. Express*, vol. 19, no. 17, p. 15803, Aug. 2011, doi: 10.1364/OE.19.015803.

[44] W. Zhou, Z. Cheng, X. Wu, X. Sun, and H. K. Tsang, "Fully suspended slot waveguide platform," *Journal of Applied Physics*, vol. 123, no. 6, p. 063103, Feb. 2018, doi: 10.1063/1.5017780.

[45] K. Gallacher *et al.*, "Low loss Ge-on-Si waveguides operating in the 8–14 μm atmospheric transmission window," *Opt. Express*, vol. 26, no. 20, p. 25667, Oct. 2018, doi: 10.1364/OE.26.025667.

[46] J. Kang, M. Takenaka, and S. Takagi, "Novel Ge waveguide platform on Ge-on-insulator wafer for mid-infrared photonic integrated circuits," *Opt. Express*, vol. 24, no. 11, p. 11855, May 2016, doi: 10.1364/OE.24.011855.

[47] J. M. Ramirez *et al.*, "Broadband integrated racetrack ring resonators for long-wave infrared photonics," *Opt. Lett.*, vol. 44, no. 2, p. 407, Jan. 2019, doi: 10.1364/OL.44.000407.

[48] S. Zheng, H. Cai, Y. D. Gu, L. K. Chin, and A. Q. Liu, "On-chip Fourier Transform Spectrometer for Chemical Sensing Applications," in *Conference on Lasers and Electro-Optics*, San Jose, California, 2016, p. AM1J.6. doi: 10.1364/CLEO_AT.2016.AM1J.6.

[49] A. B. Seddon, "Chalcogenide glasses: a review of their preparation, properties and applications," *Journal of Non-Crystalline Solids*, vol. 184, pp. 44–50, May 1995, doi: 10.1016/0022-3093(94)00686-5.

[50] B. Bureau *et al.*, "Chalcogenide optical fibers for mid-infrared sensing," *Opt. Eng*, vol. 53, no. 2, p. 027101, Feb. 2014, doi: 10.1117/1.OE.53.2.027101.

[51] K. Shimakawa, A. Kolobov, and S. R. Elliott, "Photoinduced effects and metastability in amorphous semiconductors and insulators," *null*, vol. 44, no. 6, pp. 475–588, Dec. 1995, doi: 10.1080/00018739500101576.

[52] K. Tanaka, "Photoinduced structural changes in amorphous semiconductors," p. 6, 1998.

[53] H. Lin *et al.*, "Mid-infrared integrated photonics on silicon: a perspective," *Nanophotonics*, vol. 7, no. 2, pp. 393–420, Dec. 2017, doi: 10.1515/nanoph-2017-0085.

[54] Y. Zou, S. Chakravarty, C.-J. Chung, X. Xu, and R. T. Chen, "Mid-infrared silicon photonic waveguides and devices [Invited]," *Photon. Res.*, vol. 6, no. 4, p. 254, Apr. 2018, doi: 10.1364/PRJ.6.000254.

[55] A. Spott *et al.*, "Quantum cascade laser on silicon," *Optica*, vol. 3, no. 5, p. 545, May 2016, doi: 10.1364/OPTICA.3.000545.

[56] Faist Jerome, Capasso Federico, Sivco Deborah L., Sirtori Carlo, Hutchinson Albert L., and Cho Alfred Y., "Quantum Cascade Laser," *Science*, vol. 264, no. 5158, pp. 553–556, Apr. 1994, doi: 10.1126/science.264.5158.553.

[57] G. K. Veerabathran, S. Sprengel, A. Andrejew, and M.-C. Amann, "Room-temperature vertical-cavity surface-emitting lasers at 4 $\mu$ m with GaSb-based type-II quantum wells," *Appl. Phys. Lett.*, vol. 110, no. 7, p. 071104, Feb. 2017, doi: 10.1063/1.4975813.

[58] L. Zhang, A. M. Agarwal, L. C. Kimerling, and J. Michel, "Nonlinear Group IV photonics based on silicon and germanium: from near-infrared to mid-infrared," *Nanophotonics*, vol. 3, no. 4–5, pp. 247–268, Aug. 2014, doi: 10.1515/nanoph-2013-0020.

[59] J. Wu, S. Jiang, T. Qua, M. Kuwata-Gonokami, and N. Peyghambarian, "2μm lasing from highly thulium doped tellurite glass microsphere," *Appl. Phys. Lett.*, vol. 87, no. 21, p. 211118, Nov. 2005, doi: 10.1063/1.2132532.

[60] B. Kuyken *et al.*, "Generation of 36 μm radiation and telecom-band amplification by four-wave mixing in a silicon waveguide with normal group velocity dispersion," *Opt. Lett.*, vol. 39, no. 6, p. 1349, Mar. 2014, doi: 10.1364/OL.39.001349.

[61] R. K. W. Lau, M. R. E. Lamont, A. G. Griffith, Y. Okawachi, M. Lipson, and A. L. Gaeta, "Octave-spanning mid-infrared supercontinuum generation in silicon nanowaveguides," *Opt. Lett.*, vol. 39, no. 15, p. 4518, Aug. 2014, doi: 10.1364/OL.39.004518.

[62] A. Della Torre *et al.*, "Mid-infrared supercontinuum generation in a low-loss germanium-on-silicon waveguide," *APL Photonics*, vol. 6, no. 1, p. 016102, Jan. 2021, doi: 10.1063/5.0033070.

[63] Y. Okawachi, K. Saha, J. S. Levy, Y. H. Wen, M. Lipson, and A. L. Gaeta, "Octave-spanning frequency comb generation in a silicon nitride chip," *Opt. Lett.*, vol. 36, no. 17, p. 3398, Sep. 2011, doi: 10.1364/OL.36.003398.

[64] Y. Yu *et al.*, "Experimental demonstration of linearly polarized 2–10 μm supercontinuum generation in a chalcogenide rib waveguide," *Opt. Lett.*, vol. 41, no. 5, p. 958, Mar. 2016, doi: 10.1364/OL.41.000958.

[65] R. Kou *et al.*, "Mid-IR broadband supercontinuum generation from a suspended silicon waveguide," *Opt. Lett.*, vol. 43, no. 6, p. 1387, Mar. 2018, doi: 10.1364/OL.43.001387.

[66] S. Zlatanovic *et al.*, "Mid-infrared wavelength conversion in silicon waveguides using ultracompact telecom-band-derived pump source," *Nature Photon*, vol. 4, no. 8, pp. 561–564, Aug. 2010, doi: 10.1038/nphoton.2010.117.

[67] V. Raghunathan, D. Borlaug, R. R. Rice, and B. Jalali, "Demonstration of a Mid-infrared silicon Raman amplifier," *Opt. Express*, vol. 15, no. 22, p. 14355, 2007, doi: 10.1364/OE.15.014355.

[68] M. Yu, Y. Okawachi, A. G. Griffith, M. Lipson, and A. L. Gaeta, "Mode-locked mid-infrared frequency combs in a silicon microresonator," *Optica*, vol. 3, no. 8, p. 854, Aug. 2016, doi: 10.1364/OPTICA.3.000854.

[69] T. J. Kippenberg, R. Holzwarth, and S. A. Diddams, "Microresonator-Based Optical Frequency Combs," vol. 332, p. 6, 2011.

[70] C. F. Kaminski, R. S. Watt, A. D. Elder, J. H. Frank, and J. Hult, "Supercontinuum radiation for applications in chemical sensing and microscopy," *Appl. Phys. B*, vol. 92, no. 3, pp. 367–378, Sep. 2008, doi: 10.1007/s00340-008-3132-1.

[71] N. Nader *et al.*, "Infrared frequency comb generation and spectroscopy with suspended silicon nanophotonic waveguides," *Optica*, vol. 6, no. 10, p. 1269, Oct. 2019, doi: 10.1364/OPTICA.6.001269.

[72] M. Montesinos-Ballester *et al.*, "On-Chip Mid-Infrared Supercontinuum Generation from 3 to 13 μm Wavelength," *ACS Photonics*, vol. 7, no. 12, pp. 3423–3429, Dec. 2020, doi: 10.1021/acsphotonics.0c01232.

[73] R. Wang *et al.*, "III-V-on-silicon 2-μm-wavelength-range wavelength demultiplexers with heterogeneously integrated InP-based type-II photodetectors," *Opt. Express*, vol. 24, no. 8, p. 8480, Apr. 2016, doi: 10.1364/OE.24.008480.

[74] Z. Han *et al.*, "On-chip chalcogenide glass waveguide-integrated mid-infrared PbTe detectors," *Appl. Phys. Lett.*, vol. 109, no. 7, p. 071111, Aug. 2016, doi: 10.1063/1.4961532.

[75] X. Wang, Z. Cheng, K. Xu, H. K. Tsang, and J.-B. Xu, "High-responsivity graphene/silicon-heterostructure waveguide photodetectors," *Nature Photon*, vol. 7, no. 11, pp. 888–891, Nov. 2013, doi: 10.1038/nphoton.2013.241.

[76] J. J. Ackert *et al.*, "High-speed detection at two micrometres with monolithic silicon photodiodes," *Nature Photon*, vol. 9, no. 6, pp. 393–396, Jun. 2015, doi: 10.1038/nphoton.2015.81.

[77] C. Alonso-Ramos *et al.*, "Germanium-on-silicon mid-infrared grating couplers with low-reflectivity inverse taper excitation," *Opt. Lett.*, vol. 41, no. 18, p. 4324, Sep. 2016, doi: 10.1364/OL.41.004324.

[78] S. Radosavljevic, B. Kuyken, and G. Roelkens, "Efficient 52 μm wavelength fiber-to-chip grating couplers for the Ge-on-Si and Ge-on-SOI mid-infrared waveguide platform," *Opt. Express*, vol. 25, no. 16, p. 19034, Aug. 2017, doi: 10.1364/OE.25.019034.

[79] H. Lin *et al.*, "Demonstration of high-Q mid-infrared chalcogenide glass-on-silicon resonators," *Opt. Lett.*, vol. 38, no. 9, p. 1470, May 2013, doi: 10.1364/OL.38.001470.

[80] T. Hu *et al.*, "A Polarization Splitter and Rotator Based on a Partially Etched Grating-Assisted Coupler," *IEEE Photon. Technol. Lett.*, vol. 28, no. 8, pp. 911–914, Apr. 2016, doi: 10.1109/LPT.2016.2517196.

[81] Zhenzhou Cheng *et al.*, "Mid-Infrared Grating Couplers for Silicon-on-Sapphire Waveguides," *IEEE Photonics J.*, vol. 4, no. 1, pp. 104–113, Feb. 2012, doi: 10.1109/JPHOT.2011.2179921.

[82] R. Shankar, R. Leijssen, I. Bulu, and M. Lončar, "Mid-infrared photonic crystal cavities in silicon," p. 8, 2011.

[83] P. Cheben, D.-X. Xu, S. Janz, and A. Densmore, "Subwavelength waveguide grating for mode conversion and light coupling in integrated optics," *Opt. Express*, vol. 14, no. 11, p. 4695, 2006, doi: 10.1364/OE.14.004695.

[84] P. Cheben *et al.*, "Refractive index engineering with subwavelength gratings for efficient microphotonic couplers and planar waveguide multiplexers," *Opt. Lett.*, vol. 35, no. 15, p. 2526, Aug. 2010, doi: 10.1364/OL.35.002526.

[85] P. Cheben, R. Halir, J. H. Schmid, H. A. Atwater, and D. R. Smith, "Subwavelength integrated photonics," *Nature*, vol. 560, no. 7720, pp. 565–572, Aug. 2018, doi: 10.1038/s41586-018-0421-7.

[86] R. Halir *et al.*, "Subwavelength-Grating Metamaterial Structures for Silicon Photonic Devices," *Proc. IEEE*, vol. 106, no. 12, pp. 2144–2157, Dec. 2018, doi: 10.1109/JPROC.2018.2851614.

[87] Robert Halir, Przemek J. Bock, Pavel Cheben, Alejandro Ortega-Monux , Carlos Alonso-Ramos, Jens H. Schmid, Jean Lapointe, Dan-Xia Xu, and J. Gonzalo Wanguemert-Perez, Inigo Molina-Fernandez , and Siegfried Janz, "Waveguide sub-wavelength structures: a review of principles and applications," *Laser & Photonics Reviews*, pp. 25–49, 2015, doi: 10.1002/lpor.201400083.

[88] J. M. Luque-González *et al.*, "A review of silicon subwavelength gratings: building break-through devices with anisotropic metamaterials," *Nanophotonics*, vol. 10, no. 11, pp. 2765–2797, Aug. 2021, doi: 10.1515/nanoph-2021-0110.

[89] R. Halir, P. Cheben, S. Janz, D.-X. Xu, Í. Molina-Fernández, and J. G. Wangüemert-Pérez, "Waveguide grating coupler with subwavelength microstructures," *Opt. Lett.*, vol. 34, no. 9, p. 1408, May 2009, doi: 10.1364/OL.34.001408.

[90] Yongbo Tang, Daoxin Dai, and Sailing He, "Proposal for a Grating Waveguide Serving as Both a Polarization Splitter and an Efficient Coupler for Silicon-on-Insulator Nanophotonic Circuits," *IEEE Photon. Technol. Lett.*, vol. 21, no. 4, pp. 242–244, Feb. 2009, doi: 10.1109/LPT.2008.2010528.

[91] G. Roelkens, D. Van Thourhout, and R. Baets, "Silicon-on-insulator ultra-compact duplexer based on a diffractive grating structure," *Opt. Express*, vol. 15, no. 16, p. 10091, 2007, doi: 10.1364/OE.15.010091.

[92] D. Oser *et al.*, "Subwavelength engineering and asymmetry: two efficient tools for sub-nanometer-bandwidth silicon Bragg filters," *Opt. Lett.*, vol. 43, no. 14, p. 3208, Jul. 2018, doi: 10.1364/OL.43.003208.

[93] V. M. N. Passaro, R. Loiacono, G. D'Amico, and F. De Leonardis, "Design of Bragg Grating Sensors Based on Submicrometer Optical Rib Waveguides in SOI," *IEEE Sensors J.*, vol. 8, no. 9, pp. 1603–1611, Sep. 2008, doi: 10.1109/JSEN.2008.929068.

[94] Shyh Wang, "Principles of distributed feedback and distributed Bragg-reflector lasers," *IEEE J. Quantum Electron.*, vol. 10, no. 4, pp. 413–427, Apr. 1974, doi: 10.1109/JQE.1974.1068152.

[95] J. L. Jewell, J. P. Harbison, A. Scherer, Y. H. Lee, and L. T. Florez, "Vertical-cavity surface-emitting lasers: Design, growth, fabrication, characterization," *IEEE J. Quantum Electron.*, vol. 27, no. 6, pp. 1332–1346, Jun. 1991, doi: 10.1109/3.89950.

[96] S. M. Rytov, "Electromagnetic Properties of a Finely Stratified Medium," *Sov. Phys. JETP*, vol. 2, pp. 466–475, 1956.

[97] R. Kashyap, *Fiber Bragg gratings*, 2nd ed. Burlington, MA: Academic Press, 2010.

[98] "FDTD solutions - Lumerical Inc."

[99] S. Johnson and J. Joannopoulos, "Block-iterative frequency-domain methods for Maxwell's equations in a planewave basis," *Opt. Express*, vol. 8, no. 3, p. 173, Jan. 2001, doi: 10.1364/OE.8.000173.

[100] P. J. Bock *et al.*, "Subwavelength grating periodic structures in silicon-on-insulator: a new type of microphotonic waveguide," *Opt. Express*, vol. 18, no. 19, p. 20251, Sep. 2010, doi: 10.1364/OE.18.020251.

[101] P. J. Bock *et al.*, "Subwavelength grating crossings for silicon wire waveguides," *Opt. Express*, vol. 18, no. 15, p. 16146, Jul. 2010, doi: 10.1364/OE.18.016146.

[102] Z. Wang, X. Xu, D. Fan, Y. Wang, and R. T. Chen, "High quality factor subwavelength grating waveguide micro-ring resonator based on trapezoidal silicon pillars," *Opt. Lett.*, vol. 41, no. 14, p. 3375, Jul. 2016, doi: 10.1364/OL.41.003375.

[103] José Manuel Luque-González, Robert Halir, Juan Gonzalo Wangüemert-Pérez, José de-Oliva-Rubio, Jens H. Schmid, Pavel Cheben, Íñigo Molina-Fernández, and and Alejandro Ortega-Moñux, "An ultracompact GRIN-lens-based spot size converter using subwavelength grating material," *Laser & Photonics Reviews*, vol. 13, 2019.

[104] Alejandro Sánchez-Postigo, Robert Halir, J. Gonzalo Wangüemert-Pérez, Alejandro Ortega-Moñux, Shurui Wang, Martin Vachon, Jens H. Schmid, Dan-Xia Xu, and Pavel Cheben, and Íñigo Molina-Fernández, "Breaking the coupling efficiency-bandwidth trade-off in surface graitng couplers using zero-order radiation," *Laser & Photonics Reviews*, vol. 15, 2021, doi: 10.1002/lpor.202000542.

[105] Robert Halir, Pavel Cheben, Jose Manuel Luque-Gonzalez , Jose Darıo Sarmiento-Merenguel, Jens H. Schmid, Gonzalo Wanguemert-Perez, and Dan-Xia Xu, Shurui Wang, Alejandro Ortega-Monux , and Inigo Molina-Fernandez, "Ultra-broadband nanophotonic beamsplitter using an anisotropic sub-wavelength metamaterial," *Laser & Photonics Reviews*, vol. 10, pp. 1039–1046, 2016.

[106] J. M. Luque-González *et al.*, "Polarization splitting directional coupler using tilted subwavelength gratings," *Opt. Lett.*, vol. 45, no. 13, p. 3398, Jul. 2020, doi: 10.1364/OL.394696.

[107] D. Pérez-Galacho *et al.*, "Optical pump-rejection filter based on silicon sub-wavelength engineered photonic structures," *Opt. Lett.*, vol. 42, no. 8, p. 1468, Apr. 2017, doi: 10.1364/OL.42.001468.

[108] D. Oser *et al.*, "Coherency-Broken Bragg Filters: Overcoming On-Chip Rejection Limitations," *Laser & Photonics Reviews*, vol. 13, no. 8, p. 1800226, Aug. 2019, doi: 10.1002/lpor.201800226.

[109] J. Li *et al.*, "Ultra-broadband large-angle beam splitter based on a homogeneous metasurface at visible wavelengths," *Opt. Express*, vol. 28, no. 21, p. 32226, Oct. 2020, doi: 10.1364/OE.405375.

[110] D. González-Andrade *et al.*, "Ultra-broadband nanophotonic phase shifter based on subwavelength metamaterial waveguides," *Photon. Res.*, vol. 8, no. 3, p. 359, Mar. 2020, doi: 10.1364/PRJ.373223.

[111] H. Xu, D. Dai, and Y. Shi, "Ultra-Broadband and Ultra-Compact On-Chip Silicon Polarization Beam Splitter by Using Hetero-Anisotropic Metamaterials," *Laser & Photonics Reviews*, vol. 13, no. 4, p. 1800349, Apr. 2019, doi: 10.1002/lpor.201800349.

[112] D. Benedikovic *et al.*, "Subwavelength index engineered surface grating coupler with sub-decibel efficiency for 220-nm silicon-on-insulator waveguides," *Opt. Express*, vol. 23, no. 17, p. 22628, Aug. 2015, doi: 10.1364/OE.23.022628.

[113] U. Levy, M. Abashin, K. Ikeda, A. Krishnamoorthy, J. Cunningham, and Y. Fainman, "Inhomogenous Dielectric Metamaterials with Space-Variant Polarizability," *Phys. Rev. Lett.*, vol. 98, no. 24, p. 243901, Jun. 2007, doi: 10.1103/PhysRevLett.98.243901.

[114] P. Cheben *et al.*, "Broadband polarization independent nanophotonic coupler for silicon waveguides with ultra-high efficiency," *Opt. Express*, vol. 23, no. 17, p. 22553, Aug. 2015, doi: 10.1364/OE.23.022553.
[115] C. Alonso-Ramos, P. Cheben, A. Ortega-Moñux, J. H. Schmid, D.-X. Xu, and I. Molina-Fernández, "Fiber-chip grating coupler based on interleaved trenches with directionality exceeding 95%," *Opt. Lett.*, vol. 39, no. 18, p. 5351, Sep. 2014, doi: 10.1364/OL.39.005351.
[116] D. Oser *et al.*, "High-quality photonic entanglement out of a stand-alone silicon chip," *npj Quantum Inf*, vol. 6, no. 1, p. 31, Dec. 2020, doi: 10.1038/s41534-020-0263-7.
[117] E. Luan *et al.*, "Enhanced Sensitivity of Subwavelength Multibox Waveguide Microring Resonator Label-Free Biosensors," *IEEE J. Select. Topics Quantum Electron.*, vol. 25, no. 3, pp. 1–11, May 2019, doi: 10.1109/JSTQE.2018.2821842.
[118] J. Flueckiger *et al.*, "Sub-wavelength grating for enhanced ring resonator biosensor," *Opt. Express*, vol. 24, no. 14, p. 15672, Jul. 2016, doi: 10.1364/OE.24.015672.
[119] J. Gonzalo Wangüemert-Pérez *et al.*, "Evanescent field waveguide sensing with subwavelength grating structures in silicon-on-insulator," *Opt. Lett.*, vol. 39, no. 15, p. 4442, Aug. 2014, doi: 10.1364/OL.39.004442.
[120] R. Kou *et al.*, "Mid-IR broadband supercontinuum generation from a suspended silicon waveguide," *Opt. Lett.*, vol. 43, no. 6, p. 1387, Mar. 2018, doi: 10.1364/OL.43.001387.
[121] E. D. Palik, *Handbook of optical constants of solids*, vol. 3. Academic press, 1998.
[122] "MODE - Finite Difference Eigenmode (FDE) solver - Lumerical Inc."
[123] V. Donzella, A. Sherwali, J. Flueckiger, S. Talebi Fard, S. M. Grist, and L. Chrostowski, "Sub-wavelength grating components for integrated optics applications on SOI chips," *Opt. Express*, vol. 22, no. 17, p. 21037, Aug. 2014, doi: 10.1364/OE.22.021037.
[124] V. Donzella, A. Sherwali, J. Flueckiger, S. M. Grist, S. T. Fard, and L. Chrostowski, "Design and fabrication of SOI micro-ring resonators based on sub-wavelength grating waveguides," *Opt. Express*, vol. 23, no. 4, p. 4791, Feb. 2015, doi: 10.1364/OE.23.004791.
[125] V. Lucarini, J. J. Saarinen, K.-E. Peiponen, and E. M. Vartiainen, *Kramers-Kronig relations in optical materials research*, vol. 110. Springer Science & Business Media, 2005.
[126] Y. Ma, B. Dong, and C. Lee, "Progress of infrared guided-wave nanophotonic sensors and devices," *Nano Convergence*, vol. 7, no. 1, p. 12, Dec. 2020, doi: 10.1186/s40580-020-00222-x.
[127] J. G. Wangüemert-Pérez *et al.*, "[INVITED] Subwavelength structures for silicon photonics biosensing," *Optics & Laser Technology*, vol. 109, pp. 437–448, Jan. 2019, doi: 10.1016/j.optlastec.2018.07.071.
[128] J. M. Chalmers and P. R. Griffiths, *Handbook of vibrational spectroscopy*. Wiley, 2002.
[129] P. Kozma, F. Kehl, E. Ehrentreich-Förster, C. Stamm, and F. F. Bier, "Integrated planar optical waveguide interferometer biosensors: A comparative review,"

*Biosensors and Bioelectronics*, vol. 58, pp. 287–307, Aug. 2014, doi: 10.1016/j.bios.2014.02.049.

[130] D. Rodrigo *et al.*, "Mid-infrared plasmonic biosensing with graphene," *Science*, vol. 349, no. 6244, pp. 165–168, Jul. 2015, doi: 10.1126/science.aab2051.

[131] C. S. Huertas, D. Fariña, and L. M. Lechuga, "Direct and Label-Free Quantification of Micro-RNA-181a at Attomolar Level in Complex Media Using a Nanophotonic Biosensor," *ACS Sens.*, vol. 1, no. 6, pp. 748–756, Jun. 2016, doi: 10.1021/acssensors.6b00162.

[132] J. Xu, D. Suarez, and D. S. Gottfried, "Detection of avian influenza virus using an interferometric biosensor," *Anal Bioanal Chem*, vol. 389, no. 4, pp. 1193–1199, Sep. 2007, doi: 10.1007/s00216-007-1525-3.

[133] K. Uchiyamada, K. Okubo, M. Yokokawa, E. T. Carlen, K. Asakawa, and H. Suzuki, "Micron scale directional coupler as a transducer for biochemical sensing," *Opt. Express*, vol. 23, no. 13, p. 17156, Jun. 2015, doi: 10.1364/OE.23.017156.

[134] X. Wang and C. K. Madsen, "Highly sensitive compact refractive index sensor based on phase-shifted sidewall Bragg gratings in slot waveguide," *Appl. Opt.*, vol. 53, no. 1, p. 96, Jan. 2014, doi: 10.1364/AO.53.000096.

[135] S. M. Grist *et al.*, "Silicon photonic micro-disk resonators for label-free biosensing," *Opt. Express*, vol. 21, no. 7, p. 7994, Apr. 2013, doi: 10.1364/OE.21.007994.

[136] C. E. Soteropulos, H. K. Hunt, and A. M. Armani, "Determination of binding kinetics using whispering gallery mode microcavities," *Appl. Phys. Lett.*, vol. 99, no. 10, p. 103703, Sep. 2011, doi: 10.1063/1.3634023.

[137] C. A. Barrios *et al.*, "Slot-waveguide biochemical sensor," *Opt. Lett.*, vol. 32, no. 21, p. 3080, Nov. 2007, doi: 10.1364/OL.32.003080.

[138] X. Tu *et al.*, "Thermal independent Silicon-Nitride slot waveguide biosensor with high sensitivity," *Opt. Express*, vol. 20, no. 3, p. 2640, Jan. 2012, doi: 10.1364/OE.20.002640.

[139] D.-X. Xu *et al.*, "Real-time cancellation of temperature induced resonance shifts in SOI wire waveguide ring resonator label-free biosensor arrays," *Opt. Express*, vol. 18, no. 22, p. 22867, Oct. 2010, doi: 10.1364/OE.18.022867.

[140] S. M. Grist *et al.*, "Silicon photonic micro-disk resonators for label-free biosensing," *Opt. Express*, vol. 21, no. 7, p. 7994, Apr. 2013, doi: 10.1364/OE.21.007994.

[141] A. Densmore *et al.*, "Sensitive Label-Free Biomolecular Detection Using Thin Silicon Waveguides," *Advances in Optical Technologies*, vol. 2008, pp. 1–9, Jun. 2008, doi: 10.1155/2008/725967.

[142] G. Gaur, S. Hu, R. L. Mernaugh, I. I. Kravchenko, S. T. Retterer, and S. M. Weiss, "Label-free detection of Herceptin® using suspended silicon microring resonators," *Sensors and Actuators B: Chemical*, vol. 275, pp. 394–401, Dec. 2018, doi: 10.1016/j.snb.2018.07.081.

[143] V. R. Almeida, Q. Xu, C. A. Barrios, and M. Lipson, "Guiding and confining light in void nanostructure," *Opt. Lett.*, vol. 29, no. 11, p. 1209, Jun. 2004, doi: 10.1364/OL.29.001209.

[144] C. A. Barrios *et al.*, "Slot-waveguide biochemical sensor," *Opt. Lett.*, vol. 32, no. 21, p. 3080, Nov. 2007, doi: 10.1364/OL.32.003080.
[145] C. F. Carlborg *et al.*, "A packaged optical slot-waveguide ring resonator sensor array for multiplex label-free assays in labs-on-chips," *Lab Chip*, vol. 10, no. 3, pp. 281–290, 2010, doi: 10.1039/B914183A.
[146] A. Di Falco, L. O'Faolain, and T. F. Krauss, "Chemical sensing in slotted photonic crystal heterostructure cavities," *Appl. Phys. Lett.*, vol. 94, no. 6, p. 063503, Feb. 2009, doi: 10.1063/1.3079671.
[147] X. Sun, D. Dai, L. Thylén, and L. Wosinski, "High-sensitivity liquid refractive-index sensor based on a Mach-Zehnder interferometer with a double-slot hybrid plasmonic waveguide," *Opt. Express*, vol. 23, no. 20, p. 25688, Oct. 2015, doi: 10.1364/OE.23.025688.
[148] A. Densmore *et al.*, "Silicon photonic wire biosensor array for multiplexed real-time and label-free molecular detection," *Opt. Lett.*, vol. 34, no. 23, p. 3598, Dec. 2009, doi: 10.1364/OL.34.003598.
[149] A. Densmore *et al.*, "Spiral-path high-sensitivity silicon photonic wire molecular sensor with temperature-independent response," *Opt. Lett.*, vol. 33, no. 6, p. 596, Mar. 2008, doi: 10.1364/OL.33.000596.
[150] J. Hu *et al.*, "Planar waveguide-coupled, high-index-contrast, high-Q resonators in chalcogenide glass for sensing," *Opt. Lett.*, vol. 33, no. 21, p. 2500, Nov. 2008, doi: 10.1364/OL.33.002500.
[151] C. Pérez-Armenta *et al.*, "Narrowband Bragg filters based on subwavelength grating waveguides for silicon photonic sensing," *Opt. Express*, vol. 28, no. 25, p. 37971, Dec. 2020, doi: 10.1364/OE.404364.
[152] "Journal of Biophotonics - 2015 - Melnik - Human IgG detection in serum on polymer based Mach-Zehnder interferometric.pdf."
[153] L. Martinez and M. Lipson, "Suspended Silicon-On-Insulator ring resonators," in *2006 Conference on Lasers and Electro-Optics and 2006 Quantum Electronics and Laser Science Conference*, Long Beach, CA, USA, 2006, pp. 1–2. doi: 10.1109/CLEO.2006.4628162.
[154] Z. Zhou, B. Yin, and J. Michel, "On-chip light sources for silicon photonics," *Light Sci Appl*, vol. 4, no. 11, pp. e358–e358, Nov. 2015, doi: 10.1038/lsa.2015.131.
[155] S. Serna *et al.*, "Engineering third-order optical nonlinearities in hybrid chalcogenide-on-silicon platform," *Opt. Lett.*, vol. 44, no. 20, p. 5009, Oct. 2019, doi: 10.1364/OL.44.005009.
[156] J. D. Sarmiento-Merenguel *et al.*, "Controlling leakage losses in subwavelength grating silicon metamaterial waveguides," *Opt. Lett.*, vol. 41, no. 15, p. 3443, Aug. 2016, doi: 10.1364/OL.41.003443.
[157] V. Donzella, A. Sherwali, J. Flueckiger, S. M. Grist, S. T. Fard, and L. Chrostowski, "Design and fabrication of SOI micro-ring resonators based on sub-wavelength grating waveguides," *Opt. Express*, vol. 23, no. 4, p. 4791, Feb. 2015, doi: 10.1364/OE.23.004791.

[158] J. S. Penadés *et al.*, "Suspended silicon waveguides for long-wave infrared wavelengths," *Opt. Lett.*, vol. 43, no. 4, p. 795, Feb. 2018, doi: 10.1364/OL.43.000795.
[159] S. Jahani *et al.*, "Controlling evanescent waves using silicon photonic all-dielectric metamaterials for dense integration," *Nat Commun*, vol. 9, no. 1, p. 1893, Dec. 2018, doi: 10.1038/s41467-018-04276-8.
[160] M. B. Mia, S. Z. Ahmed, I. Ahmed, Y. J. Lee, M. Qi, and S. Kim, "Exceptional coupling in photonic anisotropic metamaterials for extremely low waveguide crosstalk," *Optica*, vol. 7, no. 8, p. 881, Aug. 2020, doi: 10.1364/OPTICA.394987.
[161] D.-X. Xu *et al.*, "Empirical model for the temperature dependence of silicon refractive index from O to C band based on waveguide measurements," *Opt. Express*, vol. 27, no. 19, p. 27229, Sep. 2019, doi: 10.1364/OE.27.027229.
[162] L. Zhang, J. Chen, C. Ma, W. Li, Z. Qi, and N. Xue, "Research Progress on On-Chip Fourier Transform Spectrometer," *Laser & Photonics Reviews*, vol. 15, no. 9, p. 2100016, Sep. 2021, doi: 10.1002/lpor.202100016.
[163] B. I. Akca and C. R. Doerr, "Interleaved Silicon Nitride AWG Spectrometers," *IEEE Photon. Technol. Lett.*, vol. 31, no. 1, pp. 90–93, Jan. 2019, doi: 10.1109/LPT.2018.2884244.
[164] K. Ma, K. Chen, N. Zhu, L. Liu, and S. He, "High-Resolution Compact On-Chip Spectrometer Based on an Echelle Grating With Densely Packed Waveguide Array," *IEEE Photonics J.*, vol. 11, no. 1, pp. 1–7, Feb. 2019, doi: 10.1109/JPHOT.2018.2888592.
[165] J. Huang, J. Yang, H. Zhang, J. Zhang, W. Wu, and S. Chang, "Analysis of Tunable Flat-Top Bandpass Filters Based on Graphene," *IEEE Photon. Technol. Lett.*, vol. 28, no. 23, pp. 2677–2680, Dec. 2016, doi: 10.1109/LPT.2016.2615064.
[166] A. V. Velasco *et al.*, "High-resolution Fourier-transform spectrometer chip with microphotonic silicon spiral waveguides," *Opt. Lett.*, vol. 38, no. 5, p. 706, Mar. 2013, doi: 10.1364/OL.38.000706.
[167] H. Podmore *et al.*, "Demonstration of a compressive-sensing Fourier-transform on-chip spectrometer," *Opt. Lett.*, vol. 42, no. 7, p. 1440, Apr. 2017, doi: 10.1364/OL.42.001440.
[168] K. Okamoto, H. Aoyagi, and K. Takada, "Fabrication of Fourier-transform, integrated-optic spatial heterodyne spectrometer on silica-based planar waveguide," *Opt. Lett.*, vol. 35, no. 12, p. 2103, Jun. 2010, doi: 10.1364/OL.35.002103.
[169] E. le Coarer *et al.*, "Wavelength-scale stationary-wave integrated Fourier-transform spectrometry," *Nature Photon*, vol. 1, no. 8, pp. 473–478, Aug. 2007, doi: 10.1038/nphoton.2007.138.
[170] X. Nie, E. Ryckeboer, G. Roelkens, and R. Baets, "CMOS-compatible broadband co-propagative stationary Fourier transform spectrometer integrated on a silicon nitride photonics platform," *Opt. Express*, vol. 25, no. 8, p. A409, Apr. 2017, doi: 10.1364/OE.25.00A409.

[171] R. A. Soref, F. De Leonardis, and V. M. N. Passaro, "Scanning Spectrometer-on-a-Chip Using Thermo-Optical Spike-Filters or Vernier-Comb Filters," *J. Lightwave Technol.*, vol. 37, no. 13, pp. 3192–3200, Jul. 2019, doi: 10.1109/JLT.2019.2912725.
[172] B. I. Akca, "Design of a compact and ultrahigh-resolution Fourier-transform spectrometer," *Opt. Express*, vol. 25, no. 2, p. 1487, Jan. 2017, doi: 10.1364/OE.25.001487.
[173] P. R. Griffiths, "The Early Days of Commercial FT-IR Spectrometry: A Personal Perspective," *Appl Spectrosc*, vol. 71, no. 3, pp. 329–340, Mar. 2017, doi: 10.1177/0003702816683529.
[174] M. C. M. M. Souza, A. Grieco, N. C. Frateschi, and Y. Fainman, "Fourier transform spectrometer on silicon with thermo-optic non-linearity and dispersion correction," *Nat Commun*, vol. 9, no. 1, p. 665, Dec. 2018, doi: 10.1038/s41467-018-03004-6.
[175] S. N. Zheng *et al.*, "Microring resonator-assisted Fourier transform spectrometer with enhanced resolution and large bandwidth in single chip solution," *Nat Commun*, vol. 10, no. 1, p. 2349, Dec. 2019, doi: 10.1038/s41467-019-10282-1.
[176] M. Florjanczyk, P. Cheben, S. Janz, A. Scott, B. Solheim, and D.-X. Xu, "Multiaperture planar waveguide spectrometer formed by arrayed Mach-Zehnder interferometers," *Opt. Express*, vol. 15, no. 26, p. 18176, 2007, doi: 10.1364/OE.15.018176.
[177] P. J. Bock *et al.*, "Subwavelength grating Fourier-transform interferometer array in silicon-on-insulator: Fourier-transform interferometer array," *Laser & Photonics Reviews*, vol. 7, no. 6, pp. L67–L70, Nov. 2013, doi: 10.1002/lpor.201300063.
[178] M. Nedeljkovic, A. V. Velasco, A. Z. Khokhar, A. Delage, P. Cheben, and G. Z. Mashanovich, "Mid-Infrared Silicon-on-Insulator Fourier-Transform Spectrometer Chip," *IEEE Photon. Technol. Lett.*, vol. 28, no. 4, pp. 528–531, Feb. 2016, doi: 10.1109/LPT.2015.2496729.
[179] M. Montesinos-Ballester *et al.*, "On-chip Fourier-transform spectrometer based on spatial heterodyning tuned by thermo-optic effect," *Sci Rep*, vol. 9, no. 1, p. 14633, Dec. 2019, doi: 10.1038/s41598-019-50947-x.
[180] D. Pohl *et al.*, "An integrated broadband spectrometer on thin-film lithium niobate," *Nat. Photonics*, vol. 14, no. 1, pp. 24–29, Jan. 2020, doi: 10.1038/s41566-019-0529-9.
[181] P. R. Griffiths and J. A. De Haseth, *Fourier transform infrared spectrometry*. John Wiley & Sons, 2007.
[182] Q. Liu *et al.*, "Integrated broadband dual-polarization Ge-rich SiGe mid-infrared Fourier-transform spectrometer," *Opt. Lett.*, vol. 43, no. 20, p. 5021, Oct. 2018, doi: 10.1364/OL.43.005021.
[183] J. Li, D. Lu, and Z. Qi, "Miniature Fourier transform spectrometer based on wavelength dependence of half-wave voltage of a LiNbO_3 waveguide interferometer," *Opt. Lett.*, vol. 39, no. 13, p. 3923, Jul. 2014, doi: 10.1364/OL.39.003923.
[184] L. Li *et al.*, "Design of an on-chip Fourier transform spectrometer based on waveguide Mach–Zehnder Interferometer and fluidics," *Optics Communications*, vol. 460, p. 125103, Apr. 2020, doi: 10.1016/j.optcom.2019.125103.

[185] D. M. Kita *et al.*, "High-performance and scalable on-chip digital Fourier transform spectroscopy," *Nat Commun*, vol. 9, no. 1, p. 4405, Dec. 2018, doi: 10.1038/s41467-018-06773-2.
[186] Gabriel Lippmann, "La photographie des couleurs," *Bulletin Sté Française de Photographie*, vol. 7 of 2, 1891.
[187] M. Madi, F. Ceyssens, I. Shorubalko, H. P. Herzig, B. Guldimann, and P. Giaccari, "Lippmann waveguide spectrometer with enhanced throughput and bandwidth for space and commercial applications," *Opt. Express*, vol. 26, no. 3, p. 2682, Feb. 2018, doi: 10.1364/OE.26.002682.
[188] H. Wang, Q. Li, and W. Shi, "On-chip polarization-insensitive Fourier transform spectrometer," *Opt. Lett.*, vol. 45, no. 6, p. 1479, Mar. 2020, doi: 10.1364/OL.385205.
[189] Y. Li, M. Vanslembrouck, and R. Baets, "Two-way-fed silicon-on-insulator grating couplers with a broad bandwidth," in *Advanced Photonics 2016 (IPR, NOMA, Sensors, Networks, SPPCom, SOF)*, Vancouver, 2016, p. ITu1B.5. doi: 10.1364/IPRSN.2016.ITu1B.5.
[190] D. M. Sonnenfroh and M. G. Allen, "Observation of CO and CO2 absorption near 1.57 □m with an external-cavity diode laser," p. 3.
[191] D. Taillaert, P. Bienstman, and R. Baets, "Compact efficient broadband grating coupler for silicon-on-insulator waveguides," *Opt. Lett.*, vol. 29, no. 23, p. 2749, Dec. 2004, doi: 10.1364/OL.29.002749.
[192] M. Florjańczyk *et al.*, "Development of a Fourier-transform waveguide spectrometer for space applications," *Opt Quant Electron*, vol. 44, no. 12–13, pp. 549–556, Oct. 2012, doi: 10.1007/s11082-012-9596-6.
[193] P. Cheben *et al.*, "A high-resolution silicon-on-insulator arrayed waveguide grating microspectrometer with sub-micrometer aperture waveguides," *Opt. Express*, vol. 15, no. 5, p. 2299, 2007, doi: 10.1364/OE.15.002299.
[194] S. Janz *et al.*, "Planar Waveguide Echelle Gratings in Silica-On-Silicon," *IEEE Photon. Technol. Lett.*, vol. 16, no. 2, pp. 503–505, Feb. 2004, doi: 10.1109/LPT.2003.823139.
[195] E. Heidari, X. Xu, C.-J. Chung, and R. T. Chen, "On-chip Fourier transform spectrometer on silicon-on-sapphire," *Opt. Lett.*, vol. 44, no. 11, p. 2883, Jun. 2019, doi: 10.1364/OL.44.002883.
[196] C. Alonso-Ramos *et al.*, "Diffraction-less propagation beyond the sub-wavelength regime: a new type of nanophotonic waveguide," *Sci Rep*, vol. 9, no. 1, p. 5347, Dec. 2019, doi: 10.1038/s41598-019-41810-0.
[197] Govind P. Agrawal, *Nonlinear Fiber Optics*, 6th ed. 2019.
[198] J. M. Dudley and G. Genty, "Supercontinuum light," *Physics Today*, vol. 66, no. 7, pp. 29–34, Jul. 2013, doi: 10.1063/PT.3.2045.
[199] N. Singh *et al.*, "Octave-spanning coherent supercontinuum generation in silicon on insulator from 1.06 μm to beyond 2.4 μm," *Light Sci Appl*, vol. 7, no. 1, pp. 17131–17131, Jan. 2018, doi: 10.1038/lsa.2017.131.

[200] C. Lafforgue *et al.*, "Broadband supercontinuum generation in nitrogen-rich silicon nitride waveguides using a 300 mm industrial platform," *Photon. Res.*, vol. 8, no. 3, p. 352, Mar. 2020, doi: 10.1364/PRJ.379555.
[201] D. Grassani *et al.*, "Mid infrared gas spectroscopy using efficient fiber laser driven photonic chip-based supercontinuum," *Nat Commun*, vol. 10, no. 1, p. 1553, Dec. 2019, doi: 10.1038/s41467-019-09590-3.
[202] Y. Yu *et al.*, "A broadband, quasi-continuous, mid-infrared supercontinuum generated in a chalcogenide glass waveguide: Broadband supercontinuum generation in the MIR," *Laser & Photonics Reviews*, vol. 8, no. 5, pp. 792–798, Sep. 2014, doi: 10.1002/lpor.201400034.
[203] C. Ciret and S.-P. Gorza, "Generation of ultra-broadband coherent supercontinua in tapered and dispersion-managed silicon nanophotonic waveguides," *J. Opt. Soc. Am. B*, vol. 34, no. 6, p. 1156, Jun. 2017, doi: 10.1364/JOSAB.34.001156.
[204] N. Singh *et al.*, "Supercontinuum generation in varying dispersion and birefringent silicon waveguide," *Opt. Express*, vol. 27, no. 22, p. 31698, Oct. 2019, doi: 10.1364/OE.27.031698.
[205] M. Sinobad *et al.*, "Mid-infrared octave spanning supercontinuum generation to 85 μm in silicon-germanium waveguides," *Optica*, vol. 5, no. 4, p. 360, Apr. 2018, doi: 10.1364/OPTICA.5.000360.
[206] J. Leuthold, C. Koos, and W. Freude, "Nonlinear silicon photonics," *Nature Photon*, vol. 4, no. 8, pp. 535–544, Aug. 2010, doi: 10.1038/nphoton.2010.185.
[207] J. M. Dudley, G. Genty, and S. Coen, "Supercontinuum generation in photonic crystal fiber," *Rev. Mod. Phys.*, vol. 78, no. 4, pp. 1135–1184, Oct. 2006, doi: 10.1103/RevModPhys.78.1135.
[208] U. D. Dave *et al.*, "Dispersive-wave-based octave-spanning supercontinuum generation in InGaP membrane waveguides on a silicon substrate," *Opt. Lett.*, vol. 40, no. 15, p. 3584, Aug. 2015, doi: 10.1364/OL.40.003584.
[209] B. Kuyken, X. Liu, R. M. Osgood Jr., R. Baets, G. Roelkens, and W. M. J. Green, "Mid-infrared to telecom-band supercontinuum generation in highly nonlinear silicon-on-insulator wire waveguides," *Opt. Express*, vol. 19, no. 21, p. 20172, Oct. 2011, doi: 10.1364/OE.19.020172.
[210] R. Halir, Y. Okawachi, J. S. Levy, M. A. Foster, M. Lipson, and A. L. Gaeta, "Ultrabroadband supercontinuum generation in a CMOS-compatible platform," *Opt. Lett.*, vol. 37, no. 10, p. 1685, May 2012, doi: 10.1364/OL.37.001685.
[211] H. Zhao *et al.*, "Visible-to-near-infrared octave spanning supercontinuum generation in a silicon nitride waveguide," *Opt. Lett.*, vol. 40, no. 10, p. 2177, May 2015, doi: 10.1364/OL.40.002177.
[212] M. A. G. Porcel *et al.*, "Two-octave spanning supercontinuum generation in stoichiometric silicon nitride waveguides pumped at telecom wavelengths," *Opt. Express*, vol. 25, no. 2, p. 1542, Jan. 2017, doi: 10.1364/OE.25.001542.

[213] D. D. Hickstein *et al.*, "Quasi-Phase-Matched Supercontinuum Generation in Photonic Waveguides," *Phys. Rev. Lett.*, vol. 120, no. 5, p. 053903, Feb. 2018, doi: 10.1103/PhysRevLett.120.053903.

[214] N. Singh, M. Raval, E. Ippen, Michael. R. Watts, and F. X. Kärtner, "Supercontinuum generation in silicon Bragg grating waveguide," *Appl. Phys. Lett.*, vol. 118, no. 7, p. 071106, Feb. 2021, doi: 10.1063/5.0040722.

[215] J. Zhang, C. Alonso-Ramos, L. Vivien, S. He, and E. Cassan, "Self-Adaptive Waveguide Boundary for Inter-Mode Four-Wave Mixing," *IEEE J. Select. Topics Quantum Electron.*, vol. 26, no. 2, pp. 1–8, Mar. 2020, doi: 10.1109/JSTQE.2019.2929700.

[216] J. Wei, C. Ciret, M. Billet, F. Leo, B. Kuyken, and S.-P. Gorza, "Supercontinuum Generation Assisted by Wave Trapping in Dispersion-Managed Integrated Silicon Waveguides," *Phys. Rev. Applied*, vol. 14, no. 5, p. 054045, Nov. 2020, doi: 10.1103/PhysRevApplied.14.054045.

[217] J. Hult, "A Fourth-Order Runge–Kutta in the Interaction Picture Method for Simulating Supercontinuum Generation in Optical Fibers," *J. Lightwave Technol.*, vol. 25, no. 12, pp. 3770–3775, Dec. 2007, doi: 10.1109/JLT.2007.909373.

[218] X. Gai *et al.*, "Nonlinear absorption and refraction in crystalline silicon in the mid-infrared," *Laser & Photonics Reviews*, vol. 7, no. 6, pp. 1054–1064, 2013.